DOCTOR OF SCIENCES

Electrodynamical approach of surface multifunctionality the tuning of the Lifshitz-van der Waals interactions

Dellieu, Louis

Award date:
2016

Awarding institution:
University of Namur

University of Namur
Faculty of Sciences

Electrodynamical approach of surface multifunctionality: the tuning of the Lifshitz-van der Waals interactions

Thesis Submitted in Fulfillment of the Requirements of the Degree of Doctor of Philosophy in Physics

Louis Dellieu

Academic year 2016 - 2017

A mes parents

Electrodynamical approach of surface multifunctionality: the tuning of the Lifshitz-van der Waals interactions

by Louis Dellieu

Abstract: For a long time, anti-reflective properties have a major importance in the development of optical devices. For instance, anti-reflective coatings are required when designing telescopes, camera lenses, solar cells or glass windows. In another context, superhydrophobicity, i.e the ability of a surface to exhibit a static water contact angle equal or greater than 150â, is a key property for numerous industrial applications. Indeed, superhydrophobic surfaces can exhibit self-cleaning properties. As a matter of fact, a surface or coating that could combine both anti-reflective and superhydrophobic properties is highly interesting. However, this achievement of such multifunctional surfaces is far from being easily reachable, not only from experimental aspects but also from fundamental physics.

In literature, from a theoretical point of view, superhydrophobicity and antireflection are almost always studied separately. In this thesis work, we propose an elegant and unified theory for jointly dealing with these two problems. The way to tackle this issue relies on Lifshitz-van der Waals interaction theory. These appear as a major contribution to the interaction potential energy in many interfacial phenomena within macroscopic systems. Taking origin from quantum vacuum fluctuations, the Lifshitz-van der Waals interactions are shown to be tunable via properly designed antireflective nanostructured surfaces. The impact of this tuning in terms of surface multifunctionality is discussed and the concept is applied to two general practical cases: the superhydrophobic surface and the switching from attractive to repulsive Lifshitz-van der Waals forces.

Ph. D. thesis in Physics

Jury :
Prof. Philippe Lambin (President, University of Namur)
Prof. Serge Reynaud (Laboratoire Kastler Brossel)
Prof. Joël De Coninck (University of Mons)
Dr. Michaël Sarrazin (Co-advisor, University of Namur)
Prof. Olivier Deparis (Advisor, University of Namur)

Remerciements

Voici venu pour moi le moment tant redouté des remerciements. En effet, si cette page est pour vous la première à être lue, sachez qu'elle n'en est pas moins la dernière à être écrite. Certains parleront de garder le meilleur pour la fin, pour ma part il s'agit d'aborder le plus délicat. Délicat car la gratitude ne peut se réduire à un simple "merci" sommairement écrit à la fin d'une lettre. Elle requiert au contraire de prendre du temps, de trouver les mots justes pour exprimer mon sentiment, de m'assurer qu'aucun de mes proches et collaborateurs n'ait été oublié. En effet, comme disait Paul-Jean Toulet dans son roman "Monsieur du Paur, homme public": *Il y a des gens qui ont la susceptibilité de l'huître, on ne peut y toucher sans qu'ils se contractent.* Sur ces quelques précautions oratoires, permettez-moi, chers lecteurs, de me prêter maintenant à l'exercice délicat du remerciement.

Je tiens tout d'abord à remercier mon promoteur, le Prof. Olivier Deparis, mon co-promoteur, le Dr. Michaël Sarrazin, ainsi que le Prof. Jean Pol Vigneron pour le temps qu'ils m'ont consacré durant ces années de recherche, pour leur patience, leurs conseils et leur infinie gentillesse. Ils sont pour beaucoup dans mon épanouissement scientifique et je leur en serai éternellement reconnaissant.

Je souhaite également remercier les membres de mon jury de thèse (externes à mes encadrants), le Prof. Philippe Lambin, le Prof. Serge Reynaud, le Prof. Joël De Coninck pour la lecture attentive de ce manuscrit et les précieux conseils qu'ils m'ont prodigués afin d'en améliorer le contenu.

Je remercie bien évidemment le Fonds de la Recherche Scientifique pour m'avoir permis, par l'octroi d'une bourse, de réaliser cette thèse de doctorat.

Je remercie ensuite l'ensemble de mes collègues pour l'ambiance de travail sans égale rencontrée au sein de nos laboratoires: Céline, Amaury (MBA), Adrien, Paul Louis, Romain, Damien C, Alexandre, Jean-François, Mathieu, Bruno, Nicolas, Aline, Isabelle, Eloïse, Michaël, Sébastien, Steve-O, Nicolas .G et tous ceux que j'aurais oublié de citer[1]. Notre dynamisme de groupe aura été un pur plaisir du début à la fin, il perdurera à travers nos amitiés consolidées au fil de ces années. De manière plus personnelle, je tiens également à féliciter le Dr. Jean-François Colomer pour ses progrès en course à pied, j'ai pu les constater lors de nos "petites sorties" du midi. Qui sait Jean-Jean, peut- être passeras-tu un jour devant moi....

Je remercie également les différentes personnes qui ont contribué à la réalisation de mon travail: le Dr. Jérôme Muller, le Dr. Branko Kolaric, le Dr. Guillaume Fleury, le Dr. Alexandre

[1] Limite d'espace oblige.

Felten, le Prof. Christian Seassal, et de manière générale toute autre personne ayant participé de près ou de loin à l'élaboration de ma thèse.

Enfin, je remercie du fond du coeur ma famille ainsi que ma compagne Marine pour leur précieux soutien et leur présence affecteuse à mes côtés.

Contents

I Introduction and state of the art **11**

Introduction **13**

1 State of the art **17**

1.1 Surface functionality 17

1.1.1 Water-repellent surfaces 17

1.1.2 Antireflective surfaces 21

1.1.3 Modeling the wettability 21

1.1.4 Modeling the antireflectivity 23

1.2 Casimir effect 23

1.2.1 Planar geometry 24

1.2.2 Non-planar geometry 25

1.2.3 Modeling Casimir effect 27

II Theoretical framework **29**

2 Basic concepts **31**

2.1 The surface tension 31

2.2 Interfacial interactions in macroscopic systems 32

2.2.1 The Lifshitz-van der Waals interactions 33

2.2.2 The acid-base interactions 34

2.2.3 Electrostatic double layer interactions 35

2.3 Classical models of wettability 36

2.3.1 The Young-Dupré equation 37

2.3.2 The Wenzel model 37

2.3.3 The Cassie-Baxter model 38

2.4 Effective medium approximation 38

2.5 Anti-reflective surfaces 39

2.5.1 Thin film 39

2.5.2 Micro/nanostructures 40

2.6 Scattering matrix 42

2.6.1 Zeros of the scattering matrix . . . 42
2.6.2 Poles of the scattering matrix . . . 42
2.6.3 Remark . . . 43

3 The rigorous coupled-wave analysis 45
3.1 Structure description within the Fourier representation . . . 45
3.2 Elementary patterns description within a bidimensional periodic system . . . 47
3.2.1 Circular region . . . 47
3.2.2 Rectangular region . . . 47
3.2.3 Ring region . . . 47
3.3 Maxwell's equations within Fourier representation . . . 48
3.4 The polarization basis . . . 50
3.5 The transfer matrix T . . . 52
3.6 The scattering matrix S . . . 53
3.7 Scattering matrices assembly . . . 54
3.8 Poynting vectors, R, T, A coefficients . . . 56

4 The quantum vacuum fluctuations 57
4.1 The free fields . . . 57
4.2 The classical Hamiltonian . . . 58
4.3 The quantum Hamiltonian . . . 59
4.4 Properties of the $\widehat{a}_{\overrightarrow{k},\sigma}(t)$ and $\widehat{a}^{\dagger}_{\overrightarrow{k},\sigma}(t)$ operators . . . 60
4.5 The quantum vacuum fluctuations . . . 61

5 The Lifshitz-van der Waals interactions 63
5.1 The individual mode free energy within a cavity system . . . 63
5.2 The free energy of a cavity system and the dispersive energy . . . 65
5.3 The dispersive energy and the density of states . . . 65
5.4 The free energy of a cavity system within the imaginary frequency domain . . . 68
5.5 The Lifshitz-van der Waals interactions . . . 70
5.6 The Lifshitz-van der Waals interactions within the flat bodies geometry . . . 72
5.7 The Lifshitz-van der Waals interactions: the particular case of perfect reflecting mirrors . . . 73
5.8 Illustration of the method . . . 74

III Classical approach of surface multifunctionality at the mesoscopic scale 77

6 The wing of the grey cicada : a natural case of multifunctional surface 79
6.1 Morphology and structural model of the wing membrane . . . 79
6.2 Optical properties. . . . 80

6.2.1 Experimental results . . . 80
6.2.2 Theoretical analysis . . . 83
6.3 Wetting properties . . . 86
6.3.1 Experimental results . . . 86
6.3.2 Theoretical analysis . . . 88
6.4 Summary . . . 90

IV Nanophotonical approach of surface multifunctionality at the nanoscale 93

7 The tuning of Lifshitz-van der Waals interactions 95
7.1 Description of the interacting macroscopic bodies systems . . . 95
7.1.1 The first system : corrugated polyethylene-vacuum-water . . . 95
7.1.2 The second system : corrugated polyethylene-water-flat polyethylene . . . 97
7.1.3 The effective medium . . . 98
7.2 Accuracy of the effective medium approach . . . 99
7.2.1 The far field . . . 99
7.2.2 The near field . . . 100
7.2.3 Preliminary conclusion . . . 104
7.3 Numerical results for the corrugated polyethylene-vacuum-water system . . . 105
7.4 Discussion . . . 107
7.4.1 The quality factor . . . 107
7.5 The three dimensional treatment . . . 109

8 Lifshitz-van der Waals interactions and superhydrophobicity 113
8.1 Calculation of the water contact angle . . . 113
8.2 Achievement of the superhydrophobicity . . . 114
8.3 The case of cylinders . . . 116
8.4 The equilibrium separation distance . . . 118
8.5 Possible experimental validations . . . 120

9 The repulsive Lifshitz-van der Waals interactions 123
9.1 Traditional approach of repulsive Lifshitz-van der Waals interactions . . . 123
9.2 Negative Hamaker constant . . . 124
9.3 Modeling and simulation details . . . 125
9.4 Numerical results . . . 125
9.5 The electrostatic double layer . . . 127

10 Toward experimental validation 129
10.1 Block copolymer spin-casting . . . 129
10.2 Sequential infiltration synthesis . . . 130

10.3 Oxygen plasma chemical etching 131
10.4 Plasma etching 132
10.5 Octadecyltrichlorosilane passivating 133

V Conclusions and perspectives **135**

Conclusion **137**

A Integration of the Lifshitz-van der Waals energy over the Brillouin zone **139**

B Convergence study of the Lifshitz-van der Waals potential energy **141**
B.1 Cones 141
B.2 Cylinders 141

C Electrostatic potential energy between a cones array and a semi-infinite plane **145**

Bibliography **146**

Part I

Introduction and state of the art

Introduction

For a long time, anti-reflective properties have a major importance in the development of optical devices. For instance, anti-reflective coatings are required when designing telescopes, camera lenses, solar cells or glass windows. Such coatings allow, *e.g.,* avoiding undesirable reflections in optical imaging or increasing light trapping in solar cells. Moreover, since anti-reflective coatings are wavelength-dependent devices, they can be used to reject efficiently unwanted radiation, for instance, to enhance ultraviolet light protection in sunglasses. In another context, superhydrophobicity, *i.e* the ability of a surface to exhibit a static water contact angle equal or greater than 150°, is a key property for numerous industrial applications. Indeed, superhydrophobic surfaces can exhibit self-cleaning properties: since water droplets cannot stick on such a surface, the rolling drops clear the surface from any impurities. As a matter of fact, an optical device that could combine both anti-reflective and superhydrophobic properties is highly interesting. Such surfaces are known as multifunctional surfaces.

Superhydrophobicity can be achieved purely by geometrical surface designs (nano or micrometer structures), without the need of any additional chemical surface functionalization. Specific surface structures, like nanometric size cones, can be designed to provide superhydrophobicity but may also convey antireflection property. Therefore, cones patterned surfaces appear as good candidates for designing multifunctional surfaces.

In literature, superhydrophobicity and antireflection are almost always studied separately. Indeed, antireflection is commonly described by classical optics while superhydrophobicty is described, in the simplest way, by Cassie's law in a thermodynamical approach and, in a more precise way, by finite element methods relying on Navier-Stokes equation or molecular dynamics simulations. However, an elegant and unified way to deal with these two problems jointly is lacking. A way to fill this gap would be to rely on Lifshitz-van der Waals interaction theory. Surprisingly, the fact that the existence of antireflective nanostructures on a surface should affect the Lifshitz-van der Waals force in a two-bodies system configuration and, in particular, the wetting properties of that surface, has never been considered so far. In its basic form, van der Waals theory describes the force between two atoms (or molecules) that arises from the exchange of virtual photons between these atoms. This kind of interaction was extended by Casimir to two perfectly reflecting mirrors interacting in vacuum. In his seminal work, Lifshitz has reformulated the concept of van der Waals and Casimir forces between two macroscopic bodies in terms of vacuum fluctuations of the electromagnetic field. In this thesis work, the tight link between antireflection and superhydrophobicity properties is established from first

principles, in the vacuum photon-mode theoretical framework. The theoretical results presented in this thesis shed a new light on an old yet interesting problem by revisiting the Lifshitz-van der Waals interaction between nanostructured surfaces, especially in the context of wetting mechanisms. Indeed, static and dynamic wetting of solid surfaces by water appear both as an intricate problem, usually due to the complexity of the chemistry and physics of water. Our new approach aims at providing a better understanding of wetting phenomena at the nanoscale level. In their simplest form, these are here studied from the point of view of static contact angle, which is the premise of more complex aspects of wetting. This new approach could pave the way for the design of novel superhydrophobic coatings and trigger further studies in phase with the current scientific hot topics, such as metamaterials.

This thesis work is organized as follows. It begins by a brief state of the art on surface functionality and the Casimir effect. Both theoretical and experimental progresses are reviewed in terms of water-repellent and antireflective coatings regarding surface functionalities, and in terms of interactions within planar and non planar geometries for the Casimir effect. Following that, the manuscript is split into four main parts.

The first part concerns the theoretical framework of this thesis work. It starts with a chapter devoted to the basic concepts required for the easier reading of this manuscript. Concepts regarding surface physics are especially developed (surface tension, interfacial interactions within macroscopic systems, classical models of wettability) as well as concepts related to physical optics (effective medium approximation, antireflective surfaces and scattering matrix formalism). A second chapter presents a summary of the Rigorous Coupled Wave Analysis (RCWA) method. RCWA is a computational method in electromagnetics which is commonly used to determine the optical properties of periodic dielectric structures. It will be here especially employed for calculating the Lifshitz-van der Waals interactions within macroscopic patterned systems. In order to set the general framework of Lifshitz-van der Waals interactions, a chapter introducing the concept of quantum vacuum fluctuations of the electromagnetic field is included. The main steps of the quantization of the free electromagnetic field are firstly exposed, leading naturally to the existence of the zero point energy and the associated vacuum fluctuations. Finally, based on these three first chapters, the theory of Lifshitz-van der Waals interactions is presented within the so-called scattering approach.

The second part of this work is dedicated to the classical approach of surface multifunctionality where wettability and optical properties are investigated separately. As a case study, the wing of the grey cicada, a natural case of multifunctional surface, is investigated. The ultrastructure of the wing is observed to identify the features responsible of the superhydrophobicity and the antireflectivity of the wing. The wetting and optical properties are studied experimentally (reflectance measurements, static contact angle measurements) and theoretically (Cassie-Baxter and Wenzel models, transfer matrix modelling).

The third part of this thesis work presents our new nanophotonics approach of surface multifunctionality. This approach aims at tuning Lifshitz-van der Waals interactions *via* nanostructures and to investigate the impact in terms of surface wettability and surface adhesion. For this purpose, the first chapter of this third part introduces the key concept of manipulating quantum

vacuum photon modes using carefully designed nanostructures in order to tune Lifshitz-van der Waals interactions. Following this major chapter, a second one highlights the influence of such energy modifications on surface wettability. As a case study, static contact angles of a water droplet above a polyethylene nanostructured surface are calculated as a function of the corrugations height. Alternatively to wettability, a third chapter is devoted to the achievement of repulsive Lifshitz-van der Waals interactions within macroscopic corrugated systems. As a case study, the potential interaction energy between a nanopatterned polyethylene slab and a flat polyethylene slab with water as the intervening medium, *i.e.* the medium between both slabs, is calculated. Finally, a fourth last chapter briefly presents the experimental strategy we have selected for fabricating the patterned surfaces considered in this work. Since the fabrication is currently in progress at the time of writing thesis manuscript, only preliminary results are presented.

The fourth and last part of this manuscript is a summary of the main finding of the thesis. Furthermore, perspectives are also discussed.

Chapter 1

State of the art

This chapter aims at providing a brief state of the art on surface functionality and Casimir interactions. Surface functionality is reviewed in terms of water-repellent and/or antireflective surfaces while Casimir interactions are reviewed in terms of interactions within planar and non planar geometries. Since those both concepts are widely described in the following of this thesis, this chapter only highlights their main aspects.

1.1 Surface functionality

1.1.1 Water-repellent surfaces

In 1805, the pioneering work of Thomas Young started describing the behavior of a liquid droplet on flat surfaces [1]. Understood in terms of thermodynamic properties of surfaces, Young's theory on wetability allowed to trigger discussions on "the frictional resistance to a displacement of the contact line" [2] and on the contact angle hysteresis effect, still under investigations nowadays [3][4]. Further developments led to the understanding of the wetting of rough or heterogeneous surfaces through the Wenzel [5] and Cassie-Baxter equations [6]. Together, these theories established the required surface characteristics for achieving highly water-repellent materials[1]. Moreover, deeper understanding of water-repellent surfaces led naturally to more refined models using numerical approaches such as finite element methods relying on the Navier-Stokes equations [7] or molecular dynamic simulations [8].

Up to now, three main strategies exist for reaching highly water-repellent surfaces, known as (super)hydrophobic surfaces : the use of low-surface-energy materials, the use of surface micro-or-nanostructures and the use of "slippery infused porous surfaces" (SLIPS) effect. It is noteworthy that such strategies usually lead to additional surface functions such as anti-icing properties [9] or antibacterial properties [10][11]

[1] Both theories are described in Chapter 2.

Low-surface-energy materials

Low-surface-energy materials are especially bound among polymers such as polytetrafluoroethylene (PTFE, commonly known as Teflon), polyethylene (PE) or polystyrene (PS) [12][13][14]. Such a low surface energy behavior arises from the predominant apolar character of the poly-

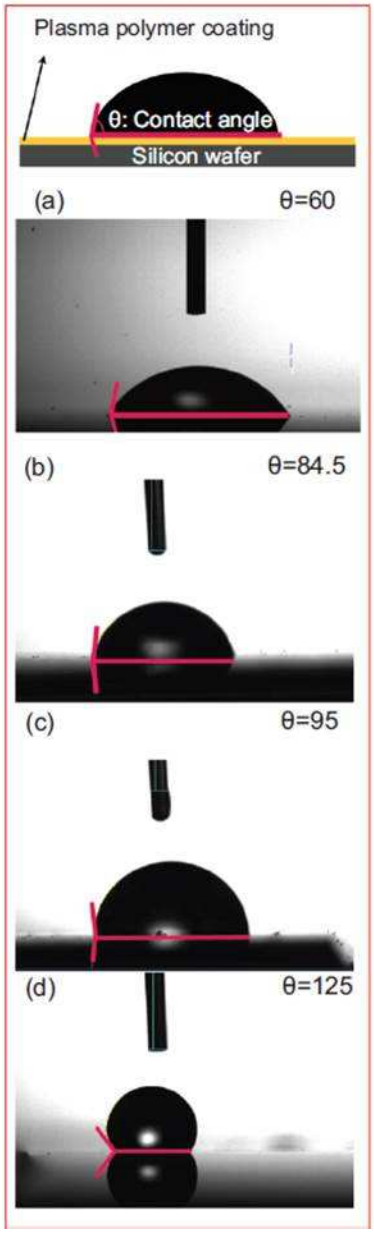

Figure 1.1: Sessile water droplet contact angle measurements on the (a) uncoated silicon waffer, (b) isopropyl alcohol coated, (c) toluene coated and (d) perfluorordecalin coated silicon wafer [15].

meric materials [16]. Moreover, specific polymers can be applied as coatings on various materials in order to modify surface wettability and, usually, to achieve hydrophobicity [17]. As an example, Fig. 1.1 displays the effect of a plasma polymer coating using various monomers on silicon wafer [15]. As expected, the as-synthetized polymeric coating, according to the chemical nature

of the monomer, enhances the water contact angle.

Other alternative methods can be employed to create low-energy surfaces by simply using other apolar materials than polymers [18] or self-assembly of molecular monolayers such as silane monolayers [19]. The latter method leads to a more precise control of the surface chemistry and the water-repellency of several materials [20].

Surface micro-nanopatterning

Alternatively to these surface and/or polymer chemistry approaches for reaching hydrophobicity, methods using surface patterning started to be developed in the late 1990s in order to achieve

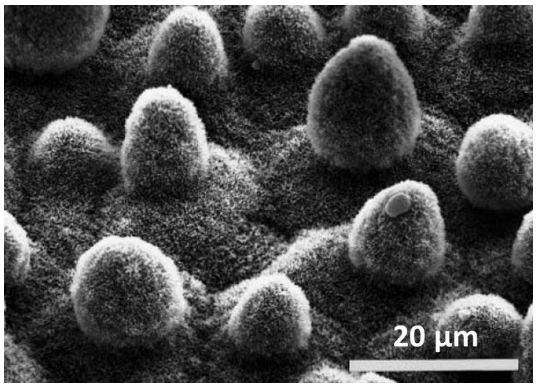

Figure 1.2: Structure of lotus leaf [21].

superhydrophobicity, which was not reachable with the previously developed low-surface-energy materials strategy. Inspired by the structure of the lotus leaf (Fig. 1.2) [21], the fabrication of superhydrophobic surfaces combining micro-nanostructures[2] and specific surface chemistry started to emerge [22][23][24]. Superhydrophobic surfaces are known to exhibit a static water contact angle equal or higher than 150° and a low contact angle hysteresis (less or equal to 5°).

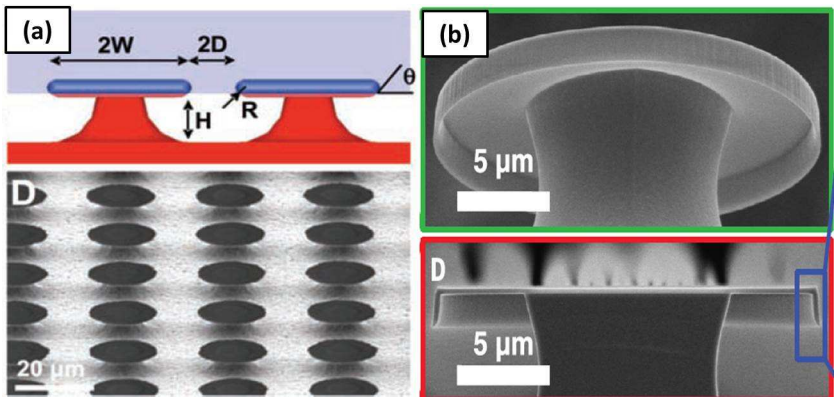

Figure 1.3: (a) Re-entrant curvature structure [25]. (b) Double re-entrant curvature structure [26].

These new breakthroughs led to a wide development of superhydrophobic surface based on

[2]Surfaces exhibiting both micro-and nano-features are known as fractal surfaces.

surfaces patterning, exploring new materials and processes as well as seeking for fundamental understanding [27][28][29]. As an outstanding example, the re-entrant (Fig. 1.3a) [25] or double re-entrant (Fig. 1.3b) [26] curvature surfaces developed in the late 2000s and 2010s provide with a strong resistance against low-surface-energy liquids[3] that would completely wet typical nanostructured superhydrophobic surfaces.

Other remarkable superhydrophobic surfaces can be found in nature such cicada's wings [30] (see Chapter 6), exhibiting lotus-like nanostructures, or springtail shells [31] (Fig. 1.4), exhibiting double re-entrant-like nanostructures.

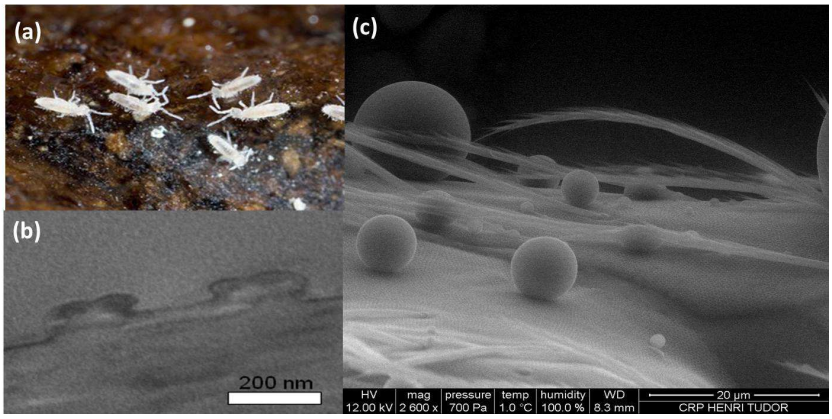

Figure 1.4: (a) Springtail. (b) Springtail shell's nanostructure. (c) Environmental scanning electron microscopy imaging of nanodroplets on springtail shell's nanostructures. This images were obtained during this thesis work.

Slippery liquid-infused porous surfaces

Although the structured surfaces introduced above enhanced liquid repellency, they still struggle with practical drawbacks: limited oleophobicity with high contact angle hysteresis [32], failure under pressure and upon physical damage [33], inability to self-heal and high production cost[28][33]. In order to address this problem, scientists from Harvard University, inspired by

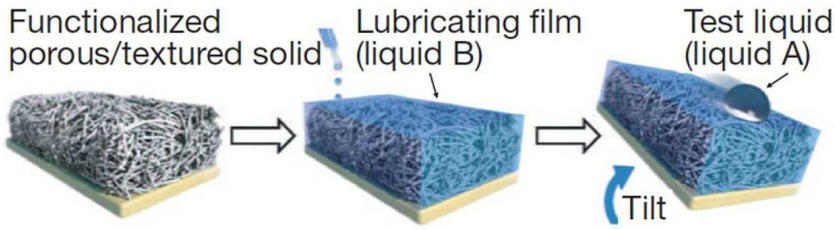

Figure 1.5: Sketch showing the fabrication of a SLIPS [34].

the Nepenthes pitcher plants [35], created a new class of functional materials: slippery liquid-infused porous surfaces (SLIPS), in which a functionalized porous/textured solid is infiltrated with a low-surface-energy, chemically inert liquid. The latter forms a physically smooth and

[3]Such surfaces are qualified as superoleophobic surfaces.

chemically homogeneous lubricating film on the surface substrate (Fig. 1.5) [34]. The resulting surfaces exhibit high pressure stability, low contact angle hysteresis, no contact line pinning, self healing properties, low production cost and omniphobicity, *i.e.* the surface is *both* superhydrophobic and oleophobic. From this approach, a wide variety of fabrication techniques emerged for producing SLIPS, exploring different types of materials and potential applications [36][37][38].

1.1.2 Antireflective surfaces

Antireflective surfaces are well known for several decades [39]. Used in a wide variety of applications (corrective lenses, decorative glasses, solar cells etc.), antireflective coatings are commonly achieved *via* three main strategies : the use of thin film interference, the use of graded index profile and the use of microstructures. These strategies are very briefly described hereafter and in more details in Chapter 2 where examples are also provided.

Quarter-wavelength thin film is the simplest form of antireflective coating. Discovered by Lord Rayleigh in 1886 [40], it consists of a single layer deposited on a surface and aims at greatly reducing the reflection by making use of appropriate phase changes and the dependence of the reflectivity on the index of refraction. Antireflective thin films are used for moderate suppression of reflectance over a broad spectral range, *e.g.* 450-1100 nm at normal incidence [39]. However, the performances of single layer thin films are not exceptional and usually required the use of multiple layer thin films for achieving efficient antireflective coatings [41]. An alternative way for reducing reflectance is to gradually decrease the refractive index of the film from the substrate to the external medium, *i.e.* air. Graded-index profiles are naturally found in moth eyes or cicada wings as a nanocones patterning [42][30] but can be artificially obtained with a multilayer structure [43]. Such antireflective graded index profile structures are used, for instance, in solar cells for enhancing their efficiency [44][45]. Surface microtexturing is also known to render a substrate anti-reflective, as demonstrated by many scientists since 1960s [46] and the reason for the antireflectivity is the light trapping through multiple internal reflections [39]. These microstructures usually consist of pyramidal, honeycomb or other kind of patternings. For long time, they were used in solar cells for enhancing the efficiency but they have been more recently employed to improve light-extraction efficiency of existing light-emitting diodes [47].

1.1.3 Modeling the wettability

Several methods for modeling the behavior of a liquid droplet on a flat or rough surface exist. Analytical methods, such Young's approach, Wenzel's approach or Cassie-Baxter approach, can provide a first approximation for evaluating the static contact angle on flat surfaces (Young's equation) or rough/heterogeneous surfaces (Wenzel/Cassie-Baxter approach). However, for an accurate description, more refined modeling approaches are needed, requiring the use of computational methods such as molecular dynamics or finite element methods.

Molecular dynamics (MD) simulations involve the physical motions of atoms and molecules, calculated by numerically solving the corresponding Newtons equations of motion [48]. Interac-

tion forces are derived from the potential energy of the atoms within molecules arising from both intramolecular and intermolecular forces. The intramolecular interactions are calculated based on the geometry of the molecule, while the intermolecular interactions are governed by van der Waals and electrostatic forces. By solving these equations at each time step, trajectories for a set of molecules can be calculated. MD simulations turns out to be a very powerful numerical

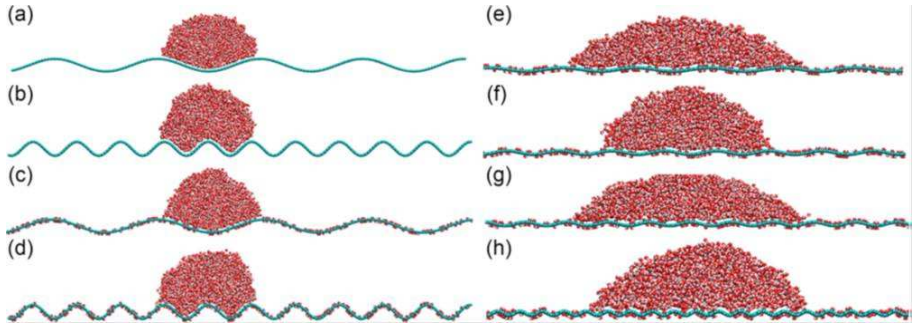

Figure 1.6: Molecular dynamics simulation of a water droplet on wrinkled graphene and graphene oxide [49].

tool for studying a variety of physical and mechanical properties, since this method provides a way to quantify the influence of atomic-scale interactions on macroscopic phenomena. For instance, MD allows calculating the surface tensions of liquid and solid surfaces as well as the static contact angle of liquid nanodroplets on flat or rough surfaces (Fig. 1.6) [50]. However, MD suffers from severe drawbacks in the case of wetting modeling, such as huge computation time.

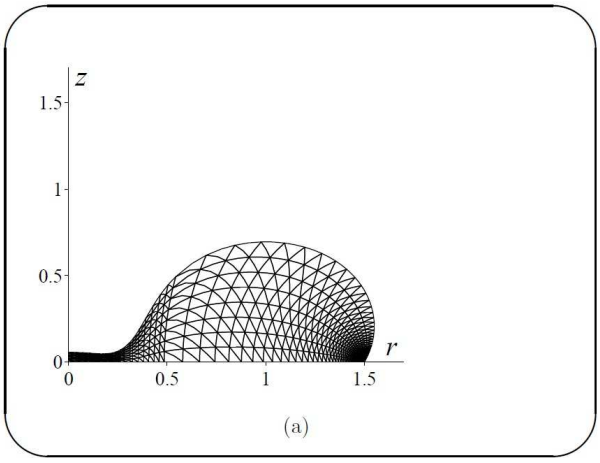

Figure 1.7: Snapshot of a relatively coarse computational mesh used for calculating the impact of a droplet on a hydrophobic substrate [51].

An alternative approach to molecular dynamics is the finite element method (FEM) [7]. FEM is a numerical technique for finding approximate solutions to boundary value problems described by partial differential equations. A whole domain is divided into a collection of subdomains (Fig. 1.7), each represented by a set of elementary equations of the original problem. Equations are then solved in each subdomains, according to the boundary conditions. In this way, the

solution can be propagated from one subdomain to another. In the specific case of wetting, Navier-Stokes equations are solved in each subdomains. FEM allows studying, for instance, the water droplet pinning over the edge of surface corrugation [52] or the evolution of the droplet over an hydrophobic surface (Fig. 1.7) [53]. FEM is widely used, especially due to its high flexibility of implementation. However, as for MD, FEM is a very time consuming method since it does not allow numerical parallelization.

1.1.4 Modeling the antireflectivity

While dealing with optical properties, a wide range of numerical methods are available [54]. Many of them rely on the numerical solving of classical Maxwell's equations in their differential form *via* differential methods. In the specific case of nanostructured objects and surfaces, three main methods are employed : the finite difference time domain (FDTD) method [55], the Green tensor method [54] and the rigorous coupled wave analysis (RCWA) method [56]. The first and second method are usually used for isolated object, although they can be extended to periodically structured surfaces. FDTD method consists in discretizing Maxwell's equations in time and space using finite differences while the Green tensor method uses integral methods for recasting Maxwell's equations into an integral form. The RCWA describes the diffraction of electromagnetic waves by periodic grating structures in which the spatially periodic permittivity and electromagnetic field are expanded in Fourier series. This method is known to provide excellent results in calculating the far field reflection and transmission [56][54]. The RCWA method is described in details in Chapter 3.

1.2 Casimir effect

The understanding of the nature of the forces between atoms, molecules and macroscopic bodies has a long history. The synopsis of that story starts in 1873 with a Dutch physicist named Johannes Diderik van der Waals. In order to account for properties of non ideal gases and liquids, van der Waals proposed a general theory of the attraction between neutral atoms, the so-called van der Waals forces [57]. At that time, these forces were introduced in a completely *ad hoc* manner, by placing well chosen parameters in the equation of state. However, the complete understanding of van der Waals forces required the advent of quantum mechanics in the early 1900s and, in particular, the work of London on dispersive force in 1930 [58].

A few years after the Second Wolrd War, another young Dutch physicist named Hendrik Casimir was working on colloidal solutions at Philips Research Laboratories . One of his colleague, Theodor Overbeek, realized that the theory used for describing the van der Waals interactions between these colloids did not match with the experimental observations. Overbeek asked Casimir to study this problem in order to coin the underlying physical effects of those non intuitive observations. With the help of Dirk Polder, Casimir had the intuition that the van der Waals interaction between the colloids had to be interpreted in terms of vacuum fluctuations. From this brilliant idea, he decided to shift his mind from colloids to perfect re-

flecting mirrors. In 1948, Casimir published his famous article *On the attraction between two perfectly conducting plates* in the Proceedings of the Royal Netherlands Academy of Arts and Science [59].

Although emerging from the same phenomenon, van der Waals and Casimir interactions were initially thought of as two different kinds of forces rather than two limiting cases of a single physical phenomenon (*i.e.* the vacuum fluctuations), as they are nowadays understood. On one hand, the Casimir forces were used to describe the dispersive interactions between perfect reflecting mirrors at large atomic separation distances and, on the other hand, van der Waals forces were employed to describe the interactions between atoms and molecules at atomic scale separations distances. In 1956, a unified theory of both van der Waals and Casimir forces between planar parallel plates in thermal equilibrium was developed by Evgeny Lifshitz [60]. His theory described dispersion forces between dissipative media as a physical phenomenon caused by the vacuum fluctuations. In the limiting cases of small and large separation distances, the Lifshitz's theory was able to reproduce both van der Waals and Casimir results. This unified force has since been well studied from both experimental and theoretical perspectives [61].

1.2.1 Planar geometry

In the 60 years following Casimir's prediction, scientists did not really step aside from the original parallel-planar geometry. Many authors extended Casimir's theory to arbitrary dielectric materials [62][63], non ideal mirrors [64][65] or arbitrary multilayer geometries [66]. Particular combinations of materials with specific conditions on their anisotropic character, permittivity and permeability properties were also investigated in order to obtain repulsive Casimir force [67][62][68].

Many measurements of van der Waals and Casimir forces were made before the 1990s, of which only experiment by van Blockland and Overbeek in 1978 with metallic surfaces can be considered as an unambiguous demonstration [69]. However, due to its weakness, precise experimental investigation of the Casimir effect required several decades of technological advances before obtaining sufficiently high precision instruments to measure it accurately [61][70]. In this modern stage of Casimir experiments, one the first experimental observations has its beginning in the experiment made by Lamoreaux in 1997 [71]. Lamoreaux used a torsion balance to measure the Casimir force between a gold-coated lens and a metallic plate at separations about 1 μm. However, uncertainties related to the experiment did not permit to consider it an actual proof of Casimir force. It took until 2002 to see the emergence of the first valid experiment of the Casimir force between two planar plates [72]. In this experiment, the two parallel surfaces are the opposing faces of a cantilever beam, free to oscillate around its clamping point, and of another thicker beam rigidly connected to a frame with adjustable distance from the cantilever. Fig. 1.8 displays the experimental setup used for this experiment. From now on, measurements of Casimir's force within the planar geometry started to be investigated for several configurations and experimental conditions [61].

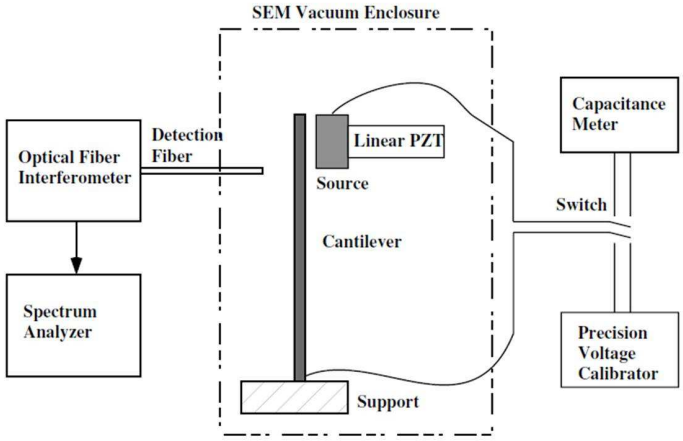

Figure 1.8: The experimental setup developed for the first valid and precise experimental proof of the Casimir force between two planar plates [72].

1.2.2 Non-planar geometry

The problem of the non planar geometry has long attracted the attention of scientists [73][74][75] but the investigations were really triggered by the first and accurate direct measurements of the

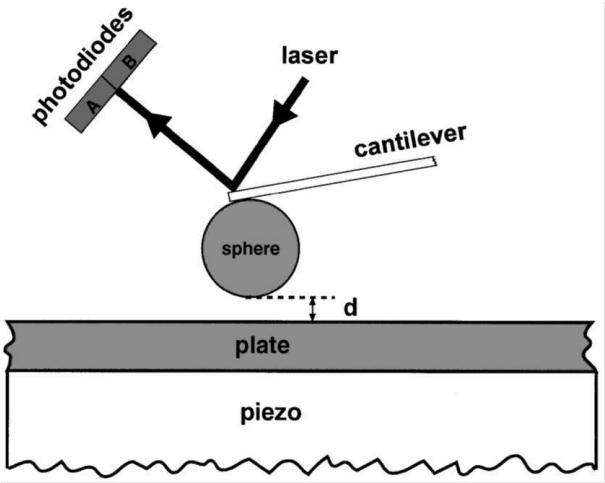

Figure 1.9: Schematic diagram of the experimental setup used to measure Casimir force [76].

Casimir force between a metal-coated sphere and a plate using standard AFM (Fig. 1.9) [76]. This experimental work led to a renewed interest in the geometrical dependence of the Casimir effect. Following the seminal paper of Derjaguin on the treatment of Casimir's interaction within the sphere-plane geometry [77], many authors started studying this configuration using different theoretical and experimental approaches [78][79][80]. Especially, this sphere-plane geometry allowed investigating, from both experimental and theoretical aspects, specific topics such the thermal Casimir effect [81][82], the repulsive Casimir force using fluids or gazes as intervening medium [83][84][85] or the Casimir effect applied to micromechanical torsonial-oscillator device [86]. The sphere-plane system was extended by authors to alternative geometries involving compact bodies interacting with planar or compact objects such as cones [88], wedges

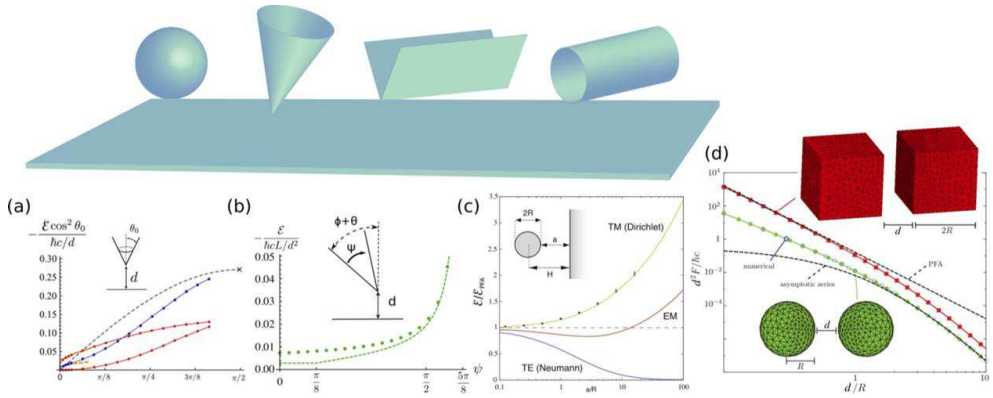

Figure 1.10: Selected results of Casimir interactions involving compact bodies suspended above planar objects or interacting with other compact bodies [87]

[88], cylinders [89] (Fig. 1.10) or more complicated shapes such as waveguides, disks, cubes, tetrahedral particles, and capsules [87][90].

Alternatively to isolated objects, the growing interest in nanoelectromechanical systems urges the scientific community to study in depth Casimir interactions within nanostructured systems, such as periodic rectangular gratings or periodically cones-patterned surfaces [91]. In particular, looking at nanostructures in the theoretical framework of dispersive interactions turns out to be of great interest, both from fundamental and experimental perspectives [92][93][94][95]. As an illustration, Fig. 1.11 displays the experimental set up and associated SEM images used to highlight strong reduction of Casimir force through metallic surface nanostructuring [96]. Moreover, the developments of brand new metamaterials naturally led scientist

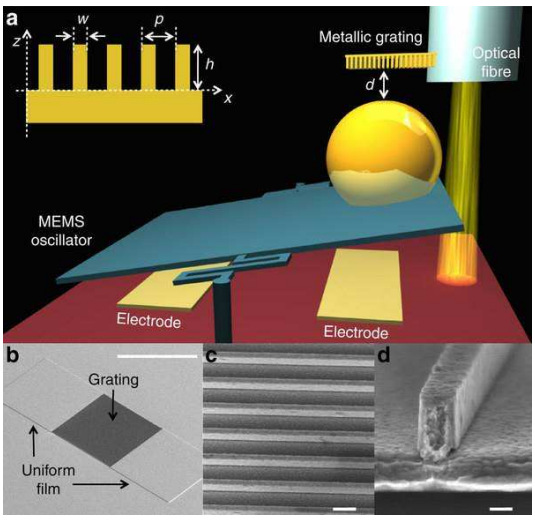

Figure 1.11: The experimental set up and associated SEM images used to highlight strong reduction of Casimir force through metallic surface nanostructuring [96]

to study the Casimir effect within such a context for achieving, for instance, repulsive Casimir force [97] or electric levitation [98]. All these new insights led to the development of more precise and refined theoretical tools, briefly discussed hereafter, each one addressing specific size and

shape of the interacting objects.

1.2.3 Modeling Casimir effect

In order to understand the behaviour of Casimir interactions between non planar macroscopic bodies, many approaches have emerged, each one addressing specific corrugation geometries. On one hand, approximation methods, such as the proximity force approximation (PFA) and the pairwise summation (PWS), appear to be the most employed when describing interactions between smooth corrugated surfaces at short and long separation distances, respectively. On the other hand, when considering corrugated surfaces with small correlation lengths (of the order of the separation distance), methods such as scattering or perturbative approaches are required in order to take into account diffraction and correlation effects which occur at the nanoscale.

The PWS is a simple semiclassical approach which allows calculating the Casimir force between two bodies as a sum of the forces acting between their constituents (atoms or molecules) [70]. This kind of method has been widely used in the theory of dispersion forces and allows a simple calculation for many configurations of experimental interest.

The PFA is another approximate method for the calculation of the Casimir force between bodies of arbitrary shape. This method was suggested in 1934 by Derjaguin [77] and applied to the interpretation of measurements of the Casimir force in the sphere - plate geometry mentioned above [76]. It consists in approximating the surface roughness profile of an object by a set of parallel plates (Fig. 1.12). Therefore, the force per unit area of an equivalent parallel-plate geometry is summed for all adjacent surfaces. A full discussion about the advantages and disadvantages of the PWS and PFA methods is provided elsewhere [70].

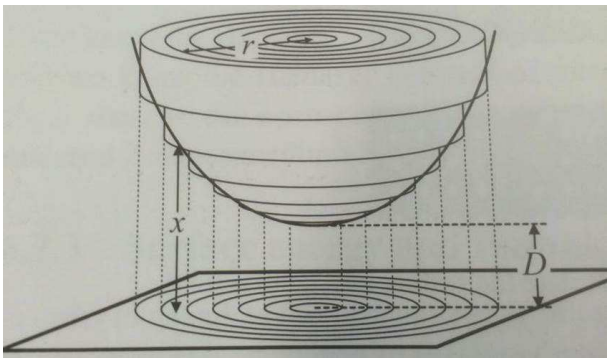

Figure 1.12: Schematic of Derjaguin approximation [99]. An half-sphere is approximated by a stack of planar cylinders of various diameters.

While considering corrugated surfaces with small correlation lengths (of the order of the separation distance), methods such as the scattering approach are required [100]. Indeed, for small correlation length surfaces, the reflection of electromagnetic waves from short-scale structures leads to diffraction and correlation effects which cannot be described properly by the summation of interatomic potentials (PWS) or by the replacement of the roughness profile by a set of parallel plates (PFA). The scattering approach allows to bypass this problem. The method is based on the calculation of the individual scattering matrices of each interacting elements,

as well as the intervening medium, solely represented by their respective dielectric properties. While calculating scattering matrices, *via* the RCWA method for instance, diffraction and correlation effects are fully taken into account, avoiding any inaccuracies in the calculation of the Casimir force.

Over the last years, a number of even more refined numerical methods have been developed and have demonstrated their accuracy in predicting Casimir interactions for arbitrary geometries and materials [101][102]. As an illustration, an efficient technique for computing Casimir energies and forces has been recently developed to deal with objects of arbitrarily complex three dimensional geometries [90]. By approximating compact objects by a set of discretized planar triangles (Fig. 1.13), the authors managed to obtain the first predictions of Casimir interactions in a number of experimentally relevant geometries, including crossed cylinders and tetrahedral nanoparticles [90].

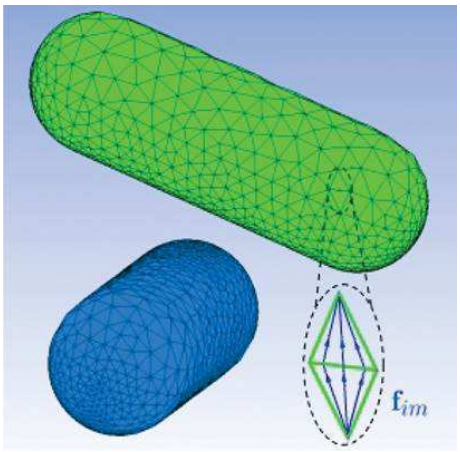

Figure 1.13: Surfaces of compact conducting objects are discretized into planar triangles [90].

The development of these advanced numerical techniques, jointly with experimental capabilities at submicrometer scales, naturally led to a huge number of experiments in order to probe the geometrical and material dependence of the Casimir effect [102]. These insights could pave the way for new perspective in the development of nanoelectronical systems (NEMS) through, for instance, Casimir torque [68][103][104][105]. Such phenomena could be exploited for adding new functionality to the architecture of NEMS [102].

Part II

Theoretical framework

Chapter 2

Basic concepts

This chapter aims at providing the basic concepts required for the easier reading of this manuscript. Concepts regarding surface physics are especially developed as well as concepts related to physical optics. From the definition of the surface tension, the concepts of cohesion/adhesion energies are introduced leading to the description of the classical models of wettability as well as interfacial interactions in macroscopic systems. Especially, the Lifshitz-van der Waals interactions which are the main point of this thesis are described. Then, from a physical optics point of view, a general description of the effective medium approach for treating the dielectric properties of composite materials is provided. Such an approach allows introducing the antireflective surfaces and their corresponding approximations in terms of continuous materials with a graded refractive index profile. Finally, the major concept of the scattering matrix which allows probing the optical properties of a system is described. The reader should note that the two main concepts, *i.e.* the Lifshitz-van der Waals interactions and the scattering matrix, are only briefly described here. A much more detailed description is provided in Chapter 3 for the scattering matrix and in Chapters 4 and 5 for the Lifshitz-van der Waals interactions.

2.1 The surface tension

The surface tension γ_i (or the surface free energy per unit area) of a one body system i is defined as the half of the cohesion energy U_{ii} of the one body system in vacuum such as [18] :

$$\gamma_i = \frac{1}{2} \left| U_{ii} \right| . \tag{2.1}$$

The cohesion energy corresponds to the work required to separate the body i into two bodies i (Fig. 2.1a) [18]. It receives contributions from several independent interaction energies which allows to rewrite the cohesion energy as :

$$U_{ii} = \sum_j U_{ii}^j, \tag{2.2}$$

where j stands for one the j^{th} type of interaction described hereafter. Similarly, the surface tension of a one body system receives contributions from the same independent interaction energies such as :

$$\gamma_i = \sum_j \gamma_i^j. \tag{2.3}$$

In the same way, the surface tension γ_{12} of a two body system $1-2$ is defined from the adhesion

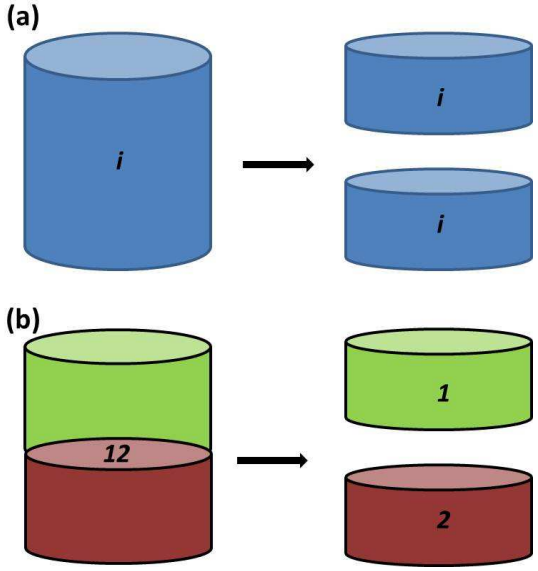

Figure 2.1: (a) Sketch of cohesion process. (b)Sketch of adhesion process.

energy U_{12} of the two body system in vacuum [18] :

$$\gamma_{12} = \gamma_1 + \gamma_2 - U_{12} \tag{2.4}$$

The adhesion energy corresponds to the work required to separate the two body system $1-2$ into two individual bodies 1 and 2 (Fig. 2.1b) [18]. As for the cohesion energy, the adhesion energy has contributions from several independent interactions energies and writes as :

$$U_{12} = \sum_j U_{12}^j. \tag{2.5}$$

Similarly, the surface tension of a two body system rewrites as :

$$\gamma_{12} = \sum_j \gamma_{12}^j. \tag{2.6}$$

2.2 Interfacial interactions in macroscopic systems

Interfacial interactions are generally described as interaction energies between macroscopic bodies [106], such as a droplet of water and a corrugated surface. These interactions include, among others, the Lifshitz-van der Waals interactions and the acid-base interactions, the descriptions

of which are summarized hereafter.

2.2.1 The Lifshitz-van der Waals interactions

The Lifshitz's theory of van der Waals energy is a method proposed by Evgeny Mikhailovich Lifshitz in 1954 for treating van der Waals interactions between macroscopic bodies [60]. The original method relies on the quantum field theory and is, in essence, a generalization of the Casimir effect [59] which allows calculating the radiation pressure within a two flat bodies system made of any materials. Since the original Lifshitz's work is arduous to coin, only the key concepts for understanding the main ideas of the Lifshitz's theory are presented hereafter.

The van der Waals interactions and the Lifshitz's approach

In 1873, Johannes Diderik van der Waals proposed the concept of a general attractive interaction between neutral atoms in order to explain several unusual properties of nonideal gases and liquids [57]. Such kind of interactions were shown to be related to the virtual photons[1] exchange between : (1) two randomly oriented dipoles (Keesom interaction [107]), (2) a randomly oriented dipole and an induced dipole (Debye interaction [108]), (3) two induced dipoles (London interaction [58]).

In 1937, the first theory of van der Waals interactions between macroscopic bodies was developed by H. C. Hamaker and applied to a two-spheres system and a sphere-wall system [109]. The method assumed that the total force between two macroscopic bodies, each consisting of many molecules in the van der Waals theory, was simply the sum of the intermolecular van der Waals forces, where the pairwise additivity was employed. However, such pairwise additivity method ignores the influence of neighboring molecules on the interaction between any pair of molecules. Indeed, the presence of a third molecule should change the van der Waals interactions between two molecules. This problem of additivity was completely avoided by the Lifshitz's approach [60]. In his theory, Lifshitz considered the bodies and the corresponding intervening medium between them as continuous media described in terms of bulk properties, *i.e.* permittivity ε_i (Fig. 2.2). Since bulk properties already contained all the necessary informations on the molecular structures of each bodies, Lifshitz was able to calculate the van der Waals interactions which were expressed in terms of radiation pressure. In his simplest version, the so-called Lifshitz-van der Waals interactions energy, known as apolar energy, per unit area U^{LW} writes as :

$$U^{LW}(L) = -\frac{A_h}{12\pi L^2}, \tag{2.7}$$

where A_h, the Hamaker constant, writes as :

$$\begin{aligned} A_h &= \frac{3}{4}k_BT\left(\frac{\varepsilon_1^0-\varepsilon_3^0}{\varepsilon_1^0+\varepsilon_3^0}\right)\left(\frac{\varepsilon_2^0-\varepsilon_3^0}{\varepsilon_2^0+\varepsilon_3^0}\right) \\ &\quad +\frac{3h}{4\pi}\int_{\xi_1}^{\infty}\left(\frac{\varepsilon_1(i\xi)-\varepsilon_3(i\xi)}{\varepsilon_1(i\xi)+\varepsilon_3(i\xi)}\right)\left(\frac{\varepsilon_2(i\xi)-\varepsilon_3(i\xi)}{\varepsilon_2(i\xi)+\varepsilon_3(i\xi)}\right)d\xi. \end{aligned} \tag{2.8}$$

[1] See Chapter 4.

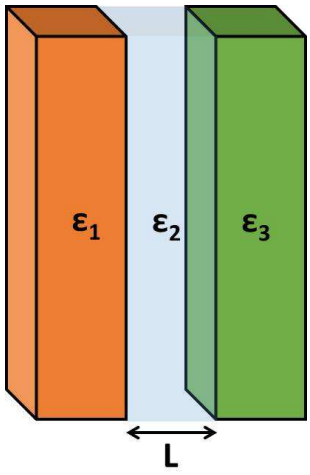

Figure 2.2: Sketch of a cavity formed by two bodies. The bodies and the intervening medium are represented by their permittivity.

with $\xi_1 = \frac{2\pi k_B T}{h}$. The first term containing the static permittivities of the three media $\varepsilon_1^0, \varepsilon_2^0$ and ε_3^0, represents the Keesom energy plus the Debye energy. The second term, usually dominant at room temperature, is assimilated to the London energy and is independent from the temperature. It involves a dependence on the imaginary frequency ($i\xi$) of the dielectric functions. As an example, the Hamaker constant for the interaction between amorphous silicon oxide and silicon oxide, with air as intervening medium (at $20°C$) can be calculated from (2.8). From the spectral data available for the permittivities [18], the Hamaker constant of this system is:

$$A_h = 1.03 \times 10^{-21} J + 6.42 \times 10^{-20} J = 6.52 \times 10^{-20} J.$$

As expected, at room temperature, the second term relative to the London energy is dominant by one order of magnitude compared to the first term relative to the Keesom energy plus the Debye energy.

The contribution of the Lifshitz-van der Waals interactions to the surface tension γ_i^{LW}, known as the apolar component of the surface tension, of a body i writes as :

$$\gamma_i^{LW} = \frac{1}{2} \left| U_{ii}^{LW}(L_0) \right|, \tag{2.9}$$

where $U_{ii}^{LW}(L_0)$ is the Lifshitz-van der Waals energy contributing to the cohesion energy of the body i calculated at the so-called equilibrium separation distance ${L_0}^2$. A much more detailed description of the Lifshitz-van der Waals interactions is provided in Chapter 5.

2.2.2 The acid-base interactions

In addition to the apolar Lifshitz-van der Waals energy, polar interactions involving *e.g.* hydrogen bonds type occur in many nonmetallic materials [18]. By extension, the hydrogen-bonding

[2]The equilibrium separation distance value is usually tabulated and varies around 1.45 Å, depending on the material type.

type interaction has to be understood as comprising all kinds of electron donor-electron acceptor interactions, or more commonly Lewis acid-base interactions. Such interactions are alluded as polar interactions, which must not be mingled with electrostatic interactions described in next section. As the apolar Lifshitz-van der Waals energy, the acid-base energy contribution to the surface tension γ_i^{AB}, known as the polar part of the surface tension, of a body i writes as :

$$\gamma_i^{AB} = \frac{1}{2}\left|U_{ii}^{AB}(L_0)\right|, \tag{2.10}$$

where U_{ii}^{AB} is the acid-base energy contributing to the cohesion energy of the body i. Such interaction decays with distance L from the body as [110] :

$$U_{ii}^{AB}(L) = U_{ii}^{AB}(L_0)e^{\frac{L_0-L}{\lambda}}, \tag{2.11}$$

where λ is the decay length.

The polar component γ_i^{AB} includes a contribution relative to the electron acceptors, γ_i^+, and a contribution relative to the electron donors, γ_i^-, such as :

$$\gamma_i^{AB} = 2\sqrt{\gamma_i^+\gamma_i^-}. \tag{2.12}$$

An interesting property can be introduced in the case of acid-base interactions within a two-body system $1-2$. In this specific case, the polar component of the surface tension γ_{12}^{AB} writes as [18] :

$$\gamma_{12}^{AB} = 2\left(\sqrt{\gamma_1^+\gamma_1^-} + \sqrt{\gamma_2^+\gamma_2^-} - \sqrt{\gamma_1^+\gamma_2^-} - \sqrt{\gamma_2^+\gamma_1^-}\right). \tag{2.13}$$

2.2.3 Electrostatic double layer interactions

The electrostatic doubler layer interaction is the result of the interaction between two charged bodies in a liquid [110]. Such an interaction arises from the overlapping of the electrostatic double layers of the bodies and is repulsive. These concepts are presented hereafter.

The electrostatic double layer

Let us consider a body immersed in water (Fig. 2.3). Because of its high dielectric constant, water is a good solvent for ions leading to different charging process of the surface, ion adsorption or dissociation for instance [110]. Surface charges cause an electric field which attracts counter ions. Such counter ions bind directly to the surface forming the so-called Stern layer (Fig. 2.3). Moreover, while taking into account thermal motion of ions, thermal fluctuations tend to drive the counterions away from the surface leading to the formation of a diffuse layer: the Gouy layer (Fig. 2.3). The layers of the surface charge, the Stern layer and the Gouy layer form together the electrostatic double layer (Fig. 2.3). An electrostatic potential ψ can be associated to the charged planar surface such as :

$$\psi = \psi_0 e^{-\kappa x}, \tag{2.14}$$

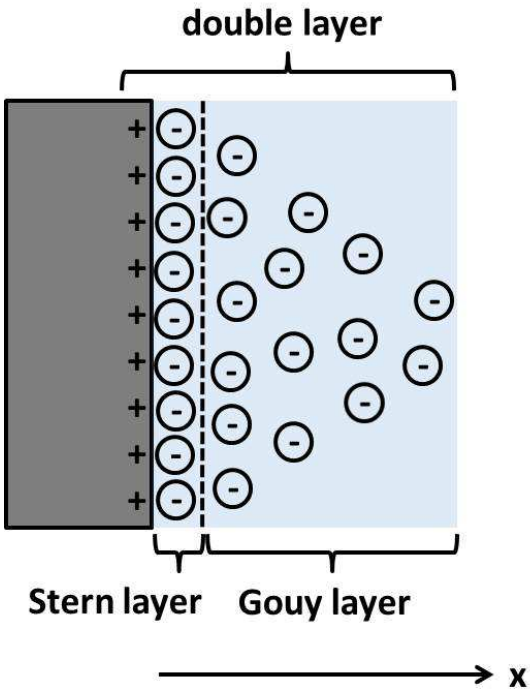

Figure 2.3: Representation of the electrostatic double layer of a charged surface in water.

where κ is the inverse of the Debye screening length λ_D of the liquid and ψ_0 the electrostatic potential at surface $x = 0$.

The electrostatic double layer energy

Considering two charged flat surfaces facing each other in a liquid and separated by a distance L . When those two charged surfaces are brought closer to each other, their electrostatic double layers overlap which induces a modification in their surface charge densities and therefore their electrostatic potentials at the surface. It can be shown that such a modification increases the Gibbs free energy of the system which leads both surfaces to repel each other [110]. The electrostatic potential energy U^{EDL} associated to this electrostatic double layers overlapping is given by [110]:

$$U^{EDL}(L) = \varepsilon_r \varepsilon_0 \kappa \left[2\psi_1(0)\psi_2(0)e^{-\kappa L} - \left(\psi_1^2(0) + \psi_2^2(0)\right) e^{-2\kappa L} \right] \tag{2.15}$$

where ε_r is the static permittivity (dielectric constant) of the liquid, ε_0 is the vacuum permittivity and $\psi_i(0)$ is the surface potential of the ithsurface at the surface.

2.3 Classical models of wettability

Theoretical models of wettability can be employed for predicting the static contact angle of a liquid on a homogeneous or heterogeneous flat surface and on a homogeneous rough surface. The three main analytical models usually employed are : the Young-Dupré model [1, 18], the

Wenzel's model [5] and the Cassie-Baxter model [6]. In the following, the roughness and the heterogeneity will be considered at a scale ranging from 1 nm to 0.5 μm.

2.3.1 The Young-Dupré equation

The Young-Dupré equation allows a theoretical calculation of the static contact angle θ of a droplet of liquid L on a flat homogeneous surface S (Fig. 2.4) at multiscale level[3] [1, 18]. Such a

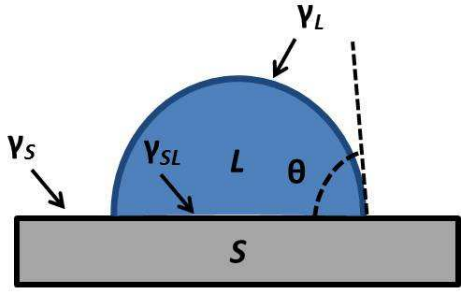

Figure 2.4: Liquid drop with disk contact area on a planar surface.

theoretical description arises from the consideration of a thermodynamical equilibrium between a three phases system: the liquid phase (L), the solid phase (S), and the gas or vapor phase (considered to be vacuum in the present case). Considering the surface tension of the solid γ_S, the surface tension of the liquid γ_L and the surface tension of the solid-liquid system γ_{SL}, the static contact angle writes as :

$$\cos\theta = \frac{\gamma_S - \gamma_{SL}}{\gamma_L}, \tag{2.16}$$

which can be reexpressed in terms of adhesion energy U_{12} :

$$\cos\theta = -1 + \frac{U_{12}}{\gamma_L}. \tag{2.17}$$

As an example, the static contact angle of water on a flat polyethylene surface can be evaluated from the values of the corresponding surface tensions [18]. The surface tension of water is $\gamma_L = 72.5mN/m$, the surface tension of polyethylene is $\gamma_S = 33mN/m$ and the surface tension of the water-polyethylene interface is $\gamma_{SL} = 54.1mN/m$. Therefore, from (2.16), the static water contact angle on a flat polyethylene surface is $\theta = 104°$, which is the measured value [18]. The same calculation is performed in Chapter 8, using (2.17).

2.3.2 The Wenzel model

The effect of the roughness of a homogeneous surface on its wettability can be taken into account by the so-called Wenzel's equation [5] :

$$\cos\theta_{app} = r\cos\theta. \tag{2.18}$$

[3]The equation allows a theoretical description of surface wettability properties at the macroscopic scale as well as the nanoscopic scale.

Here, θ_{app} is the apparent contact angle of a droplet on the corrugated surface which can be observed by eye (Fig. 2.5), θ is the static contact angle that would result from the same droplet on a flat surface of same chemical nature and r the roughness factor. According to the roughness

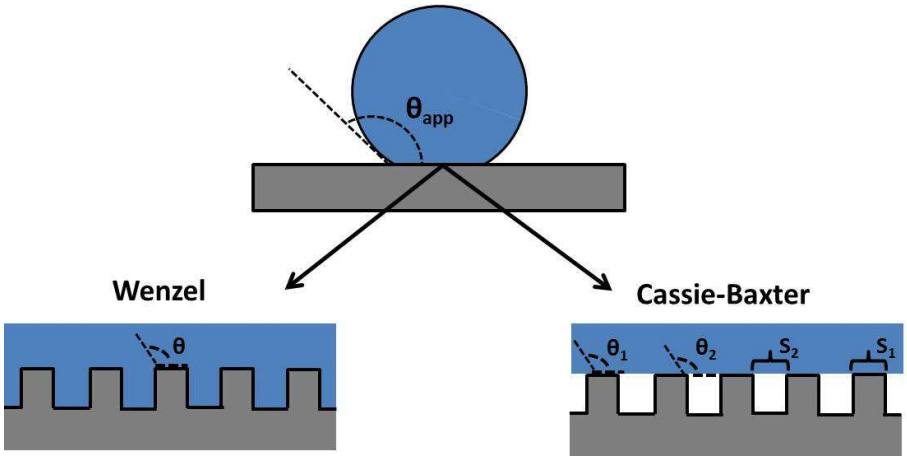

Figure 2.5: Representation of the apparent contact angle θ_{app} and the effect of the roughness from the points of view of the Wenzel model and the Cassie Baxter model.

profile of the surface (Fig. 2.5), the roughness factor r is defined as the ratio between the actual and projected surface areas[4]. This factor is always larger or equal to one. Therefore, surface roughness decreases the contact angle of a hydrophilic flat surface ($\theta < 90°$) and increases the contact angle of a hydrophobic flat surface ($\theta > 90°$).

2.3.3 The Cassie-Baxter model

Most solid surfaces are chemically inhomogeneous. The Cassie-Baxter model [6] considers a smooth but chemically patchwise heterogeneous surface. Considering two different kinds of region 1 and 2 with intrinsic contact angles θ_1 and θ_2, which occupy the surface ratios $f_1 = \frac{S_1}{S_1+S_2}$ and $f_2 = \frac{S_2}{S_1+S_2}$, the apparent contact angle of the droplet in this case writes as :

$$\cos\theta_{app} = f_1 \cos\theta_1 + f_2 \cos\theta_2. \tag{2.19}$$

It is noteworthy that Eq. (2.19) can be used for treating a corrugated surface. Indeed, assuming a rough surface for which the droplet does not fill the gaps between corrugations (Fig. 2.5), the Cassie-Baxter model can be used by imposing $\theta_2 = 180°$ (flat meniscus in the gap).

2.4 Effective medium approximation

The effective medium approximation (EMA) pertains to analytical approaches which aim at describing the macroscopic properties of composite materials (Fig. 2.6) [111]. Based on the volume filling fractions and the intrinsic properties of the constituents of the composite material,

[4]The projected area of a three dimensional object is the area of the two dimensional image that this object formed when it is projected onto a given plane.

the EMA averages the multiple microscopic effects contributing to the macroscopic properties. The properties under consideration are usually the conductivity σ or the dielectric constant ε of the composite material (Fig. 2.6). There are different EMA approaches each of them being more

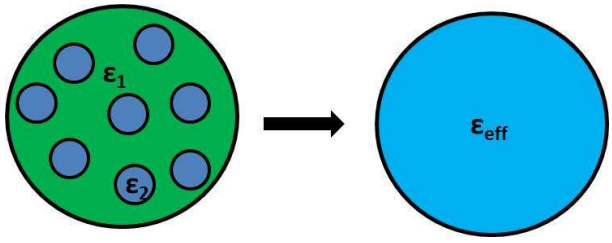

Figure 2.6: Composite material and its corresponding effective approximation.

or less accurate in distinct conditions according to *e.g.* the geometrical shape of the constituents of the composite material [111]. However, all of them rely on the Clausius-Mossotti relation which allows linking the microscopic polarizability of a medium and its macroscopic dielectric constant [111]. For example, the Bruggman's theory allows deriving the effective properties of a system made of a mixture of components with different arbitrary properties while the Maxwell-Garnett theory is employed for deriving the effective properties of a system made of inclusions in a host material. In both Bruggman and Maxwell-Garnett theories, the shape of the inclusions (sphere, ellipsoid, ...) can be taken into account through the use of depolarizing factors. Although appearing as simple, the application of EMA may easily become restrictive and must, when allowed, be handled with great care. The ambiguity about the validity of the results provided by such approximations as well as their underlying hypothesis will be especially illustrated in Chapter 7 in the framework of nanocorrugated surfaces approximated by an effective multilayer.

2.5 Anti-reflective surfaces

Anti-reflective surfaces aim at reducing the reflection of light upon them and/or improving the light absorption or transmission. Such surfaces can be made either using a thin film or micro-nanostructures (Fig. 2.7) [112].

2.5.1 Thin film

The thin film forms two interfaces producing both reflected waves (Fig. 2.7a). The refractive index and the film thickness d are optimized for obtaining minimal reflection loss through destructive interference between these reflected waves [112], *i.e.* :

$$2n_{TF}d\cos(\theta) = (m + \frac{1}{2})\lambda, \tag{2.20}$$

and

$$n_0 n_{TF} = n_{sub}^2 \tag{2.21}$$

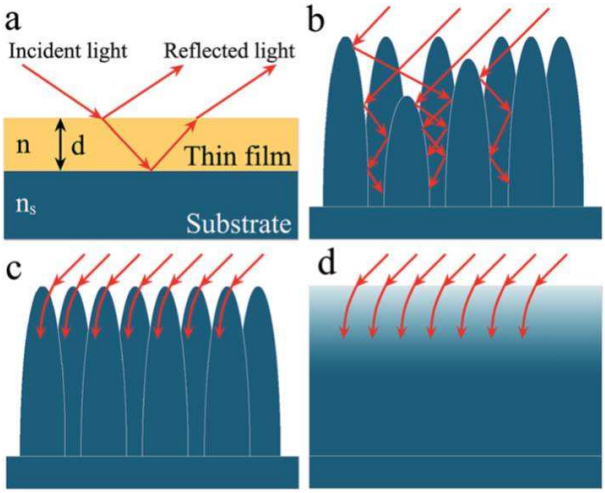

Figure 2.7: (a) Anti reflective thin film. (b) Anti reflective microstructure. (c) Anti reflective nanostructure and (d) its corresponding effective description [113].

where n_0 and n_{sub} are respectively the refractive indexes of the incident medium and the substrate, n_{TF} and d are respectively the refractive index and the thickness of the thin film, θ is the incident angle of the light, λ is the wavelength of the incident light and m is an integer. At normal incidence and for $m = 0$, (2.20) reduces to :

$$d = \frac{\lambda}{4n_{TF}}. \tag{2.22}$$

In this specific case, the antireflective thin film is a called quarter wavelength film. However, since the thickness and the refractive index of the thin film are wavelength dependent and the interference depends on the incident wave polarization and the incident angle, the anti-reflective performance of the thin film becomes very specific.

2.5.2 Micro/nanostructures

The use of micro or nanostructures is much less restrictive [112]. Considering a microstructure for which the size of the structuration is much larger than the light wavelength and the depth and space between individual structure are at the same scale as the light wavelength. In this case, the light rays are trapped in the inter-structure gaps leading to multiple internal reflections (Fig. 2.7b). Therefore, the incident light can be more easily absorbed or transmitted, reducing the reflection in the incident light wavelength range. Conversely, considering a nanostructure for which all the relevant sizes of the structuration are less than the wavelength. In this case, the light is insensitive to the details of the structure but only ”sees” it as an effective material (Fig. 2.7c-d). If this effective material exhibits a graded refractive index, *i.e.* the index increases smoothly from a value as close as possible to the index of free space to a value that matches the index of the uniform substrate, the incident light will be progressively transmitted through the structure, which will therefore act as an anti-reflective coating.

Such effects of the nanostructure on the antireflection properties of a surface are illustrated

on Fig. 2.8 where the reflection coefficient of a polyethyelene (PE) surface was computed.

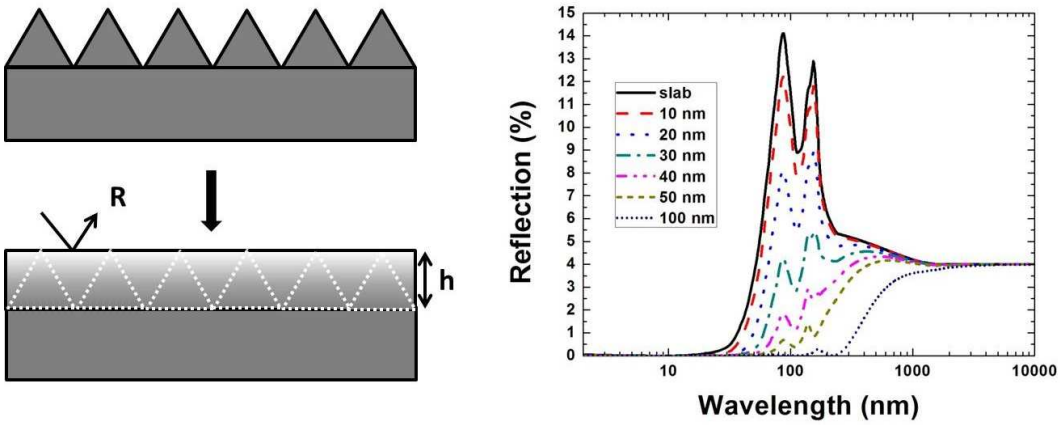

Figure 2.8: Corrugated PE surface described by a continuous effective material with a graded effective index along its thickness and its reflection coefficient (at normal incidence) for various cones height. The base of the cones was kept constant.

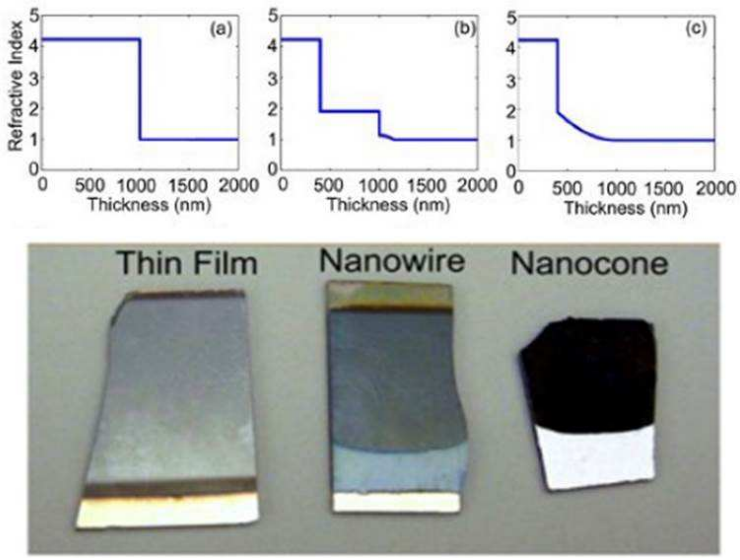

Figure 2.9: (left-up) Refractive index profile of an $a-Si:H$ thin film, (middle-up) refractive index profile of an $a-Si:H$ nanowires arrays, (right-up) refractive index profile of an $a-Si:H$ nanocones film. (left-botton) Photographs of $a-Si:H$ thin film, (middle-bottom) nanowires arrays, and (right-bottom) nanocones arrays [114].

The polyethylene surface is nanostructured with cones. Due to the cones size, the corrugated surface can be described by a continuous effective material with a graded refractive index along its thickness. The efficiency of the anti-reflective coating can be improved by increasing the cones height. Indeed, such a maneuver allows refining the graded character of the refractive index profile. As expected, the higher the cones, the lower the reflection coefficient. This figure is fully discussed in Chapter 8. A last illustration of the nanostructure antireflective coating is illustrated on Fig. 2.9 [114].

The antireflective performances of an $a-Si:H$ thin film on ITO (substrate), an $a-Si:H$ nanowires array on ITO and an $a-Si:H$ nanocones array on ITO are compared as well as their refractive index profile. As expected, the antireflection properties of the nanocones array is the most efficient due to its graded refractive index profile and therefore allows a much better absorption of the light. This efficient absorption explains the black color of the sample.

Both kinds of structures (micro and nano) are efficient whatever the polarization states of the incident light is and the incident angle is. They are therefore much more convenient than the thin film.

2.6 Scattering matrix

In optics, the scattering matrix S of a system is a matrix that connects outcoming electromagnetic states $|out\rangle$ to incoming electromagnetic states $|in\rangle$. As such, the scattering matrix can be considered as a kind of transfer function. Since both electromagnetic states are time dependent, the connection between them writes as :

$$|out(t)\rangle = S(t) \star |in(t)\rangle \,, \tag{2.23}$$

where $\star$ is the convolution product and the corresponding relation between Fourier transforms is :

$$|out(\omega)\rangle = S(\omega)\, |in(\omega)\rangle \,. \tag{2.24}$$

The study of the properties of the scattering matrix allows characterizing the properties of the physical system that it describes. A more detailed description of the scattering matrix in the framework of the Rigorous Coupled Wave Analysis method is presented in Chapter 3.

2.6.1 Zeros of the scattering matrix

The determination of the zeros of the scattering matrix is equivalent to investigating the conditions for which $|out(\omega)\rangle = 0$ with $|in(\omega)\rangle \neq 0$. Such a situation would correspond to a complete disappearance of the electromagnetic field in the far-field (propagative field) as well as in the near field (evanescent field) which is physically unacceptable. Therefore, it is assumed that the scattering matrix S does not possess any zeros.

2.6.2 Poles of the scattering matrix

The scattering matrix $S(\omega)$ allows linking the incoming electromagnetic field $|in\rangle$ and the outcoming electromagnetic field $|out\rangle$ as:

$$S^{-1}(\omega)\, |out(\omega)\rangle = |in(\omega)\rangle \,. \tag{2.25}$$

The eigen modes ω_p of the system can be introduced as solution of (2.25) in the case $|in(\omega)\rangle = 0$, *i.e.*:

$$S^{-1}(\omega_p)\,|out(\omega)\rangle = 0, \tag{2.26}$$

which is equivalent to calculate :

$$\det S^{-1}(\omega_p) = 0. \tag{2.27}$$

2.6.3 Remark

Considering Eq. (2.23), since $|in(t)\rangle$ is real because the electromagnetic field is a physically measurable quantity and thereof $|out(t)\rangle$ is real too, $S(t)$ is real as well and so $S(t) = S^*(t)$. Moreover, since the Fourier transform of $S(t)$ writes as:

$$S(t) = \frac{1}{2\pi}\int_{-\infty}^{+\infty} S(\omega)e^{-i\omega t}d\omega \tag{2.28}$$

and the Fourier transform of $S^*(t)$ as:

$$S^*(t) = \frac{1}{2\pi}\int_{-\infty}^{+\infty} S^*(\omega)e^{i\omega t}d\omega = S(t) = \frac{1}{2\pi}\int_{-\infty}^{+\infty} S^*(-\omega)e^{-i\omega t}d\omega, \tag{2.29}$$

the reality of $S(t)$ imposes $S^*(-\omega) = S(\omega)$. This useful relation will be employed in Chapter 5.

Chapter 3

The rigorous coupled-wave analysis

The rigorous coupled-wave analysis (RCWA) is a computational method in electromagnetics used to determine the optical properties of periodic dielectric structures [56, 115]. The key point of this method lies in the derivation of the scattering matrix S of the periodic system which allows linking the incoming electromagnetic field to the outcoming electromagnetic field. As a result, the reflection, transmission and absorption coefficients of the periodic dielectric structure can be evaluated. The main steps of the method are presented hereafter and follow the same framework as in Dr. Michael Sarrazin's thesis manuscript [116].

3.1 Structure description within the Fourier representation

Let us consider a dielectric planar layer exhibiting a bidimensional refractive indices periodic distribution (Fig. 3.1). The bidimensional (2D) periodicity is described by two basis vectors $\overrightarrow{a_1}$ and $\overrightarrow{a_2}$ (not necessarily orthogonal) forming the primitive cell. The permittivity or dielectric constant $\varepsilon(\overrightarrow{\rho},\omega)$ of the layer is assumed to be independent of the normal coordinate z (along the thickness of the layer) and to be a function of the lateral coordinates $\overrightarrow{\rho} = x\overrightarrow{a_1} + y\overrightarrow{a_2}$ and the frequency ω. In the primitive cell of the real space, the dielectric function is supposed to be a piecewise assembly of constant values emerging from n_l islands in a homogenous host medium s (Fig. 3.1):

$$\varepsilon(\overrightarrow{\rho},\omega) = \varepsilon_s(\omega) + \sum_{l=1}^{n_l}[\varepsilon_l(\omega) - \varepsilon_s(\omega)]\Omega_l(\overrightarrow{\rho)}, \tag{3.1}$$

where ε_s is the dielectric constant in the homogenous region, ε_l is the dielectric constant in a given island region. The periodicity implies that the primitive cell is reproduced periodically in the (x, y) plane, *i.e.* $\varepsilon(\overrightarrow{\rho} + \overrightarrow{R}) = \varepsilon(\overrightarrow{R})$ where $\overrightarrow{R} = m\overrightarrow{a_1} + p\overrightarrow{a_2}$ is a translation vector $(m, p \in \aleph)$. The geometrical domain occupied by an island is described by the Boolean function $\Omega_l(\overrightarrow{\rho})$ in such a way:

$$\Omega_l(\overrightarrow{\rho}) = \begin{cases} 1 \text{ if } \varepsilon(\overrightarrow{\rho}) = \varepsilon_l \\ 0 \text{ if } \varepsilon(\overrightarrow{\rho}) \neq \varepsilon_l \end{cases} \tag{3.2}$$

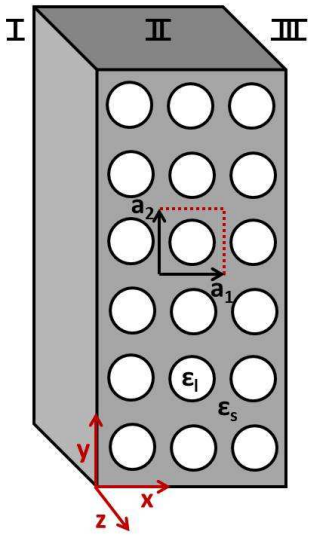

Figure 3.1: Sketch of periodic permittivity layer. The white circles are the cross sections of the cylinders running across the whole layer thickness. The primitive cell is delimited by dotted lines and the lattice vectors $\overrightarrow{a_1}$ and $\overrightarrow{a_2}$ and is assumed to enclose a single island ($n_l = 1$).

The Fourier series expansion of the Boolean function can be written as:

$$\Omega_l(\overrightarrow{\rho}) = \sum_{\overrightarrow{g}} \Omega_{l,\overrightarrow{g}} e^{i\overrightarrow{g}\cdot\overrightarrow{\rho}}, \tag{3.3}$$

where $\overrightarrow{g}$ is a reciprocal lattice vector and $\Omega_{l,\overrightarrow{g}}$ is the Fourier coefficient given by:

$$\Omega_{l,\overrightarrow{g}} = \frac{1}{\sigma}\int_{\sigma} \Omega_l(\overrightarrow{\rho}) e^{-i\overrightarrow{g}\cdot\overrightarrow{\rho}} d\overrightarrow{\rho}^2, \tag{3.4}$$

with σ the primitive cell area. The Fourier series expansion of the dielectric function writes as:

$$\varepsilon(\overrightarrow{\rho},\omega) = \sum_{\overrightarrow{g}} \varepsilon_{\overrightarrow{g}}(\omega) e^{i\overrightarrow{g}\cdot\overrightarrow{\rho}}, \tag{3.5}$$

with its Fourier coefficients $\varepsilon_{\overrightarrow{g}}(\omega)$ given by:

$$\varepsilon_{\overrightarrow{g}}(\omega) = \varepsilon_s(\omega)\delta_{\overrightarrow{g},\overrightarrow{0}} + \sum_{l=1}^{n_l}[\varepsilon_l(\omega) - \varepsilon_s(\omega)]\Omega_{l,\overrightarrow{g}} \tag{3.6}$$

where $\delta_{\overrightarrow{g};0}$ is the Kronecker symbol. From the above expressions, we can easily obtain the Fourier series expansion of $\frac{1}{\varepsilon(\overrightarrow{\rho},\omega)}$ which will be needed further:

$$\frac{1}{\varepsilon(\overrightarrow{\rho},\omega)} = \sum_{\overrightarrow{g}} \left[\frac{1}{\varepsilon(\omega)}\right]_{\overrightarrow{g}} e^{i\overrightarrow{g}\cdot\overrightarrow{\rho}}, \tag{3.7}$$

with :

$$\left[\frac{1}{\varepsilon(\omega)}\right]_{\overrightarrow{g}} = \frac{1}{\varepsilon_s(\omega)}\delta_{\overrightarrow{g},\overrightarrow{0}} + \sum_{l=1}^{n_l}\left[\frac{1}{\varepsilon_l(\omega)} - \frac{1}{\varepsilon_s(\omega)}\right]\Omega_{l,\overrightarrow{g}}. \tag{3.8}$$

3.2 Elementary patterns description within a bidimensional periodic system

The Fourier coefficients of a bidimensional island region (Eq. (3.4)) can be analytically calculated in various simple cases.

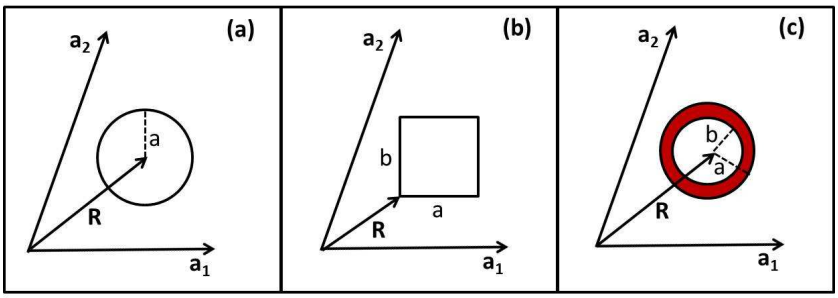

Figure 3.2: (a) Circular region. (b) Rectangular region. (c) Ring region.

3.2.1 Circular region

Let us consider a circular region of center $\overrightarrow{R}$ and radius a (Fig. 3.2 (a)). In this case, the Fourier coefficients of the Boolean function are expressed as:

$$\Omega_{\overrightarrow{g}} = \frac{2\pi a^2}{\sigma}\frac{J_1(ga)}{ga}e^{-i\overrightarrow{g}.\overrightarrow{R}}, \tag{3.9}$$

with J_1 the first-order Bessel function.

3.2.2 Rectangular region

Let us consider a rectangular region defined by an origin $\overrightarrow{R}$, a width a and a height b (Fig. 3.2 (b)). In this case, the Fourier coefficients of the Boolean function are expressed as:

$$\Omega_{\overrightarrow{g}} = \frac{ab}{\sigma}\left(\frac{e^{-ig_x a}-1}{-ig_x a}\right)\left(\frac{e^{-ig_y b}-1}{-ig_y b}\right)e^{-i\overrightarrow{g}.\overrightarrow{R}}. \tag{3.10}$$

3.2.3 Ring region

Let us consider a ring region of center $\overrightarrow{R}$ with an external radius a and an internal radius b (Fig. 3.2 (c)). In this case, the Fourier coefficients of the Boolean function are expressed as:

$$\Omega_{\overrightarrow{g}\neq\overrightarrow{0}} = \frac{e^{-i\overrightarrow{g}.\overrightarrow{R}}}{\sigma}\frac{2\pi}{g}\left[aJ_1(ga) - b.J_1(gb)\right]. \tag{3.11}$$

for $\overrightarrow{g} \neq \overrightarrow{0}$. In the case of $\overrightarrow{g} = \overrightarrow{0}$, the Fourier coefficients of the Boolean function is expressed as:

$$\Omega_{\overrightarrow{g}=\overrightarrow{0}} = \frac{2\pi}{\sigma}\frac{a^2 - b^2}{2} \tag{3.12}$$

3.3 Maxwell's equations within Fourier representation

For a periodic dielectric function, the Floquet-Bloch theorem imposes a simple form for the electric and magnetic fields:

$$\begin{bmatrix} \overrightarrow{E} \\ \overrightarrow{H} \end{bmatrix} = \sum_{\overrightarrow{g}} \begin{bmatrix} E_{x,\overrightarrow{g}}(z)\overrightarrow{e_x} + E_{y,\overrightarrow{g}}(z)\overrightarrow{e_y} + E_{z,\overrightarrow{g}}(z)\overrightarrow{e_z} \\ H_{x,\overrightarrow{g}}(z)\overrightarrow{e_x} + H_{y,\overrightarrow{g}}(z)\overrightarrow{e_y} + H_{z,\overrightarrow{g}}(z)\overrightarrow{e_z} \end{bmatrix} e^{i(\overrightarrow{k}+\overrightarrow{g})\cdot\overrightarrow{\rho}} e^{-i\omega t}, \tag{3.13}$$

where $\overrightarrow{k}$ is the photon wave vector. In a Cartesian coordinate system, Maxwell's equations for an inhomogeneous medium can be written as:

$$\overrightarrow{\nabla} \cdot (\varepsilon(x,y)\overrightarrow{E}) = 0, \tag{3.14}$$

$$\overrightarrow{\nabla} \cdot \overrightarrow{H} = 0, \tag{3.15}$$

$$\overrightarrow{\nabla} \times \overrightarrow{E} = -\mu_0 \frac{\partial}{\partial t}\overrightarrow{H}, \tag{3.16}$$

$$\overrightarrow{\nabla} \times \overrightarrow{H} = \varepsilon(x,y)\varepsilon_0 \frac{\partial}{\partial t}\overrightarrow{E}. \tag{3.17}$$

Inserting Eq. (3.5), (3.7) and (3.13) into Eq. (3.14) to (3.17), the expression of Maxwell's equations within the Fourier representation are:

$$\frac{dE_{z,\overrightarrow{g'}}}{dz} = -i \sum_{\overrightarrow{g}\,\overrightarrow{g'}} \left(\frac{1}{\varepsilon}\right)_{\overrightarrow{g'}-\overrightarrow{g}-\overrightarrow{g}} \varepsilon_{\overrightarrow{g'}}(\overrightarrow{k} + \overrightarrow{g} + \overrightarrow{g'}) \cdot \overrightarrow{E}_{//,\overrightarrow{g}}, \tag{3.18}$$

$$\frac{dH_{z,\overrightarrow{g}}}{dz} = -i(\overrightarrow{k} + \overrightarrow{g}) \cdot \overrightarrow{H}_{//,\overrightarrow{g}}, \tag{3.19}$$

$$\frac{dE_{y,\overrightarrow{g}}}{dz} = i(k_y + g_y)E_{z,\overrightarrow{g}} - i\mu_0\omega H_{x,\overrightarrow{g}}, \tag{3.20}$$

$$\frac{dE_{x,\overrightarrow{g}}}{dz} = i(k_x + g_x)E_{z,\overrightarrow{g}} + i\mu_0\omega H_{y,\overrightarrow{g}}, \tag{3.21}$$

$$H_{z,\overrightarrow{g}} = \frac{1}{\mu_0\omega}\left[(k_x + g_x)E_{y,\overrightarrow{g}} - (k_y + g_y)E_{x,\overrightarrow{g}}\right], \tag{3.22}$$

$$\frac{dH_{y,\overrightarrow{g}}}{dz} = i(k_y + g_y)H_{z,\overrightarrow{g}} + i\varepsilon_0\omega \sum_{\overrightarrow{g'}} \varepsilon_{\overrightarrow{g}-\overrightarrow{g'}} E_{x,\overrightarrow{g'}}, \tag{3.23}$$

$$\frac{dH_{x,\overrightarrow{g}}}{dz} = i(k_x + g_x)H_{z,\overrightarrow{g}} - i\varepsilon_0\omega \sum_{\overrightarrow{g'}} \varepsilon_{\overrightarrow{g}-\overrightarrow{g'}} E_{y,\overrightarrow{g'}}, \tag{3.24}$$

$$E_{z,\overrightarrow{g}} = \frac{1}{\varepsilon_0\omega} \sum_{\overrightarrow{g'}} \left(\frac{1}{\varepsilon}\right)_{\overrightarrow{g}-\overrightarrow{g'}} \left[(k_y + g_y^{'})H_{x,\overrightarrow{g'}} - (k_x + g_x^{'})H_{y,\overrightarrow{g'}}\right], \tag{3.25}$$

with $\overrightarrow{g'}$ and $\overrightarrow{g''}$ two arbitrary reciprocal lattice vectors. Equations (3.22) and (3.25) allow eliminating the longitudinal field components $E_{z,\overrightarrow{g}}$ and $H_{z,\overrightarrow{g}}$ which leaves only the transverse components $\overrightarrow{E}_{//,\overrightarrow{g}} \equiv E_{x,\overrightarrow{g}}\overrightarrow{e_x} + E_{y,\overrightarrow{g}}\overrightarrow{e_y}$ and $\overrightarrow{H}_{//,\overrightarrow{g}} \equiv H_{x,\overrightarrow{g}}\overrightarrow{e_x} + H_{y,\overrightarrow{g}}\overrightarrow{e_y}$ unknown. Such a result is important since those unknown field components are precisely the ones which remain continuous while passing through interfaces perpendicular to the z-direction. Therefore, the above equations set can be reduced to:

$$\frac{dE_{x,\overrightarrow{g}}}{dz} = \frac{i(k_x + g_x)}{\varepsilon_0\omega} \sum_{\overrightarrow{g'}} \left(\frac{1}{\varepsilon}\right)_{\overrightarrow{g}-\overrightarrow{g'}} \left[(k_y + g_y^{'})H_{x,\overrightarrow{g'}} - (k_x + g_x^{'})H_{y,\overrightarrow{g'}}\right] + i\mu_0\omega H_{y,\overrightarrow{g}}, \tag{3.26}$$

$$\frac{dE_{y,\overrightarrow{g}}}{dz} = \frac{i(k_y + g_y)}{\varepsilon_0\omega} \sum_{\overrightarrow{g'}} \left(\frac{1}{\varepsilon}\right)_{\overrightarrow{g}-\overrightarrow{g'}} \left[(k_y + g_y^{'})H_{x,\overrightarrow{g'}} - (k_x + g_x^{'})H_{y,\overrightarrow{g'}}\right] - i\mu_0\omega H_{x,\overrightarrow{g}}, \tag{3.27}$$

$$\frac{dH_{x,\overrightarrow{g}}}{dz} = \frac{i(k_x + g_x)}{\mu_0\omega} \left[(k_x + g_x)E_{y,\overrightarrow{g}} - (k_y + g_y)E_{x,\overrightarrow{g}}\right] - i\varepsilon_0\omega \sum_{\overrightarrow{g'}} \varepsilon_{\overrightarrow{g}-\overrightarrow{g'}} E_{y,\overrightarrow{g'}}, \tag{3.28}$$

$$\frac{dH_{y,\overrightarrow{g}}}{dz} = \frac{i(k_y + g_y)}{\mu_0\omega} \left[(k_x + g_x)E_{y,\overrightarrow{g}} - (k_y + g_y)E_{x,\overrightarrow{g}}\right] + i\varepsilon_0\omega \sum_{\overrightarrow{g'}} \varepsilon_{\overrightarrow{g}-\overrightarrow{g'}} E_{x,\overrightarrow{g'}}. \tag{3.29}$$

Using appropriate initial conditions, the above differential equations system can be easily solved. For this purpose, solutions in homogenous regions I and III (Fig. 3.1) surrounding the inhomogeneous region II are investigated. In region I, the dielectric function takes the constant value ε_I while in region III it takes the constant value ε_{III}. In this case of constant values, Eq. (3.26) to (3.29) can be simplified and two new sets of equations can be obtained by derivation of those equations with respect to z. These two new sets are reduced to:

$$\frac{d^2}{dz^2} \begin{bmatrix} \overrightarrow{E}_{j,//,\overrightarrow{g}} \\ \overrightarrow{H}_{j,//,\overrightarrow{g}} \end{bmatrix} = - \left(\varepsilon_j(\omega)\frac{\omega^2}{c^2} - |(\overrightarrow{k_{//}} + \overrightarrow{g})|^2\right) \begin{bmatrix} \overrightarrow{E}_{j,//,\overrightarrow{g}} \\ \overrightarrow{H}_{j,//,\overrightarrow{g}} \end{bmatrix}, \tag{3.30}$$

where j = I or III and $\overrightarrow{k_{//}} = k_x\overrightarrow{e_x} + k_y\overrightarrow{e_y}$. Solutions can be easily deduced:

$$\begin{bmatrix} \overrightarrow{E}_{j,//,\overrightarrow{g}} \\ \overrightarrow{H}_{j,//,\overrightarrow{g}} \end{bmatrix} = \begin{bmatrix} \overrightarrow{A}^{+}_{j,//,\overrightarrow{g}} \\ \overrightarrow{B}^{+}_{j,//,\overrightarrow{g}} \end{bmatrix} e^{ik_{j,\overrightarrow{g},z}z} + \begin{bmatrix} \overrightarrow{A}^{-}_{j,//,\overrightarrow{g}} \\ \overrightarrow{B}^{-}_{j,//,\overrightarrow{g}} \end{bmatrix} e^{-ik_{j,\overrightarrow{g},z}z}, \tag{3.31}$$

with $k_{j,\overrightarrow{g},z} = \sqrt{\varepsilon_j(\omega)\frac{\omega^2}{c^2} - |\overrightarrow{k_{//}} + \overrightarrow{g}|^2}$ which can be real or imaginary. The transverse components of the electromagnetic field represent plane waves traveling along the ascending Oz axis ($e^{ik_{j,\overrightarrow{g},z}z}$) or descending Oz axis ($e^{-ik_{j,\overrightarrow{g},z}z}$). Moreover, according to the nature of $k_{j,\overrightarrow{g},z}$, *i.e.* real or imaginary, waves can be propagative ($k_{j,\overrightarrow{g},z}$ is real) or evanescent ($k_{j,\overrightarrow{g},z}$ is imaginary).

3.4 The polarization basis

In order to describe more explicitly the electric and magnetic fields polarization states, it is necessary to define a polarization basis linked to the reciprocal lattice (Fig. 3.3). For this purpose, the following vectors are defined in region I:

$$\overrightarrow{\mu}_{I\overrightarrow{g}} = \frac{k_{\overrightarrow{g}z}}{\sqrt{\varepsilon_I}\frac{\omega}{c}} \frac{\overrightarrow{k_{//}} + \overrightarrow{g}}{\left|\overrightarrow{k_{//}} + \overrightarrow{g}\right|}, \tag{3.32}$$

$$\overrightarrow{\eta}_{I\overrightarrow{g}} = \frac{\overrightarrow{k_{//}} + \overrightarrow{g}}{\left|\overrightarrow{k_{//}} + \overrightarrow{g}\right|} \times \overrightarrow{e}_z, \tag{3.33}$$

$$\overrightarrow{\chi}^{\pm}_{I\overrightarrow{g}} = \mp \overrightarrow{\mu}_{I\overrightarrow{g}} + \frac{\left|\overrightarrow{k_{//}} + \overrightarrow{g}\right|}{\sqrt{\varepsilon_I}\frac{\omega}{c}} \overrightarrow{e}_z. \tag{3.34}$$

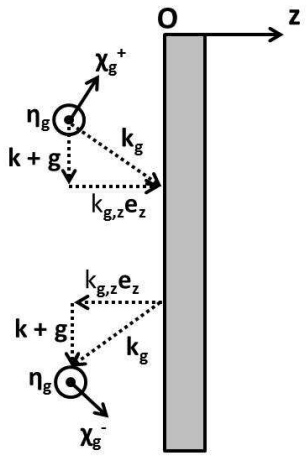

Figure 3.3: Sketch of the polarization basis.

It is noteworthy that this formulation, presented for the homogenous region I, remains the same for the homogenous region III. The expressions of the electric and magnetic fields in the polarization basis are:

$$\begin{aligned}\overrightarrow{E}_I(\overrightarrow{\rho},z) &= \sum_{\overrightarrow{g}}[N^+_{I\overrightarrow{g}}\,\overrightarrow{\eta}_{\overrightarrow{g}}e^{ik_{I\overrightarrow{g}z}(z-z_I)} + N^-_{I\overrightarrow{g}}\,\overrightarrow{\eta}_{\overrightarrow{g}}e^{-ik_{I\overrightarrow{g}z}(z-z_I)} \\ &\quad + X^+_{I\overrightarrow{g}}\,\overrightarrow{\chi}^+_{I\overrightarrow{g}}e^{ik_{I\overrightarrow{g}z}(z-z_I)} + X^-_{I\overrightarrow{g}}\,\overrightarrow{\chi}^-_{I\overrightarrow{g}}e^{-ik_{I\overrightarrow{g}z}(z-z_I)}]e^{i(\overrightarrow{k}+\overrightarrow{g}).\overrightarrow{\rho}}, \qquad (3.35)\end{aligned}$$

$$\begin{aligned}\overrightarrow{H}_I(\overrightarrow{\rho},z) &= \frac{\sqrt{\varepsilon_I}}{c\mu_0}\sum_{\overrightarrow{g}}[-N^+_{I\overrightarrow{g}}\,\overrightarrow{\chi}^+_{I\overrightarrow{g}}e^{ik_{I\overrightarrow{g}z}(z-z_I)} - N^-_{I\overrightarrow{g}}\,\overrightarrow{\chi}^-_{I\overrightarrow{g}}e^{-ik_{I\overrightarrow{g}z}(z-z_I)} \\ &\quad + X^+_{I\overrightarrow{g}}\,\overrightarrow{\eta}_{\overrightarrow{g}}e^{ik_{I\overrightarrow{g}z}(z-z_I)} + X^-_{I\overrightarrow{g}}\,\overrightarrow{\eta}_{\overrightarrow{g}}e^{-ik_{I\overrightarrow{g}z}(z-z_I)}]e^{i(\overrightarrow{k}+\overrightarrow{g}).\overrightarrow{\rho}}. \qquad (3.36)\end{aligned}$$

Their respective components parallel to the surface can be written as[1]:

$$\begin{aligned}\overrightarrow{E}_{//,I}(z) &= N^+_{I\overrightarrow{g}}\,\overrightarrow{\eta}_{\overrightarrow{g}}e^{ik_{I\overrightarrow{g}z}(z-z_I)} + N^-_{I\overrightarrow{g}}\,\overrightarrow{\eta}_{\overrightarrow{g}}e^{-ik_{I\overrightarrow{g}z}(z-z_I)} \\ &\quad - X^+_{I\overrightarrow{g}}\,\overrightarrow{\mu}_{I\overrightarrow{g}}e^{ik_{I\overrightarrow{g}z}(z-z_I)} + X^-_{I\overrightarrow{g}}\,\overrightarrow{\mu}_{I\overrightarrow{g}}e^{-ik_{I\overrightarrow{g}z}(z-z_I)}, \qquad (3.37)\end{aligned}$$

$$\begin{aligned}\overrightarrow{H}_{//,I}(z) &= \frac{\sqrt{\varepsilon_I}}{c\mu_0}(N^+_{I\overrightarrow{g}}\,\overrightarrow{\mu}_{I\overrightarrow{g}}e^{ik_{I\overrightarrow{g}z}(z-z_I)} - N^-_{I\overrightarrow{g}}\,\overrightarrow{\mu}_{I\overrightarrow{g}}e^{-ik_{I\overrightarrow{g}z}(z-z_I)} \\ &\quad + X^+_{I\overrightarrow{g}}\,\overrightarrow{\eta}_{\overrightarrow{g}}e^{ik_{I\overrightarrow{g}z}(z-z_I)} + X^-_{I\overrightarrow{g}}\,\overrightarrow{\eta}_{\overrightarrow{g}}e^{-ik_{I\overrightarrow{g}z}(z-z_I)}), \qquad (3.38)\end{aligned}$$

where $N^{(+,-)}_{\overrightarrow{g}}$ are the amplitudes in the s-polarization state for each diffracting orders associated to a reciprocal lattice vector $\overrightarrow{g}$ while $X^{(+,-)}_{\overrightarrow{g}}$ are the corresponding amplitudes in the p-polarization state. The signs $\pm$ indicate the direction of propagation of the field: $(+)$ along the ascending Oz axis, $(-)$ in the opposite way. According to Eq. (3.37) and (3.38), the parallel components of the electric and magnetic fields can now be expressed in terms of these field amplitudes:

$$\overrightarrow{E}_{//}(z_I) = N^+_{I\overrightarrow{g}}\,\overrightarrow{\eta}_{\overrightarrow{g}} + N^-_{I\overrightarrow{g}}\,\overrightarrow{\eta}_{\overrightarrow{g}} - X^+_{I\overrightarrow{g}}\,\overrightarrow{\mu}_{I\overrightarrow{g}} + X^-_{I\overrightarrow{g}}\,\overrightarrow{\mu}_{I\overrightarrow{g}}, \qquad (3.39)$$

$$\overrightarrow{H}_{//}(z_I) = \frac{\sqrt{\varepsilon_I}}{c\mu_0}(N^+_{I\overrightarrow{g}}\,\overrightarrow{\mu}_{I\overrightarrow{g}} - N^-_{I\overrightarrow{g}}\,\overrightarrow{\mu}_{I\overrightarrow{g}} + X^+_{I\overrightarrow{g}}\,\overrightarrow{\eta}_{\overrightarrow{g}} + X^-_{I\overrightarrow{g}}\,\overrightarrow{\eta}_{\overrightarrow{g}}), \qquad (3.40)$$

in the homogenous region I, at the interface with region II ($z = z_I$), and :

[1]We note that $\overrightarrow{\mu}_{I\overrightarrow{g}}$ is the projection of $X^{(+,-)}_{I\overrightarrow{g}}$ in the (x,y) plane.

$$\overrightarrow{E}_{//}(z_{III}) = N^{+}_{III\overrightarrow{g}}\,\overrightarrow{\eta}_{\overrightarrow{g}} + N^{-}_{III\overrightarrow{g}}\,\overrightarrow{\eta}_{\overrightarrow{g}} - X^{+}_{III\overrightarrow{g}}\,\overrightarrow{\mu}_{III\overrightarrow{g}} + X^{-}_{III\overrightarrow{g}}\,\overrightarrow{\mu}_{III\overrightarrow{g}}, \tag{3.41}$$

$$\overrightarrow{H}_{//}(z_{III}) = \frac{\sqrt{\varepsilon_I}}{c\mu_0}(N^{+}_{III\overrightarrow{g}}\,\overrightarrow{\mu}_{III\overrightarrow{g}} - N^{-}_{III\overrightarrow{g}}\,\overrightarrow{\mu}_{III\overrightarrow{g}} + X^{+}_{III\overrightarrow{g}}\,\overrightarrow{\eta}_{\overrightarrow{g}} + X^{-}_{III\overrightarrow{g}}\,\overrightarrow{\eta}_{\overrightarrow{g}}), \tag{3.42}$$

in the homogenous region III, at the interface with region II ($z = z_{III}$). Based on the above equations, two matrices, V and U, can be defined in order to link the electromagnetic fields in the Cartesian basis to the field amplitudes in the polarization basis:

$$\begin{bmatrix} E_{x,\overrightarrow{g}}(z_I) \\ E_{y,\overrightarrow{g}}(z_I) \\ H_{x,\overrightarrow{g}}(z_I) \\ H_{x,\overrightarrow{g}}(z_I) \end{bmatrix} = \begin{bmatrix} \eta_{x\overrightarrow{g}} & -\mu_{xI\overrightarrow{g}} & \eta_{x\overrightarrow{g}} & \mu_{xI\overrightarrow{g}} \\ \eta_{y\overrightarrow{g}} & -\mu_{yI\overrightarrow{g}} & \eta_{y\overrightarrow{g}} & \mu_{yI\overrightarrow{g}} \\ \frac{\sqrt{\varepsilon_I}}{c\mu_0}\mu_{xI\overrightarrow{g}} & \frac{\sqrt{\varepsilon_I}}{c\mu_0}\eta_{x\overrightarrow{g}} & -\frac{\sqrt{\varepsilon_I}}{c\mu_0}\mu_{xI\overrightarrow{g}} & \frac{\sqrt{\varepsilon_I}}{c\mu_0}\eta_{x\overrightarrow{g}} \\ \frac{\sqrt{\varepsilon_I}}{c\mu_0}\mu_{yI\overrightarrow{g}} & \frac{\sqrt{\varepsilon_I}}{c\mu_0}\eta_{y\overrightarrow{g}} & -\frac{\sqrt{\varepsilon_I}}{c\mu_0}\mu_{yI\overrightarrow{g}} & \frac{\sqrt{\varepsilon_I}}{c\mu_0}\eta_{y\overrightarrow{g}} \end{bmatrix} \begin{bmatrix} N^{+}_{I,\overrightarrow{g}} \\ X^{+}_{I,\overrightarrow{g}} \\ N^{-}_{I,\overrightarrow{g}} \\ X^{-}_{I,\overrightarrow{g}} \end{bmatrix} \equiv V \begin{bmatrix} N^{+}_{I,\overrightarrow{g}} \\ X^{+}_{I,\overrightarrow{g}} \\ N^{-}_{I,\overrightarrow{g}} \\ X^{-}_{I,\overrightarrow{g}} \end{bmatrix}, \tag{3.43}$$

and :

$$\begin{bmatrix} N^{+}_{I,\overrightarrow{g}} \\ X^{+}_{I,\overrightarrow{g}} \\ N^{-}_{I,\overrightarrow{g}} \\ X^{-}_{I,\overrightarrow{g}} \end{bmatrix} = \Delta_{I,\overrightarrow{g}} \begin{bmatrix} \mu_{yI\overrightarrow{g}} & -\mu_{xI\overrightarrow{g}} & -\frac{c\mu_0}{\sqrt{\varepsilon_I}}\eta_{y\overrightarrow{g}} & \frac{c\mu_0}{\sqrt{\varepsilon_I}}\eta_{x\overrightarrow{g}} \\ \eta_{y\overrightarrow{g}} & -\eta_{x\overrightarrow{g}} & \frac{c\mu_0}{\sqrt{\varepsilon_I}}\mu_{yI\overrightarrow{g}} & -\frac{c\mu_0}{\sqrt{\varepsilon_I}}\mu_{xI\overrightarrow{g}} \\ \mu_{yI\overrightarrow{g}} & -\mu_{xI\overrightarrow{g}} & \frac{c\mu_0}{\sqrt{\varepsilon_I}}\eta_{y\overrightarrow{g}} & -\frac{c\mu_0}{\sqrt{\varepsilon_I}}\eta_{x\overrightarrow{g}} \\ -\eta_{y\overrightarrow{g}} & \eta_{x\overrightarrow{g}} & \frac{c\mu_0}{\sqrt{\varepsilon_I}}\mu_{yI\overrightarrow{g}} & -\frac{c\mu_0}{\sqrt{\varepsilon_I}}\mu_{xI\overrightarrow{g}} \end{bmatrix} \begin{bmatrix} E_{x,\overrightarrow{g}}(z_I) \\ E_{y,\overrightarrow{g}}(z_I) \\ H_{x,\overrightarrow{g}}(z_I) \\ H_{x,\overrightarrow{g}}(z_I) \end{bmatrix} \equiv U \begin{bmatrix} E_{x,\overrightarrow{g}}(z_I) \\ E_{y,\overrightarrow{g}}(z_I) \\ H_{x,\overrightarrow{g}}(z_I) \\ H_{x,\overrightarrow{g}}(z_I) \end{bmatrix}, \tag{3.44}$$

where $\Delta_{I,\overrightarrow{g}} = \sqrt{\varepsilon_I}\frac{\omega}{2k_{I\overrightarrow{g}z}c}$. It is obvious that this formulation, presented for the homogenous region I, remains the same for the homogenous region III.

3.5 The transfer matrix T

The fields representation within homogenous regions requires to work with the coefficients $N^{+}_{\overrightarrow{g}}$, $N^{-}_{\overrightarrow{g}}$, $X^{+}_{\overrightarrow{g}}$, $X^{-}_{\overrightarrow{g}}$ which can be ordered as as vector:

$$\begin{bmatrix} \overline{N}^{+} \\ \overline{X}^{+} \\ \overline{N}^{-} \\ \overline{X}^{-} \end{bmatrix}, \tag{3.45}$$

with :

$$\overline{N}^{+} = \begin{bmatrix} N^{+}_{\overrightarrow{g}_1} \\ N^{+}_{\overrightarrow{g}_2} \\ \dots \\ N^{+}_{\overrightarrow{g}_n} \end{bmatrix}, \quad \overline{N}^{-} = \begin{bmatrix} N^{-}_{\overrightarrow{g}_1} \\ N^{-}_{\overrightarrow{g}_2} \\ \dots \\ N^{-}_{\overrightarrow{g}_n} \end{bmatrix} \tag{3.46}$$

$$\overline{X}^{+} = \begin{bmatrix} X^{+}_{\overrightarrow{g}_1} \\ X^{+}_{\overrightarrow{g}_2} \\ ... \\ X^{+}_{\overrightarrow{g}_n} \end{bmatrix}, \ \overline{X}^{-} = \begin{bmatrix} X^{-}_{\overrightarrow{g}_1} \\ X^{-}_{\overrightarrow{g}_2} \\ ... \\ X^{-}_{\overrightarrow{g}_n} \end{bmatrix}. \tag{3.47}$$

According to Maxwell's equations linearity, a transfer matrix T can be defined in order to link the coefficients in region I to the coefficients in region III as:

$$\begin{bmatrix} \overline{N}^{+}_{I} \\ \overline{X}^{+}_{I} \\ \overline{N}^{-}_{I} \\ \overline{X}^{-}_{I} \end{bmatrix} = \begin{bmatrix} T^{++}_{NN} & T^{++}_{NX} & T^{+-}_{NN} & T^{+-}_{NX} \\ T^{++}_{XN} & T^{++}_{XX} & T^{+-}_{XN} & T^{+-}_{XX} \\ T^{-+}_{NN} & T^{-+}_{NX} & T^{--}_{NN} & T^{--}_{NX} \\ T^{-+}_{XN} & T^{-+}_{XX} & T^{--}_{XN} & T^{--}_{XX} \end{bmatrix} \begin{bmatrix} \overline{N}^{+}_{III} \\ \overline{X}^{+}_{III} \\ \overline{N}^{-}_{III} \\ \overline{X}^{-}_{III} \end{bmatrix}. \tag{3.48}$$

Moreover, Eq. (3.26) to (3.29) can take the following matrix form:

$$\frac{d}{dz} \begin{bmatrix} \overline{E}_x(z_I) \\ \overline{E}_y(z_I) \\ \overline{H}_x(z_I) \\ \overline{H}_y(z_I) \end{bmatrix} = \begin{bmatrix} A^{xx}_{EE} & A^{xy}_{EE} & A^{xx}_{EH} & A^{xy}_{EH} \\ A^{yx}_{EE} & A^{yy}_{EE} & A^{yx}_{EH} & A^{yy}_{EH} \\ A^{xx}_{HE} & A^{xy}_{HE} & A^{xx}_{HH} & A^{xy}_{HH} \\ A^{yx}_{HE} & A^{yy}_{HE} & A^{yx}_{HH} & A^{yy}_{HH} \end{bmatrix} \begin{bmatrix} \overline{E}_x(z_{III}) \\ \overline{E}_y(z_{III}) \\ \overline{H}_x(z_{III}) \\ \overline{H}_y(z_{III}) \end{bmatrix}, \tag{3.49}$$

with the corresponding solution

$$\begin{bmatrix} \overline{E}_x(z_I) \\ \overline{E}_y(z_I) \\ \overline{H}_x(z_I) \\ \overline{H}_y(z_I) \end{bmatrix} = \exp\left\{ \begin{bmatrix} A^{xx}_{EE} & A^{xy}_{EE} & A^{xx}_{EH} & A^{xy}_{EH} \\ A^{yx}_{EE} & A^{yy}_{EE} & A^{yx}_{EH} & A^{yy}_{EH} \\ A^{xx}_{HE} & A^{xy}_{HE} & A^{xx}_{HH} & A^{xy}_{HH} \\ A^{yx}_{HE} & A^{yy}_{HE} & A^{yx}_{HH} & A^{yy}_{HH} \end{bmatrix} (z_I - z_{III}) \right\} \begin{bmatrix} \overline{E}_x(z_{III}) \\ \overline{E}_y(z_{III}) \\ \overline{H}_x(z_{III}) \\ \overline{H}_y(z_{III}) \end{bmatrix} \equiv e^{A(z_I - z_{III})} \begin{bmatrix} \overline{E}_x(z_{III}) \\ \overline{E}_y(z_{III}) \\ \overline{H}_x(z_{III}) \\ \overline{H}_y(z_{III}) \end{bmatrix}. \tag{3.50}$$

It is noteworthy that such a matrix exponent can be faithfully calculated *via* the Padé exponent technique [116]. The transfer matrix T, which relates the fields amplitude in the polarization basis, can be obtained via the following matrices combination:

$$T = U e^{A(z_I - z_{III})} V \tag{3.51}$$

3.6 The scattering matrix S

The transfer matrix T, as defined above, allows to determine fields amplitude in region I from the fields amplitude in region III. Its abridged expression can be written as:

$$T = \begin{bmatrix} T^{++} & T^{+-} \\ T^{-+} & T^{--} \end{bmatrix}. \tag{3.52}$$

However, while dealing with a scattering problem, the outcoming fields amplitudes $(\overline{N}^{+}_{III}, \overline{X}^{+}_{III,} \overline{N}^{-}_{I}, \overline{X}^{-}_{I})$ are required to be defined from the incoming fields amplitudes $(\overline{N}^{+}_{I}, \overline{X}^{+}_{I,} \overline{N}^{-}_{III}, \overline{X}^{-}_{III})$. Such a link can be done via the scattering matrix S:

$$\begin{bmatrix} \overline{N}_{III}^{+} \\ \overline{X}_{III}^{+} \\ \overline{N}_{I}^{-} \\ \overline{X}_{I}^{-} \end{bmatrix} = \begin{bmatrix} S_{NN}^{++} & S_{NX}^{++} & S_{NN}^{+-} & S_{NX}^{+-} \\ S_{XN}^{++} & S_{XX}^{++} & S_{XN}^{+-} & S_{XX}^{+-} \\ S_{NN}^{-+} & S_{NX}^{-+} & S_{NN}^{--} & S_{NX}^{--} \\ S_{XN}^{-+} & S_{XX}^{-+} & S_{XN}^{--} & S_{XX}^{--} \end{bmatrix} \begin{bmatrix} \overline{N}_{I}^{+} \\ \overline{X}_{I}^{+} \\ \overline{N}_{III}^{-} \\ \overline{X}_{III}^{-} \end{bmatrix}, \tag{3.53}$$

where S can be simply written as :

$$S = \begin{bmatrix} S^{++} & S^{+-} \\ S^{-+} & S^{--} \end{bmatrix}, \tag{3.54}$$

with S^{++} and S^{--} generalizing the transmission Fresnel coefficients and S^{+-} and S^{-+} generalizing the reflection Fresnel coefficients (Fig. 3.4). The elements of the scattering matrix S

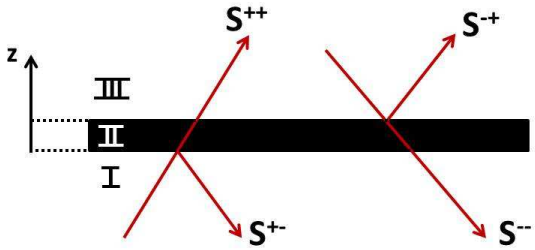

Figure 3.4: Representation of the elements of the scattering matrix.

can be expressed in terms of the elements of the transfer matrix T:

$$S^{++} = \left[T^{++}\right]^{-1}, \tag{3.55}$$

$$S^{+-} = -\left[T^{++}\right]^{-1} T^{+-}, \tag{3.56}$$

$$S^{-+} = T^{-+}\left[T^{++}\right]^{-1}, \tag{3.57}$$

$$S^{--} = T^{--} - T^{-+}\left[T^{++}\right]^{-1} T^{+-}. \tag{3.58}$$

3.7 Scattering matrices assembly

So far, the electromagnetic field propagation through a single inhomogeneous periodic layer has been considered with its corresponding Fourier description *via* the scattering matrix formalism. However, the underlying success condition of this method is the thickness of the layer. Considering the computation of the electromagnetic field propagation through a thick layer (typically of the order of the wavelength), numerical stability issues occur because of numerical integrations involving non-well conditioned matrices. In this specific case, the best solution is to split the layer into several layers[2], evaluate the individual scattering matrices and then combine them

[2]Empirically, it can be shown that a layer thickness smaller than $\lambda/10$ ensures stable computation of the scattering matrix elements from the transfer matrix elements. The assembly of such scattering matrices can be shown to be stable.

for obtaining the global scattering matrix of the system Let us consider a scattering matrix S corresponding to two successive layers 1 and 2 for which each individual scattering matrix S_1 and S_2 are known (Fig. 3.5). Let us denote the following scattering matrices:

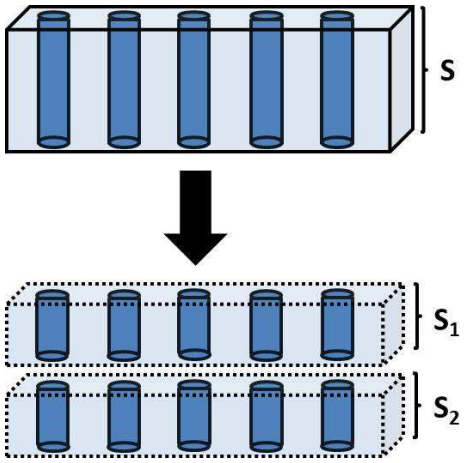

Figure 3.5: Single layer represented by a scattering matrix S split into two layers represented by two scattering matrices S_1 and S_2.

$$S = \begin{bmatrix} S^{++} & S^{+-} \\ S^{-+} & S^{--} \end{bmatrix}, \tag{3.59}$$

for the global system,

$$S_1 = \begin{bmatrix} S_1^{++} & S_1^{+-} \\ S_1^{-+} & S_1^{--} \end{bmatrix}, \tag{3.60}$$

for layer 1, and

$$S_2 = \begin{bmatrix} S_2^{++} & S_2^{+-} \\ S_2^{-+} & S_2^{--} \end{bmatrix}, \tag{3.61}$$

for layer 2. It can be easily shown that the relations below allow calculating the scattering matrix S elements *via* the scattering matrices S_1 and S_2 elements:

$$S^{++} = S_2^{++}(1 - S_1^{+-}S_2^{-+})^{-1}S_1^{++}, \tag{3.62}$$

$$S^{+-} = S_2^{+-} + S_2^{++}(1 - S_1^{+-}S_2^{-+})^{-1}S_1^{+-}S_2^{--}, \tag{3.63}$$

$$S^{-+} = S_1^{-+} + S_1^{--}S_2^{-+}(1 - S_1^{+-}S_2^{-+})^{-1}S_1^{++}, \tag{3.64}$$

$$S^{--} = S_1^{--}\left(1 + S_2^{-+}(1 - S_1^{+-}S_2^{-+})^{-1}S_1^{+-}\right)S_2^{--}, \tag{3.65}$$

with 1 the identity matrix.

3.8 Poynting vectors, R, T, A coefficients

The Poynting vector flux refers to the electromagnetic power transmitted through the layer cross section area. Such a vector allows calculating the transmission and reflection coefficients as well as the energy loss within the layer. Considering the area σ of the primitive cell, the electromagnetic power transmitted therethrough can be obtained by integrating the Poynting vector:

$$J = \int_{\sigma} \frac{1}{2} \Re(\overrightarrow{E} \times \overrightarrow{H}^{*}) \cdot \overrightarrow{e}_{z} \, dS. \tag{3.66}$$

Within the field representation developed above, the following expressions are obtained:

$$J_{I}^{+} = \frac{\sigma}{2\mu_{0}\omega} \sum_{\overrightarrow{g}} k_{I\overrightarrow{g}z} \left[\left| N_{I\overrightarrow{g}}^{+} \right|^{2} + \left| X_{I\overrightarrow{g}}^{+} \right|^{2} \right] \Theta(\varepsilon_{I}(\omega) \frac{\omega^{2}}{c^{2}} - \left| \overrightarrow{k_{//}} + \overrightarrow{g} \right|^{2}), \tag{3.67}$$

for the incident flux in region I,

$$J_{III}^{+} = \frac{\sigma}{2\mu_{0}\omega} \sum_{\overrightarrow{g}} k_{III\overrightarrow{g}z} \left[\left| N_{III\overrightarrow{g}}^{+} \right|^{2} + \left| X_{III\overrightarrow{g}}^{+} \right|^{2} \right] \Theta(\varepsilon_{III}(\omega) \frac{\omega^{2}}{c^{2}} - \left| \overrightarrow{k_{//}} + \overrightarrow{g} \right|^{2}), \tag{3.68}$$

for the transmitted flux in region III, and:

$$J_{I}^{-} = -\frac{\sigma}{2\mu_{0}\omega} \sum_{\overrightarrow{g}} k_{I\overrightarrow{g}z} \left[\left| N_{I\overrightarrow{g}}^{-} \right|^{2} + \left| X_{I\overrightarrow{g}}^{-} \right|^{2} \right] \Theta(\varepsilon_{I}(\omega) \frac{\omega^{2}}{c^{2}} - \left| \overrightarrow{k_{//}} + \overrightarrow{g} \right|^{2}), \tag{3.69}$$

for the reflected flux in region I, with $\Theta(x) = 1$ if $x > 0$ and $\Theta(x) = 0$ otherwise. Therefore, the reflection coefficient R and the transmission coefficient T are written as:

$$R = |\frac{J_{I}^{-}}{J_{I}^{+}}|, \tag{3.70}$$

$$T = |\frac{J_{III}^{+}}{J_{I}^{+}}|, \tag{3.71}$$

with the absorption (loss) coefficient defined as $A = 1 - R - T$. Note the both R and T include the contribution of all diffraction orders.

Chapter 4

The quantum vacuum fluctuations

This chapter sets the general framework of the Lifshitz-van der Waals interactions : the quantum vacuum fluctuations of the electromagnetic field. The main steps of the quantization of the free electromagnetic field are firstly exposed, leading naturally to the existence of the zero point energy. From this statement, the associated quantum vacuum fluctuations of the electromagnetic field are deduced.

4.1 The free fields

Let us consider a classical electromagnetic field in vacuum, in the absence of any sources of charges or currents. The electric and magnetic field vectors, $\overrightarrow{E}(\overrightarrow{r},t)$ and $\overrightarrow{B}(\overrightarrow{r},t)$, at the space-time point $(\overrightarrow{r},t)$ can be expressed in terms of the vector potential $\overrightarrow{A}(\overrightarrow{r},t)$ by [117] :

$$\overrightarrow{E}(\overrightarrow{r},t) = -\frac{\partial}{\partial t}\overrightarrow{A}(\overrightarrow{r},t), \tag{4.1}$$

$$\overrightarrow{B}(\overrightarrow{r},t) = \overrightarrow{\nabla}\times\overrightarrow{A}(\overrightarrow{r},t). \tag{4.2}$$

The vector potential $\overrightarrow{A}(\overrightarrow{r},t)$ satisfies the homogeneous wave equation :

$$-\nabla^2\overrightarrow{A}(\overrightarrow{r},t)+\frac{1}{c^2}\frac{\partial^2}{\partial t^2}\overrightarrow{A}(\overrightarrow{r},t)=0, \tag{4.3}$$

and the Coulomb gauge :

$$\overrightarrow{\nabla}.\overrightarrow{A}(\overrightarrow{r},t)=0. \tag{4.4}$$

These conditions define the so-called free fields which are supposed to exist even without sources. Classically, the absence of sources should cancel out the electromagnetic field. However, the quantum mechanics allows the existence of such free fields, as it will be demonstrated further, which justifies *ex post facto* this approach.

The solution of Eq. (4.3), restricted to a cubic volume V such as $V=L^3$, can be written as

the superposition of progressive waves, such as :

$$\overrightarrow{A}(\overrightarrow{r},t)=\sum_{\overrightarrow{k},\sigma}\sqrt{\frac{\hbar}{2\omega_{\overrightarrow{k}}\varepsilon_0 V}}\left(\overrightarrow{\eta}_{\overrightarrow{k},\sigma}a_{\overrightarrow{k},\sigma}e^{i(\overrightarrow{k}.\overrightarrow{r}-\omega_{\overrightarrow{k}}t)}+\overrightarrow{\eta}^{*}_{\overrightarrow{k},\sigma}a^{*}_{\overrightarrow{k},\sigma}e^{-i(\overrightarrow{k}.\overrightarrow{r}-\omega_{\overrightarrow{k}}t)}\right), \tag{4.5}$$

where $\overrightarrow{k}$ is the photon wave vector, σ is the polarization state, $\overrightarrow{\eta}_{\overrightarrow{k},\sigma}$ are unit basis vectors and $a_{\overrightarrow{k},\sigma}$ are the constant complex coefficients describing the vector potential. It is noteworthy to stress that the Planck's constant $\hbar$ is artificially introduced in Eq. (4.5) although no quantum aspects have been consired yet. Its use will be justified further. Since the volume V in which the solution is defined will be later extended to the entire free space, Born-von Karman boundary conditions are applied[1]. Therefore, periodic functions, for which the periodicity coincides with the volume dimensions, must be employed. The periodicity constraint restricts the photon wave vectors $\overrightarrow{k}$ to discrete values as :

$$\begin{aligned} k_x &= \frac{2\pi}{L}\nu_x, \\ k_y &= \frac{2\pi}{L}\nu_y, \\ k_z &= \frac{2\pi}{L}\nu_{z.} \end{aligned} \tag{4.6}$$

where ν_i are integers. From Eqs. (4.1), (4.2) and (4.5), the free fields can be written as :

$$\overrightarrow{E}(\overrightarrow{r},t) = i\sum_{\overrightarrow{k},\sigma}\sqrt{\frac{\hbar\omega_{\overrightarrow{k}}}{2\varepsilon_0 V}}\left(\overrightarrow{\eta}_{\overrightarrow{k},\sigma}a_{\overrightarrow{k},\sigma}e^{i(\overrightarrow{k}.\overrightarrow{r}-\omega_{\overrightarrow{k}}t)}+\overrightarrow{\eta}^{*}_{\overrightarrow{k},\sigma}a^{*}_{\overrightarrow{k},\sigma}e^{-i(\overrightarrow{k}.\overrightarrow{r}-\omega_{\overrightarrow{k}}t)}\right), \tag{4.7}$$

$$\begin{aligned} \overrightarrow{B}(\overrightarrow{r},t) = -\frac{i}{c}\sum_{\overrightarrow{k},\sigma}\sqrt{\frac{\hbar\omega_{\overrightarrow{k}}}{2\varepsilon_0 V}}\Big((\overrightarrow{\eta}_{\overrightarrow{k},\sigma}\times\overrightarrow{k})a_{\overrightarrow{k},\sigma}e^{i(\overrightarrow{k}.\overrightarrow{r}-\omega_{\overrightarrow{k}}t)}+ \\ (\overrightarrow{\eta}^{*}_{\overrightarrow{k},\sigma}\times\overrightarrow{k})a^{*}_{\overrightarrow{k},\sigma}e^{-i(\overrightarrow{k}.\overrightarrow{r}-\omega_{\overrightarrow{k}}t)}\Big). \end{aligned} \tag{4.8}$$

4.2 The classical Hamiltonian

The classical Hamiltonian H of the electromagnetic field, which corresponds to the energy of the electromagnetic field, writes as:

$$H=\frac{1}{2}\int_V\left[\varepsilon_0\left|\overrightarrow{E}(\overrightarrow{r},t)\right|^2+\frac{1}{\mu_0}\left|\overrightarrow{B}(\overrightarrow{r},t)\right|^2\right]d^3\overrightarrow{r} \tag{4.9}$$

where the bracketed term corresponds to the energy of the electromagnetic field stored at point $\overrightarrow{r}$ in the volume V at time t. At this stage, it is noteworthy to stress that the bracketed term can also be assimilated to a pressure inside the volume, *i.e.* the so-called radiation pressure. By integrating the expressions of the free fields given by Eqs. (4.7) and (4.8) in Eq. (4.9), it can

[1] Born-von Karman boundary conditions are periodic boundary conditions which impose that the wave function must be periodic on a cubic lattice formed by the cubic volume V.

be shown that the classical Hamiltonian writes as [117]:

$$H = \frac{1}{2} \sum_{\overrightarrow{k},\sigma} \hbar\omega_{\overrightarrow{k}} \left[a_{\overrightarrow{k},\sigma}(t) a^*_{\overrightarrow{k},\sigma}(t) + a^*_{\overrightarrow{k},\sigma}(t) a_{\overrightarrow{k},\sigma}(t) \right], \tag{4.10}$$

where $a_{\overrightarrow{k},\sigma}(t) = a_{\overrightarrow{k},\sigma} e^{-i\omega_{\overrightarrow{k}} t}$. For the purpose of field quantization, it is desirable to rewrite H in a more common form by introducing a pair of real canonical variables $q_{\overrightarrow{k},\sigma}(t)$ and $p_{\overrightarrow{k},\sigma}(t)$ defined by:

$$q_{\overrightarrow{k},\sigma}(t) = \sqrt{\frac{\hbar}{2\omega_{\overrightarrow{k}}}} \left(a_{\overrightarrow{k},\sigma}(t) + a^*_{\overrightarrow{k},\sigma}(t) \right), \tag{4.11}$$

$$p_{\overrightarrow{k},\sigma}(t) = -i\sqrt{\frac{\hbar\omega_{\overrightarrow{k}}}{2}} \left(a_{\overrightarrow{k},\sigma}(t) - a^*_{\overrightarrow{k},\sigma}(t) \right). \tag{4.12}$$

The classical Hamiltonian H therefore writes as :

$$H = \frac{1}{2} \sum_{\overrightarrow{k},\sigma} \left[p^2_{\overrightarrow{k},\sigma}(t) + \omega^2_{\overrightarrow{k}} q^2_{\overrightarrow{k},\sigma}(t) \right]. \tag{4.13}$$

One can recognize the energy of a system of independent harmonic oscillators of frequency $\omega_{\overrightarrow{k}}$, one for each ($\overrightarrow{k}$, σ) mode of the electromagnetic field.

4.3 The quantum Hamiltonian

The failover of classical mechanics to quantum mechanics is done by matching the real canonical variables to Hilbert space operators. Such operators act on the eigen state of the quantum mechanical system, *i.e.* the electromagnetic field, which is represented by an eigen state vector, a ket, $|\psi\rangle$. The eigen states of the electromagnetic field are described by photons. The quantum Hamiltonian $\mathcal{H}$ writes as :

$$\mathcal{H} = \frac{1}{2} \sum_{\overrightarrow{k},\sigma} \left[\widehat{p}^2_{\overrightarrow{k},\sigma}(t) + \omega^2_{\overrightarrow{k}} \widehat{q}^2_{\overrightarrow{k},\sigma}(t) \right], \tag{4.14}$$

where $\widehat{p}_{\overrightarrow{k},\sigma}(t)$ and $\widehat{q}_{\overrightarrow{k},\sigma}(t)$ are the operators corresponding to the real canonical variables $q_{\overrightarrow{k},\sigma}(t)$ and $p_{\overrightarrow{k},\sigma}(t)$. For many purposes, it is more convenient to deal, not with the operators $\widehat{p}_{\overrightarrow{k},\sigma}(t)$ and $\widehat{q}_{\overrightarrow{k},\sigma}(t)$, but with a set of operators defined by :

$$\widehat{a}_{\overrightarrow{k},\sigma}(t) = \sqrt{\frac{1}{2\hbar\omega_{\overrightarrow{k}}}} \left(\omega_{\overrightarrow{k}} \widehat{q}_{\overrightarrow{k},\sigma}(t) + i\widehat{p}_{\overrightarrow{k},\sigma}(t) \right), \tag{4.15}$$

$$\widehat{a}^\dagger_{\overrightarrow{k},\sigma}(t) = \sqrt{\frac{1}{2\hbar\omega_{\overrightarrow{k}}}} \left(\omega_{\overrightarrow{k}} \widehat{q}_{\overrightarrow{k},\sigma}(t) - i\widehat{p}_{\overrightarrow{k},\sigma}(t) \right), \tag{4.16}$$

where the second operator is the Hermitian conjugate (†) of the first one. Thanks to the followed commutation relation $\left[\widehat{a}_{\overrightarrow{k},\sigma}(t), \widehat{a}^{\dagger}_{\overrightarrow{k},\sigma}(t)\right] = I\delta_{\overrightarrow{k},\overrightarrow{k}'}\delta_{\sigma,\sigma'}$, the quantum Hamiltonian can be therefore rewritten as [117]:

$$\mathcal{H} = \sum_{\overrightarrow{k},\sigma} \left[\widehat{a}^{\dagger}_{\overrightarrow{k},\sigma}(t)\widehat{a}_{\overrightarrow{k},\sigma}(t) + \frac{1}{2}\right]\hbar\omega_{\overrightarrow{k}}. \tag{4.17}$$

Each mode $(\overrightarrow{k},\sigma)$ of the quantum Hamiltonian is formally equivalent to a harmonic oscillator containing a $n_{\overrightarrow{k},\sigma}$ number of quantum excitations. Similarly, a mode $(\overrightarrow{k},\sigma)$ of the electromagnetic field contains a $n_{\overrightarrow{k},\sigma}$ number of photons. The eigen energy which is associated to the mode $(\overrightarrow{k},\sigma)$ and is an eigen value of the quantum Hamiltonian writes as:

$$\mathcal{E}_{\overrightarrow{k},\sigma} = (n_{\overrightarrow{k},\sigma} + \frac{1}{2})\hbar\omega_{\overrightarrow{k}}. \tag{4.18}$$

An eigen state of the electromagnetic field is an eigen state vector labeled by a list of integer numbers specifying for each mode $(\overrightarrow{k},\sigma)$ the number $n_{\overrightarrow{k},\sigma}$ of photons in this mode. Such an eigen state vector writes as :

$$|\psi\rangle = \left|n_{\overrightarrow{k}_1,\sigma_1}, n_{\overrightarrow{k}_2,\sigma_2}, \ldots, n_{\overrightarrow{k},\sigma}, \ldots\right\rangle. \tag{4.19}$$

4.4 Properties of the $\widehat{a}_{\overrightarrow{k},\sigma}(t)$ and $\widehat{a}^{\dagger}_{\overrightarrow{k},\sigma}(t)$ operators

The action of the operators $\widehat{a}_{\overrightarrow{k},\sigma}(t)$ and $\widehat{a}^{\dagger}_{\overrightarrow{k},\sigma}(t)$ on the eigen state vector of the quantum Hamiltonian reduces to :

$$\widehat{a}_{\overrightarrow{k},\sigma}(t)\left|n_{\overrightarrow{k}_1,\sigma_1}, n_{\overrightarrow{k}_2,\sigma_2}, \ldots, n_{\overrightarrow{k},\sigma}, \ldots\right\rangle = \sqrt{n_{\overrightarrow{k},\sigma}}\left|n_{\overrightarrow{k}_1,\sigma_1}, n_{\overrightarrow{k}_2,\sigma_2}, \ldots, n_{\overrightarrow{k},\sigma} - 1, \ldots\right\rangle, \tag{4.20}$$

$$\widehat{a}^{\dagger}_{\overrightarrow{k},\sigma}(t)\left|n_{\overrightarrow{k}_1,\sigma_1}, n_{\overrightarrow{k}_2,\sigma_2}, \ldots, n_{\overrightarrow{k},\sigma}, \ldots\right\rangle = \sqrt{n_{\overrightarrow{k},\sigma}+1}\left|n_{\overrightarrow{k}_1,\sigma_1}, n_{\overrightarrow{k}_2,\sigma_2}, \ldots, n_{\overrightarrow{k},\sigma} + 1, \ldots\right\rangle. \tag{4.21}$$

which means that $\widehat{a}_{\overrightarrow{k},\sigma}(t)$ "destroys" a photon in the mode $(\overrightarrow{k},\sigma)$ while $\widehat{a}^{\dagger}_{\overrightarrow{k},\sigma}(t)$ "creates" a photon in the mode $(\overrightarrow{k},\sigma)$. For this reason, $\widehat{a}_{\overrightarrow{k},\sigma}(t)$ is called annihilation operator and $\widehat{a}^{\dagger}_{\overrightarrow{k},\sigma}(t)$ is called creation operator. It is noteworthy that the destruction of a photon in the mode $(\overrightarrow{k},\sigma)$ followed by the creation of a photon in the mode $(\overrightarrow{k},\sigma)$ leaves the eigen state vector of the electromagnetic field unchanged :

$$\widehat{a}^{\dagger}_{\overrightarrow{k},\sigma}(t)\widehat{a}_{\overrightarrow{k},\sigma}(t)\left|n_{\overrightarrow{k}_1,\sigma_1}, n_{\overrightarrow{k}_2,\sigma_2}, \ldots, n_{\overrightarrow{k},\sigma}, \ldots\right\rangle = n_{\overrightarrow{k},\sigma}\left|n_{\overrightarrow{k}_1,\sigma_1}, n_{\overrightarrow{k}_2,\sigma_2}, \ldots, n_{\overrightarrow{k},\sigma} - 1, \ldots\right\rangle. \tag{4.22}$$

The operator $N_{\overrightarrow{k},\sigma} = \widehat{a}^{\dagger}_{\overrightarrow{k},\sigma}(t)\widehat{a}_{\overrightarrow{k},\sigma}(t)$ measures the number of photons in the mode $(\overrightarrow{k},\sigma)$.

4.5 The quantum vacuum fluctuations

The Eqs. (4.17) and (4.18) indicate that, in the vacuum where no photons are present, a residual electromagnetic field and its associated residual energy exist. Such residual field and energy are called zero point field and zero point energy, respectively. Such phenomena are the consequence of the fact that a quantum mechanical harmonic oscillator can never come to rest. In order to understand the origin of this fact, let us consider the vacuum state of the electromagnetic field $|0\rangle$, which corresponds to the state of lowest energy. According to (4.20) and (4.21), the expectation values of both $\widehat{a}_{\overrightarrow{k},\sigma}(t)$ and $\widehat{a}^{\dagger}_{\overrightarrow{k},\sigma}(t)$ vanish in the vacuum state since :

$$\widehat{a}_{\overrightarrow{k},\sigma}(t)\,|0\rangle = 0 = \langle 0|\,\widehat{a}^{\dagger}_{\overrightarrow{k},\sigma}(t). \tag{4.23}$$

Moreover, the modal expansion of any field operator $\widehat{F}(\overrightarrow{r},t)$, which may be the electric or magnetic field, writes as :

$$\widehat{F}(\overrightarrow{r},t) = \frac{1}{L^{3/2}}\sum_{\overrightarrow{k},\sigma} l(\omega)\,\overrightarrow{\eta}_{\overrightarrow{k},\sigma}\,\widehat{a}_{\overrightarrow{k},\sigma}\,e^{i(\overrightarrow{k}.\overrightarrow{r}-\omega_{\overrightarrow{k}}t)}, \tag{4.24}$$

where $l(\omega)$ is a slowly varying function of frequency which is different for each operator field. According to (4.23), the mean value of the field operator $\left\langle \widehat{F}(\overrightarrow{r},t)\right\rangle$ in vacuum writes as :

$$\left\langle \widehat{F}(\overrightarrow{r},t)\right\rangle = \langle 0|\,\widehat{F}(\overrightarrow{r},t)\,|0\rangle = 0. \tag{4.25}$$

While the mean value of the operator field is zero, it can be shown that the mean of the square of the field operator is not null and writes as [117] :

$$\left\langle \widehat{F}^2(\overrightarrow{r},t)\right\rangle = \langle 0|\,\widehat{F}^2(\overrightarrow{r},t)\,|0\rangle = \frac{2}{(2\pi)^3}\int |l(\omega)|^2\,d^3k \neq 0. \tag{4.26}$$

Since the variance of the field operator is $\langle 0|\,(\Delta\widehat{F}(\overrightarrow{r},t))^2\,|0\rangle = \langle 0|\,\widehat{F}^2(\overrightarrow{r},t)\,|0\rangle$, where $\Delta\widehat{F}(\overrightarrow{r},t) \equiv \widehat{F}(\overrightarrow{r},t) - \left\langle \widehat{F}(\overrightarrow{r},t)\right\rangle$, is different from zero according to (4.26), the electromagnetic field fluctuates in the vacuum state. An eigen state vector and an eigen energy are therefore attributed to these quantum vacuum fluctuations : the zero point field and the zero point energy, respectively.

Chapter 5

The Lifshitz-van der Waals interactions

In 1948, Hendrik Casimir developed the theory of van der Waals interactions between macroscopic perfectly reflecting metallic mirrors [59]. The interaction can be attributed to a radiation pressure caused by the manifestation of quantum vacuum fluctuations. The Casimir's idea was extended by Evgeny Mikhailovich Lifshitz in 1955 to non ideal mirrors for describing the macroscopic van der Waals interactions between dielectric bodies, *i.e.* Lifshitz-van der Waals interactions [60]. The Casimir interactions and its Lifshitz-van der Waals generalization have been widely studied within the planar bodies geometry from both theoretical and experimental points of view for many years [118, 119, 65, 84, 106]. Moreover, the growing interest in nanoelectromechanical systems urges the scientific community to study in depth van der Waals and electrostatic interactions within nanostructured systems [120, 70]. In particular, looking at nanostructures in the theoretical framework of Lifshitz-van der Waals interactions turns out to be of great interest, both from fundamental perspectives and for quantum-based technologies [121]. In order to understand the influence of surface corrugations on Lifshitz-van der Waals interactions between macroscopic bodies, many approaches emerged few years ago, each one addressing specific corrugation geometries [70]. On one hand, methods, such as the proximity force approximation and the pairwise summation, appear to be the most employed when describing interactions between smooth corrugated surfaces at short and long separation distances, respectively [70, 92]. On the other hand, when considering corrugated surfaces with small correlation lengths (of the order of the separation distance), methods such as scattering or perturbative approaches are required in order to take into account diffraction and correlation effects which occur at the nanoscale [70, 100]. The method described hereafter evaluates the Lifshitz-van der Waals interactions within the scattering approach.

5.1 The individual mode free energy within a cavity system

Let us consider a cavity system that is formed by two macroscopic bodies facing each other in vacuum and separated by a distance L (Fig 5.1). In the case of Lifshitz-van der Waals

interactions, the total free energy G, which can be assimilated to the work of the Lifshitz-van der Waals force, is supposed to depend only on the discrete electromagnetic modes ω_p available inside the cavity and is therefore the sum of each individual mode free energy. In the following, $\omega_p = \omega_p(\overrightarrow{k}_{//})$, where $\overrightarrow{k}_{//}$ is the parallel component (*i.e.* parallel to the planes of the cavity) of the related photon wave vector. In a first step, the all set of the eigen modes of the cavity system, *i.e.* modes outside and inside the cavity, are considered. The free energy $g(\omega_p)$ associated to

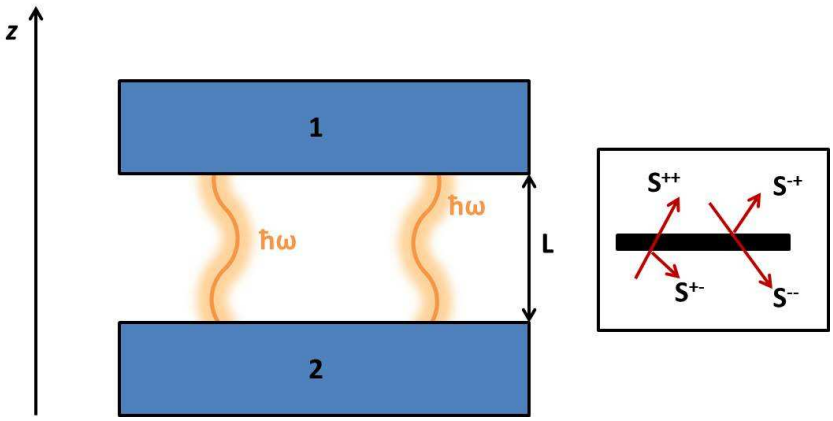

Figure 5.1: Cavity system formed by two macroscopic bodies facing each other in vacuum. Each body can be optically represented by its scattering matrix (S_1 or S_2). The same representation applies for the space between bodies vacuum (S_v). Discrete virtual electromagnetic modes are represented in the cavity.

the p^{th} mode can be expressed as:

$$g(\omega_p) = -k_b T \ln(Z(\omega_p)), \tag{5.1}$$

where k_b is the Boltzmann constant, T is the absolute temperature and $Z(\omega_p)$ is the partition function of the system associated to the p^{th} mode which can be written as :

$$Z(\omega_p) = \sum_{n=0}^{\infty} e^{\frac{-E_p(n)}{k_b T}}, \tag{5.2}$$

where E_p is the energy associated to p^{th} photon mode, for n photons available within the cavity[1]:

$$E_p(n) = \hbar\omega_p(n + \frac{1}{2}). \tag{5.3}$$

Eq. (5.3) indicates two contributions to the Hamiltonian : a main contribution from the real photons of energy $n\hbar\omega_p$ ($n \neq 0$) and a residual contribution (zero point energy) from vacuum fluctuations ($n = 0$). Based on Eq. (5.2) and (5.3) the partition function can be rewritten[2] :

$$Z(\omega_p) = \frac{e^{-\frac{\hbar\omega_p}{2k_b T}}}{1 - e^{-\frac{\hbar\omega_p}{k_b T}}}. \tag{5.4}$$

[1]The number of photons is given by the Planck's law with $n = \frac{1}{e^{\frac{\hbar\omega}{k_b}} - 1}$.

[2]Eq. (5.2) is the sum of a geometrical progression.

Eqs. (5.1) and (5.4) lead to the following expression for the p^{th} mode free energy:

$$g(\omega_p) = \hbar\omega_p \left[\frac{1}{2} + \frac{k_b T}{\hbar\omega_p} \ln(1 - e^{-\frac{\hbar\omega p}{k_b T}}) \right]. \tag{5.5}$$

This last expression contains the above mentioned contributions arising from both thermal and quantum effects. However, for standard temperature conditions and short separation distance, the thermal contribution is negligible compared to the quantum contribution since $\hbar\omega_p >> k_b T$ [3]. The p^{th} mode free energy therefore reduces to:

$$g(\omega_p) = \frac{\hbar\omega_p}{2}. \tag{5.6}$$

5.2 The free energy of a cavity system and the dispersive energy

The free energy of the cavity system $G(\overrightarrow{k_{//}})$, for a given parallel component $\overrightarrow{k_{//}}$ of the photon wave vector, is the sum of the p individual modes free energies:

$$G(\overrightarrow{k_{//}}) = 2\sum_p g(\omega_p) = \sum_p \hbar\omega_p, \tag{5.7}$$

where the factor 2 accounts for the two polarizations states of the quantum vacuum photon modes. The dispersive energy U per unit area, *i.e.* the interaction solely due to vacuum fluctuations, of the cavity system is obtained by integrating the free energy $G(\overrightarrow{k_{//}})$ over the parallel wave vectors:

$$U = \int \frac{d^2 \overrightarrow{k}_{//}}{(2\pi)^2} G(\overrightarrow{k_{//}}). \tag{5.8}$$

It is noteworthy that, rigorously, the energy U is the dispersive **free** energy. However, as temperature effects can be neglected in the present case, this energy can be assimilated to a potential dispersive energy.

5.3 The dispersive energy and the density of states

The individual free energies summation required above can be actually carried out *via* the argument principle theorem: for a meromorphic function[4] $f(z)$ and a holomorphic function[5] $g(z)$ in a γ loop containing the poles of $f(z)$ (Fig. 5.2), the following expression is verified [123]:

[3] In such conditions, $k_b T \approx 0.025\ eV$ ($T = 300K$), which is an order of magnitude lower than the lowest photon energy involved here, $\hbar\omega_p = 0.619\ eV$ ($\lambda_p = 2\mu m$). Therefore, $\frac{k_b T}{\hbar\omega_p} \ln(1 - e^{-\frac{\hbar\omega p}{k_b T}}) \approx -6.86 \times 10^{-13}$ which is negligible compared to the quantum vacuum contribution. Although not considered in the present study, it is noteworthy that in the case of metallic mirrors and for large separation distances ($L > 1\mu m$) the thermal contribution to the energy E_p needs to be taken into account [122].

[4] A meromorphic function is a holomorphic function on a close loop of the complex plane, except for a set of isolated points (the poles of the function) contained in the close loop.

[5] A holomorphic function is a function that is differentiable in a neighborhood around every points of a close loop in the complex plane.

$$\sum_p g(z_p) = -\frac{1}{2\pi i}\oint_\gamma g(z)\frac{d}{dz}\ln(f(z))dz, \tag{5.9}$$

where z_p are the poles of $f(z)$ and where it is assumed that $f(z)$ does not possess any zeros.

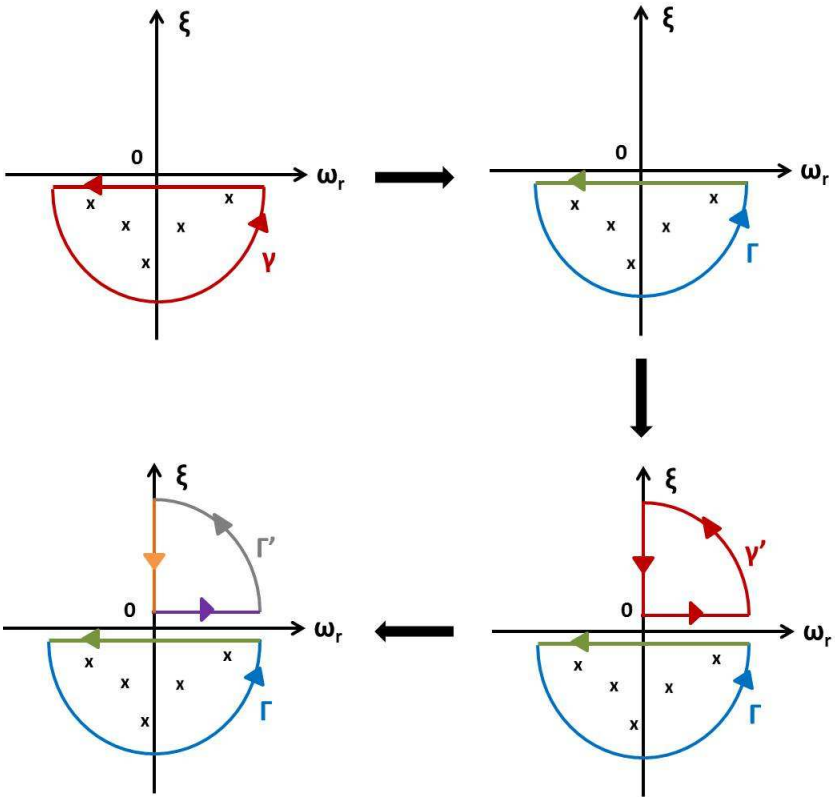

Figure 5.2: Sketch of close loops γ and $\gamma^{'}$ and their respective decomposition in open loop (Γ and $\Gamma^{'}$) and finite interval along the real frequency axis (for γ) and the imaginary frequency axis (for $\gamma^{'}$). See text below for explanations.

In the case of the above described cavity, the angular frequencies ω_p related to each eigen mode can be obtained from the scattering matrix S of the system [116] and are given by solving[6]:

$$\det S^{-1}(\omega_p, \overrightarrow{k}_{//}) = 0, \tag{5.10}$$

i.e. the eigen modes are the poles of $\det S(\omega, \overrightarrow{k}_{//})$ with $\omega = \omega_r - i\xi$, the complex angular frequency. Moreover, $\det S(\omega, \overrightarrow{k}_{//})$ does not possess any zeros [7] and, as $\det S(\omega)$ is meromorphic [123], it contains the eigen modes of the system. Furthermore, the individual mode free energy $g(\omega)$ is a holomorphic function [123]. Therefore, by virtue of the argument principle (Eq. (5.9)), the free energy $G(\overrightarrow{k}_{//})$ of the cavity system is:

$$G(\overrightarrow{k_{//}}) = \sum_p g(\omega_p) = -\frac{1}{2\pi i}\oint_\gamma g(\omega)\frac{d}{d\omega}\ln(\det S(\omega, \overrightarrow{k}_{//}))d\omega. \tag{5.11}$$

[6] See Chapter 2

[7] The scattering matrix does not possess any global zeros, see Chapter 2.

Considering the decomposition of the close loop γ into an open loop Γ and a finite interval along the real frequency axis (Fig. 5.2), Eq. (5.11) can be expressed as:

$$\begin{aligned} G(\overrightarrow{k_{//}}) &= -[\frac{1}{2i\pi}\oint_{\gamma} g(\omega)\frac{d}{d\omega}\ln(\det S(\omega, \overrightarrow{k}_{//}))\ d\omega], \\ &= -[\frac{1}{2i\pi}\int_{\Gamma} g(\omega)\frac{d}{d\omega}\ln(\det S(\omega, \overrightarrow{k}_{//}))\ d\omega - \frac{1}{2i\pi}\int_{-\infty}^{\infty} g(\omega_r)\frac{d}{d\omega_r}\ln(\det S(\omega_r, \overrightarrow{k}_{//}))\ d\omega_r], \\ &= \frac{1}{2i\pi}\int_{-\infty}^{\infty} g(\omega_r)\frac{d}{d\omega_r}\ln(\det S(\omega_r, \overrightarrow{k}_{//}))\ d\omega_r. \end{aligned} \tag{5.12}$$

The integration on the open loop Γ is equal to zero because $\lim_{|\omega|\to\infty}\ln(\det S(\omega, \overrightarrow{k}_{//})) = 0$[8]. It is noteworthy that the electromagnetic density of states $\rho(\omega_r(\overrightarrow{k}_{//}))$ is implicitly expressed in Eq. (5.12). Indeed, let us consider $\rho(\omega_r, \overrightarrow{k}_{//})$ a Dirac comb [124] for modes without losses:

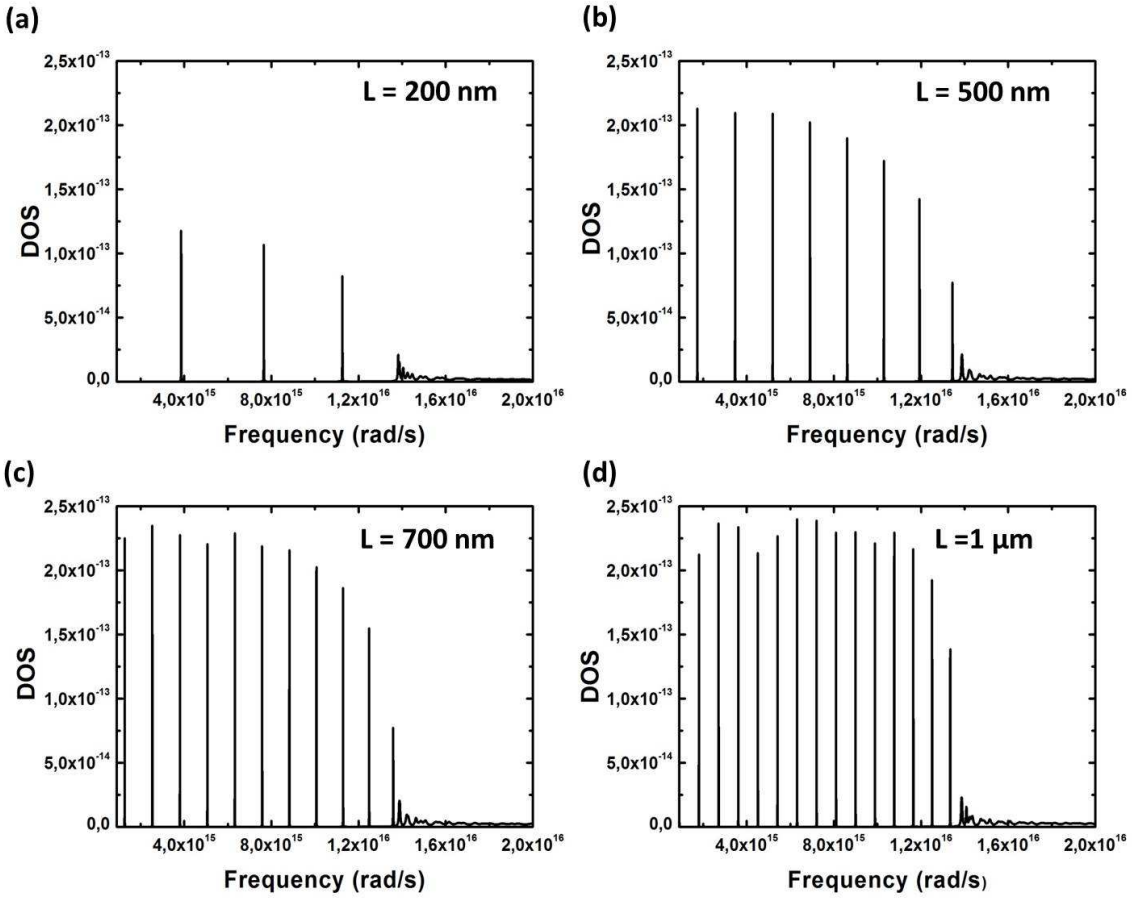

Figure 5.3: Density of states (DOS) $\rho(\omega_r, \overrightarrow{k}_{//} = \overrightarrow{0})$ of a cavity system formed by two copper mirrors facing each other with a separation distance equal to : (a) 200 nm, (b) 500 nm, (c) 700 nm and (d) 1 μm. The x-axis is the real frequency ω_r.

[8]When $\omega \longrightarrow \infty$, $\varepsilon(\omega) \longrightarrow 1$ and the system is assimilated to vacuum. Therefore, $S(\omega, \overrightarrow{k}_{//}) = I$, $\det(S(\omega, \overrightarrow{k}_{//})) = 1$ and $\ln(\det(S(\omega, \overrightarrow{k}_{//}))) = 0$.

$$\rho(\omega_r, \overrightarrow{k}_{//}) = \sum_p \delta(\omega_r - \omega_{r,p}). \tag{5.13}$$

Moreover, since :

$$\sum_p g(\omega_{r,p}) = \sum_p \int_{-\infty}^{+\infty} g(\omega_r)\delta(\omega_r - \omega_{r,p})d\omega, \tag{5.14}$$

then :

$$G(\overrightarrow{k_{//}}) = \int_{-\infty}^{+\infty} g(\omega_r)\rho(\omega_r, \overrightarrow{k}_{//})d\omega_r, \tag{5.15}$$

Therefore, according to Eq. (5.12) and (5.15), the electromagnetic density of states writes as:

$$\rho(\omega_r, \overrightarrow{k}_{//}) = \frac{1}{2\pi i}\frac{d}{d\omega_r}\ln(\det S(\omega_r, \overrightarrow{k}_{//})). \tag{5.16}$$

Fig. 5.3 displays the density of states $\rho(\omega_r, \overrightarrow{k}_{//})$ of two copper mirrors for different separation distances L = 200 nm , 500 nm, 700 nm , 1 μm. The density of states is here illustrated for normal incidence, *i.e.* $\overrightarrow{k_{//}} = \overrightarrow{0}$, and copper was modelized by a Drude model ($\omega_{plasma} = 1.36 \times 10^{16} rad/s$, $\gamma_{loss} = 4.4 \times 10^{13} rad/s$). Sharp peaks on Fig. 5.3 indicate the eigen modes of the system which are equally spaced. Indeed, due to the boundary conditions of the cavity, the p^{th} mode frequency writes as $\omega_p = p\pi c/L$ and so the mode spacing $\Delta\omega_p = \pi c/L$ is constant. The greater the mirror separation distance, the greater the number of modes. Beyond their plasma frequency, the mirrors become transparent preventing the existence of eigen modes within the cavity system, as displayed on Fig. 5.3.

While the electromagnetic density of states can be easily evaluated for each photon wave vectors $\overrightarrow{k}_{//}$, its numerical integration over frequencies turns to be extremely difficult. Indeed, the Dirac-like peaks distribution imposes a very small integration step, leading to huge computational time. Therefore, in order to avoid such numerical issues, the use of imaginary eigen modes angular frequency, *via* a Wick rotation, is required as explained hereafter.

5.4 The free energy of a cavity system within the imaginary frequency domain

The complex form of the eigen mode angular frequency ω_p is:

$$\omega_p = \omega_{r,p} - i\xi_p, \tag{5.17}$$

where $\omega_{r,p}$ is the real part of the p^{th} complex eigen mode angular frequency and ξ_p is the corresponding imaginary part, with $\omega_{r,p} \in \mathbb{R}$ and $\xi_p \in \mathbb{R}^+$. Note that, since the electromagnetic fields are proportional to $e^{-i\omega_p t} = e^{-i\omega_{r,p}t}e^{-\xi,pt}$, the limited lifetime of the mode imposes $\xi_p \in \mathbb{R}^+$. Therefore, the eigen modes of the system, *i.e.* the poles of $\det S(\omega, \overrightarrow{k}_{//})$, are located in the lower half complex plane defined by the above described close loop γ as its radius tends to infinity (Fig. 5.2). Moreover, after substitution by $g(\omega) = \frac{\hbar\omega}{2}$, integrating by parts Eq. (5.11)

leads to:

$$\begin{aligned} G(\overrightarrow{k_{//}}) &= -\frac{\hbar}{4i\pi}\oint_\gamma \omega\frac{d}{d\omega}\ln(\det S(\omega,\overrightarrow{k}_{//}))\ d\omega, \\ &= -\frac{\hbar}{4i\pi}\left[\omega\ln(\det S(\omega,\overrightarrow{k}_{//}))\right]_\gamma + \frac{\hbar}{4i\pi}\oint_\gamma \ln(\det S(\omega,\overrightarrow{k}_{//}))\ d\omega, \\ &= \frac{\hbar}{4i\pi}\oint_\gamma \ln(\det S(\omega,\overrightarrow{k}_{//}))\ d\omega. \end{aligned} \tag{5.18}$$

The term $\left[\omega\ln(\det S(\omega,\overrightarrow{k}_{//}))\right]_\gamma$ vanishes due to the simple-valued[9] character of $\omega\ln(\det S(\omega,\overrightarrow{k}_{//}))$. Considering the decomposition of the close loop γ into an open loop Γ and a finite interval along the real axis (Fig. 5.2) , Eq. (5.18) can be expressed as:

$$\begin{aligned} G(\overrightarrow{k_{//}}) &= \frac{\hbar}{4i\pi}\oint_\gamma \ln(\det S(\omega,\overrightarrow{k}_{//}))\ d\omega, \\ &= \frac{\hbar}{4i\pi}\int_\Gamma \ln(\det S(\omega,\overrightarrow{k}_{//}))\ d\omega - \frac{\hbar}{4i\pi}\int_{-\infty}^{\infty}\ln(\det S(\omega_r,\overrightarrow{k}_{//}))\ d\omega_r, \\ &= -\frac{\hbar}{4i\pi}\int_{-\infty}^{\infty}\ln(\det S(\omega_r,\overrightarrow{k}_{//}))\ d\omega_r. \end{aligned} \tag{5.19}$$

The integration on the open loop Γ is equal to zero because $\lim_{|\omega|\to\infty}\ln(\det S(\omega,\overrightarrow{k}_{//})) = 0$. Moreover, since $S(-\omega_r,\overrightarrow{k}_{//}) = S(\omega_r,\overrightarrow{k}_{//})^*$[10] which imposes $\det S(-\omega_r,\overrightarrow{k}_{//}) = (\det S(\omega_r,\overrightarrow{k}_{//}))^*$, one then obtains :

$$\begin{aligned} G(\overrightarrow{k_{//}}) &= -\frac{\hbar}{4i\pi}\int_{-\infty}^{\infty}\ln(\det S(\omega_r,\overrightarrow{k}_{//}))\ d\omega_r, \\ &= -\frac{\hbar}{4i\pi}\int_0^{\infty}\left(\ln(\det S(\omega_r,\overrightarrow{k}_{//}))\right)^*\ d\omega_r - \frac{\hbar}{4i\pi}\int_0^{\infty}\ln(\det S(\omega_r,\overrightarrow{k}_{//}))\ d\omega_r, \\ &= -\frac{\hbar}{2i\pi}\int_0^{\infty} Re\left\{\ln(\det S(\omega_r,\overrightarrow{k}_{//}))\right\}\ d\omega_r. \end{aligned} \tag{5.20}$$

Considering now a meromorphic function $F(z)$ and close loop γ' of the upper part of the complex plane which does not contain any poles of $F(z)$ (Fig. 5.2). Such conditions impose the integration of the function $F(z)$ along this loop to be zero and therefore writes as (Fig. 5.2):

$$\int_{\gamma'} F(z)dz = \int_0^{\infty} F(\omega_r)d\omega + \int_{\Gamma'} F(z)dz - i\int_0^{\infty} F(i\xi)d\xi = 0. \tag{5.21}$$

Since $\lim_{|z|\to\infty} F(z) = 0$, Eq. (5.21) leads to:

$$i\int_0^{\infty} F(i\xi)d\xi = \int_0^{\infty} F(\omega_r)d\omega_r. \tag{5.22}$$

[9] A simple-valued function is a function that is not defined to within $2\pi i$.
[10] See Chapter 2

Such a procedure where the integration along the real axis is replaced by one along the imaginary axis is known as a Wick rotation [101, 125]. Since the scattering matrix $S(t)$ is real valued[11], Eq. (5.18) giving the total free energy of the system can be written , according to Eq. (5.20), as:

$$G(\overrightarrow{k_{//}}) = -\frac{\hbar}{2\pi}\int_0^\infty \ln(\det S(i\xi, \overrightarrow{k}_{//}))d\xi. \tag{5.23}$$

The Wick rotation leading to the use of imaginary angular frequencies allows a much more easier numerical integration of the free energy because the function $h(\xi) = \ln(\det S(i\xi, \overrightarrow{k}_{//}))$ is smooth, *i.e.* does not present tight spaced sharp peaks. Such trend is represented on Fig. 5.4, where $h(\xi)$ was calculated for the same case as Fig. 5.3 with a separation distance of 200 nm. Due to its smoothness, the free energy is easily integrated since the issues regarding the

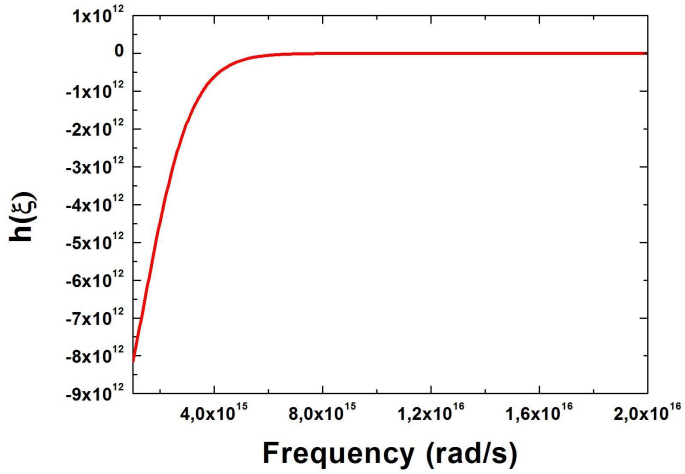

Figure 5.4: Function $h(\xi) = \ln(\det S(i\xi))$ calculated at the normal incidence ($\overrightarrow{k_{//}} = \overrightarrow{0}$) for a cavity system formed of two copper mirrors facing each other in vacuum with a separation distance equal to 200 nm. The x-axis is the imaginary frequency $i\xi$. Its smoothness makes it easily integrable.

integrating steps of the numerical integration over the real frequencies are avoided.

5.5 The Lifshitz-van der Waals interactions

According to (5.8) and (5.23) , the expression for the dispersive energy is :

$$U(L) = -\frac{\hbar}{2\pi}\int \frac{d^2\overrightarrow{k}_{//}}{(2\pi)^2}\int_0^\infty d\xi \ln(\det S(i\xi, \overrightarrow{k}_{//})). \tag{5.24}$$

Here, we have noted explicitly the dependance of U on the cavity length L. At this point, the all set of eigen modes of the cavity system, *i.e.* modes inside and outside the cavity, are considered. However, the Lifshitz-van der Waals energy is attributed solely to the eigen modes inside the

[11] See Chapter 3.

cavity. Optically speaking, the system can be faithfully described by three scattering matrices : S_1 related to the body 1, S_2 related to the body 2 and S_v related to the intervening medium (vacuum in the present case [12]) (Fig. 5.2). The scattering matrix S of the global system is the combination of those three matrices, the elements of which are given by the combination rules described in Sect. 2.7:

$$S^{++} = S_2^{++} S_v^{++} K S_1^{++}, \tag{5.25}$$

$$S^{+-} = S_2^{+-} + S_2^{++} S_v^{++} K S_1^{+-} S_v^{--} S_2^{--}, \tag{5.26}$$

$$S^{-+} = S_1^{-+} + S_1^{--} S_v^{--} S_2^{-+} S_v^{++} K S_1^{++}, \tag{5.27}$$

$$S^{--} = S_1^{--} \left(1 + S_v^{--} S_2^{-+} S_v^{++} K S_1^{+-}\right) S_v^{--} S_2^{--}, \tag{5.28}$$

with :

$$K = \frac{1}{1 - S_1^{+-} S_v^{--} S_2^{-+} S_v^{++}}. \tag{5.29}$$

The determinant of the scattering matrix S can be rewritten as [123]:

$$\det S = \det\left(S^{++} - S^{+-}\left[S^{--}\right]^{-1} S^{-+}\right) \det\left(S^{--}\right). \tag{5.30}$$

According to Eq. (5.25) to (5.30), the poles of $\det S$ include the poles of $\det K$. Since the matrix K combines the coupling elements between the two interacting bodies, *i.e.* S_1^{+-} and S_2^{-+}, the poles of $\det K$ correspond to the eigen modes inside the cavity, *i.e.* the allowed quantum vacuum photon modes responsible for the interactions between the two bodies. Note that, the poles of the individual scattering matrices S_1 and S_2, which are the remaining poles of the scattering matrix S (according to Eq. (5.25) to (5.30)), give the eigen modes related to the individual bodies, *i.e.* when bodies 1 and 2 are infinitely separated. As a result, in the following, only the poles of K will be considered, among all the poles of S, *i.e.* $\det S$ is replaced by $\det K$ in Eq. (5.24). Such a maneuver allows avoiding the well-known procedure of subtraction of the photon modes energy at an infinite distance $L \to \infty$ from the Lifshitz-van der Waals energy at a finite distance L[13] which requires complicated regularization operations [70]. Alternatively, the Lifshitz-van der Waals energy per unit area $U^{LW}(L)$ can be written as:

$$U^{LW}(L) = \frac{\hbar}{2\pi} \int \frac{d^2 k_{//}}{(2\pi)^2} \int_0^\infty d\xi \ln[\det(1 - S_1^{+-}(i\xi, \overrightarrow{k}_{//}) S_v^{--}(i\xi, \overrightarrow{k}_{//}) S_2^{-+}(i\xi, \overrightarrow{k}_{//}) S_v^{++}(i\xi, \overrightarrow{k}_{//}))]. \tag{5.31}$$

The computation of the scattering matrices can be done with the RCWA method which imposes boundaries of the cavity system (taking the form of surface corrugation here) to be periodically structured. The periodicity of the boundary layers allows to restrict the integration over $\overrightarrow{k_{//}}$ (*i.e.*

[12] According to the definition of the scattering matrix, S_v is a diagonal matrix *i.e.* only with S_v^{++} and S_v^{--} as non-zero elements. In the case of an intervening medium different from vacuum, S_v is not diagonal anymore leading to more complicated calculations.

[13] $U(L) = \sum_p \frac{1}{2}\hbar(\omega_p(L) - \omega_p(L \to \infty))$

over $\mathbb{R}^2$) to the first Brillouin zone (BZ) [124] such as $\int \frac{d^2k_{//}}{(2\pi)^2} \rightarrow \int_{BZ} \frac{d^2k_{//}}{(2\pi)^2}$. The details of the numerical integration method over the Brillouin zone are presented in Appendix A.The numerical calculation of the energy will therefore require to study the convergence of the result in terms of the range and number of imaginary frequencies ξ, the number of photon wave vectors $N_{\overrightarrow{k}_{//}}$ and the number of reciprocal lattice vectors $N_{\overrightarrow{g}}$.

5.6 The Lifshitz-van der Waals interactions within the flat bodies geometry

In the case of a flat bodies system[14] in vacuum for which obviously no diffraction effects occur, the scattering matrices S_1 and S_2 write as :

$$S_1 = \begin{pmatrix} T_1^{s,++} & 0 & R_1^{s,+-} & 0 \\ 0 & T_1^{p,++} & 0 & R_1^{p,+-} \\ R_1^{s,-+} & 0 & T_1^{s,--} & 0 \\ 0 & R_1^{p,-+} & 0 & T_1^{p,--} \end{pmatrix}, \tag{5.32}$$

$$S_2 = \begin{pmatrix} T_2^{s,++} & 0 & R_2^{s,+-} & 0 \\ 0 & T_2^{p,++} & 0 & R_2^{p,+-} \\ R_2^{s,-+} & 0 & T_2^{s,--} & 0 \\ 0 & R_2^{p,-+} & 0 & T_2^{p,--} \end{pmatrix}, \tag{5.33}$$

where $R_i^{m,h}$ and $T_i^{m,h}$ correspond to the complex reflection and transmission coefficient in the direction h (see Chapter 3) of the body i in the m polarization state (s or p). The scattering matrix of the vacuum spacer S_v writes as:

$$S_v = \begin{pmatrix} e^{ik_zL} & 0 & 0 & 0 \\ 0 & e^{ik_zL} & 0 & 0 \\ 0 & 0 & e^{ik_zL} & 0 \\ 0 & 0 & 0 & e^{ik_zL} \end{pmatrix}, \tag{5.34}$$

where L is the cavity length. According to Eqs. (5.32), (5.33) and (5.34), Eq. (5.31) can be expressed in terms of reflection coefficients:

$$U^{LW}(L) = \frac{\hbar}{2\pi} \sum_{m=s,p} \int \frac{d^2k_{//}}{(2\pi)^2} \int_0^\infty d\xi \ln(1 - R_1^{m-+}(i\xi, k_{//}) R_2^{m+-}(i\xi, k_{//}) e^{-2\kappa L}), \tag{5.35}$$

with $\kappa = \sqrt{\frac{\xi^2}{c^2} + |k_{//}|^2}$. In this specific case of flat bodies system, the numerical calculation of the energy will require to study the convergence of the results in terms of the range and number of imaginary frequencies ξ and the number of photon wave vectors $N_{\overrightarrow{k}_{//}}$ but not in

[14] The flat body can be either a single bulky layer or a flat slab with a multilayer interfacial layer.

terms of number of reciprocal lattice vectors $N_{\overrightarrow{g}}$ since only the specular order $\overrightarrow{g}=0$ has to be considered obviously.

5.7 The Lifshitz-van der Waals interactions: the particular case of perfect reflecting mirrors

The interaction of two semi-infinite perfect reflecting mirrors in vacuum is the case studied by Casimir in 1948 [59]. From Eq. (5.35), let us set $d^2k_{//}=dk_xdk_y=k_{//}dk_{//}d\theta$ ($\theta, k_{//}$: polar coordinates) which leads to :

$$U^{LW}(L)=\frac{\hbar}{2\pi}\sum_{m=s,p}\int_0^\infty\frac{k_{//}dk_{//}}{2\pi}\int_0^\infty d\xi\ln(1-R_1^m(i\xi,\overrightarrow{k}_{//})R_2^m(i\xi,\overrightarrow{k}_{//})e^{-2\sqrt{\frac{\xi^2}{c^2}+|k_{//}|^2}L}). \tag{5.36}$$

Moreover, let us set $k_{//}L=\beta$ and $\frac{\xi}{c}L=\alpha$ and rewrite Eq. (5.36) as :

$$U^{LW}(L)=\frac{\hbar c}{4\pi^2}\frac{1}{L^3}\sum_{m=s,p}\int_0^\infty\beta d\beta\int_0^\infty d\alpha\ln(1-R_1^m(\alpha,\beta)R_2^m(\alpha,\beta)e^{-2\sqrt{\alpha^2+\beta^2}}). \tag{5.37}$$

Since perfect reflecting mirrors are considered, *i.e.* $R_i^s=1$ and $R_i^p=-1$, Eq. (5.37) is reduced to :

$$U^{LW}(L)=\frac{\hbar c}{2\pi^2}\frac{1}{L^3}I, \tag{5.38}$$

with $I=\int_0^\infty\beta d\beta\int_0^\infty d\alpha\ln(1-e^{-2\sqrt{\alpha^2+\beta^2}})$. Using a polar coordinate system, the integral I writes as:

$$\begin{aligned} I &= \int_0^{\frac{\pi}{2}}\sin(\varphi)d\varphi\int_0^\infty\rho^2\ln(1-e^{-2\rho})d\rho,\\ &= \int_0^\infty\rho^2\ln(1-e^{-2\rho})d\rho,\\ &= -\frac{2}{3}\int_0^\infty\rho^3\frac{d\rho}{e^{2\rho}-1}, \end{aligned} \tag{5.39}$$

where Eq. (5.39) is obtained by integration by parts. Imposing $2\rho=x$, Eq. (5.39) rewrites as:

$$I=-\frac{1}{24}\int_0^\infty\frac{x^3}{e^x-1}dx. \tag{5.40}$$

The integral in Eq. (5.40) turns out to be a Bernouilli number, *i.e.* $\int_0^\infty\frac{x^3}{e^x-1}dx=\frac{\pi^4}{15}$, which implies that $I=-\frac{\pi^4}{360}$. Therefore, the Lifshitz-van der Waals energy per unit area for two semi infinite perfect reflecting mirrors writes as :

$$U^{LW}(L)=-\frac{\hbar c\pi^2}{720L^3}, \tag{5.41}$$

which is the well-known expression for the Casimir energy. Due to the perfect reflectivity character of the mirror, this last expression is universal and valid at any separation distance.

5.8 Illustration of the method

As illustration, the absolute Lifshitz-van der Waals interaction energy[15] was calculated using Eq. (5.35) for two semi-infinite flat copper slabs of 1μm thickness both facing each other in vacuum (Fig. 5.5). The complex reflection coefficient of each slab was calculated by the RCWA method in which only the specular order $\overrightarrow{g} = 0$ was considered. Each copper slabs were modeled with a Drude model [100]:

$$\varepsilon(\omega) = 1 - \frac{\omega_{plasma}^2}{\omega(\omega + i\gamma)} \tag{5.42}$$

where $\omega_{plasma} = 8.97eV$ is the plasma frequency of copper and $\gamma = 29.5\ meV$ the relaxation parameter of copper. Note that, rigorously, experimental optical data should be used in the present case in order to take into account interband transitions. However, it will be assumed that the optical description of the mirrors with a Drude model will be sufficient in a first approximation for describing the general trend of the interaction.

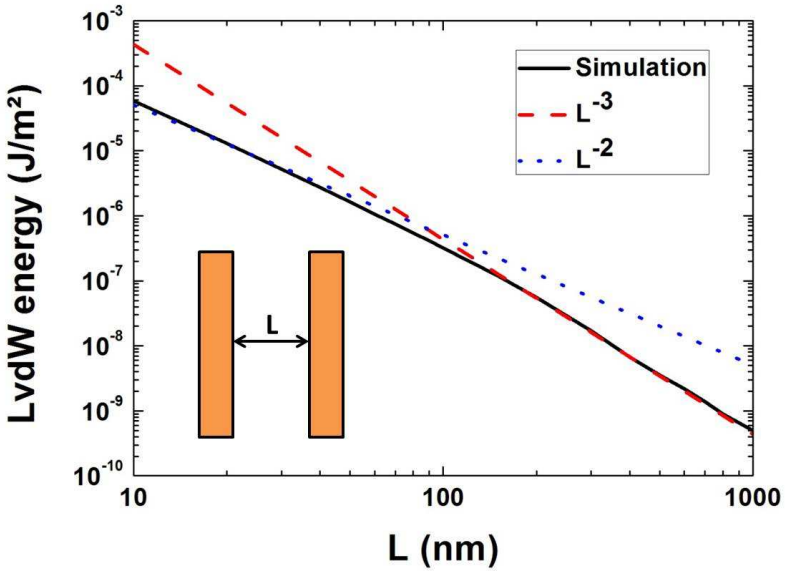

Figure 5.5: Lifshitz-van der Waals interaction energy for two semi-infinite copper slabs facing each other in vacuum.

According to literature [126], the Lifshitz-van der Waals interaction energy per unit area between metallic mirrors decays on one hand as the cube of the separation distance L at long distance range[16] ($L >> \lambda_{plasma}$, with λ_{plasma} the plasma wavelength) as Eq. (5.41) and on the other hand as the square of the separation distance L at short distance range[17] ($L << \lambda_{plasma}$)

[15] The absolute value of the energy (which is attractive and so negative) is taken since a logarithmic representation is employed to display the results (see 5.5).

[16] In this case, the metallic mirrors behave as perfect reflectors, therefore following the Casmir's predictions.

[17] In this case, the interaction between the metallic mirrors is understood in terms of their surface plasmons coupling through evanescent waves [127][65].

as:

$$U^{LW}(L) = -\frac{\alpha\hbar c\pi^2}{480\lambda_{plasma}L^2}, \tag{5.43}$$

where $\alpha = 1.193$ [100]. The results presented in Fig. 5.5 exhibit the expected trend : the Lifshitz-van der Waals energy decays as the square of the separation distance at short range and then gradually turns to decay as the cube of the separation distance.

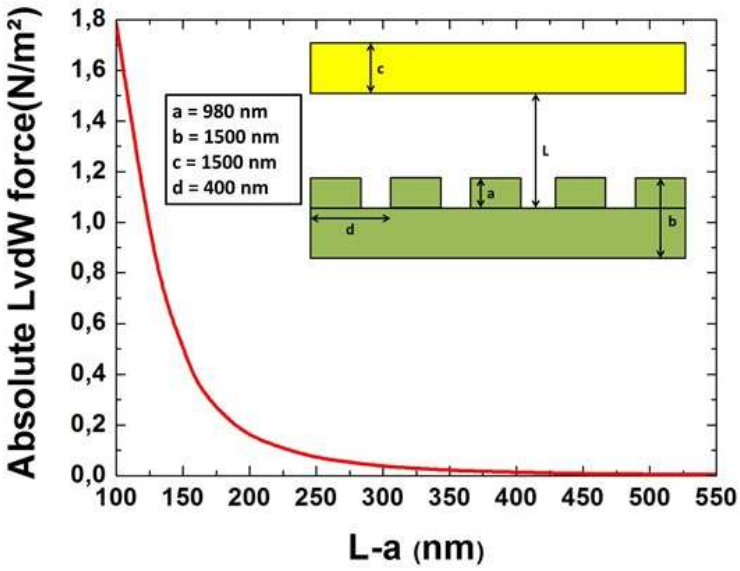

Figure 5.6: Lifshitz-van der Waals interaction force for a silicon grating facing a gold plate in vacuum.

A last check point of the method aimed at establishing the LvdW interaction energy between a silicon grating and a gold plate using Eq. (A.2) and comparing it with published results. The parameters of the grating are displayed on Fig. 5.6 and the parameters of the gold plasma model and the silicon Drude-Lorentz model used in computation were chosen from the literature [92]. The scattering matrices were obtained by the RCWA method with a number $N_{\overrightarrow{g}}$ of reciprocal lattice vectors $\overrightarrow{g} = (g_x, g_y)$, such as: $N_{\overrightarrow{g}} = N_{g_x} \times N_{g_y} = 14 \times 1$. The results of the simulation, presented in Fig. 5.6 in terms of the absolute Lifshitz-van der Waals force (obtained by Lifhitz-van der Waals energy derivative) match well with the published ones [92], validating, as the previous results, the veracity of the method.

Part III

Classical approach of surface multifunctionality at the mesoscopic scale

Chapter 6

The wing of the grey cicada : a natural case of multifunctional surface

Two separated levels of functionality are identified in the nanostructure which covers the wings of the grey cicada *Cicada orni* (Hemiptera). The upper level is responsible for superhydrophobic character of the wing, while the lower level enhances its anti-reflective behavior. Extensive wetting experiments with various chemical species and optical measurements were performed in order to assess the bi-functionality. Scanning electron microscopy imaging was used to identify the nanostructure morphology. Numerical optical simulations and analytical wetting models were used to prove the roles of both levels of the nanostructure. In addition, the complex refractive index of the chitinous material of the wing was determined from measurements.

6.1 Morphology and structural model of the wing membrane

The grey cicada (Fig. 6.1) is one of the most frequent cicada species in the south of France. The studied specimen was captured at Alés in the Cévennes region. The grey cicada is about

Figure 6.1: The grey cicada *Cicada orni* (Hemiptera).

40 mm long and has a 75 mm wing span. In order to investigate the nanostructure of the wing, scanning electron microscopy (SEM) imaging was performed with *Jeol* 7500 *F* scanning electron

microscope. Both sides of the wing are covered by a hexagonal nipple array (Fig. 6.2a). Each

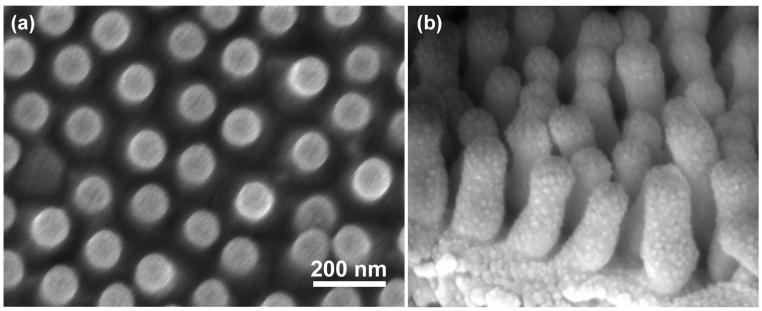

Figure 6.2: Scanning electron microscopy images of the cicada wing. a: Typical hexagonal nipple array is clearly observed. b: Protuberances consist of conic-like tips with a hemispherical top.

protuberance is a truncated cone, with a hemispherical top (Fig. 6.2b). Protuberances lay on a 2.7 μm-thick slab. This type of protuberance is often encountered in compound eyes or corrugated wings of insects [42][128]. According to SEM pictures, the typical dimensions and geometry of the different parts of the structure can be estimated on average. The truncated cone has a circular base of radius $R \approx 85$ nm, and a height $h \approx 160$ nm. The top hemisphere has a radius $r \approx 40$ nm. The total height (cone + hemisphere) is therefore $H \approx 200$ nm. The average hexagonal lattice parameter is $a_0 \approx 173$ nm. It can be fairly assumed that the disorder in the biological structure, *i.e.* weak deviations with respect to perfect lattice, does not significantly affect the main conclusions of the present study [129].

6.2 Optical properties.

6.2.1 Experimental results

The diffusive and polarizing characters of the wing were investigated at incidence angles of 0°, 15° and 30° using scatterometry in transmittance mode (*ELDIM EZcontrast* scatterometer).

The results are presented for an incidence angle of 30°. In order to detect possible polarization of the emerging light, a polarizer was placed as analyzer. In a first step (calibration), at each incidence angle, the bidirectional transmittance distribution function (BTDF) of the incident beam ($\lambda \cong 510$ nm) alone (without wing) was measured, showing purely specular transmittance as expected (Fig. 6.3b). In a second step, the wing was inserted and the polarizer was positioned perpendicular to the wing longitudinal axis and then parallel to it. BTDFs of the wing for both analyzed polarizations were recorded. At each incidence angle, both BTDF maps were compared to the BTDF map of the incident beam alone. Accordingly, neither diffusive effects nor polarizing effects of the wing could be detected (Fig. 6.3c and d). Results (not shown) were identical for the other 32 equidistant wavelengths in the visible spectrum (according to the characteristics of our scatterometer). Since the wing exhibited a very low diffusive character and in order to optimize the signal to noise ratio, transmission properties are mainly emphasized hereafter by contrast with reflection properties.

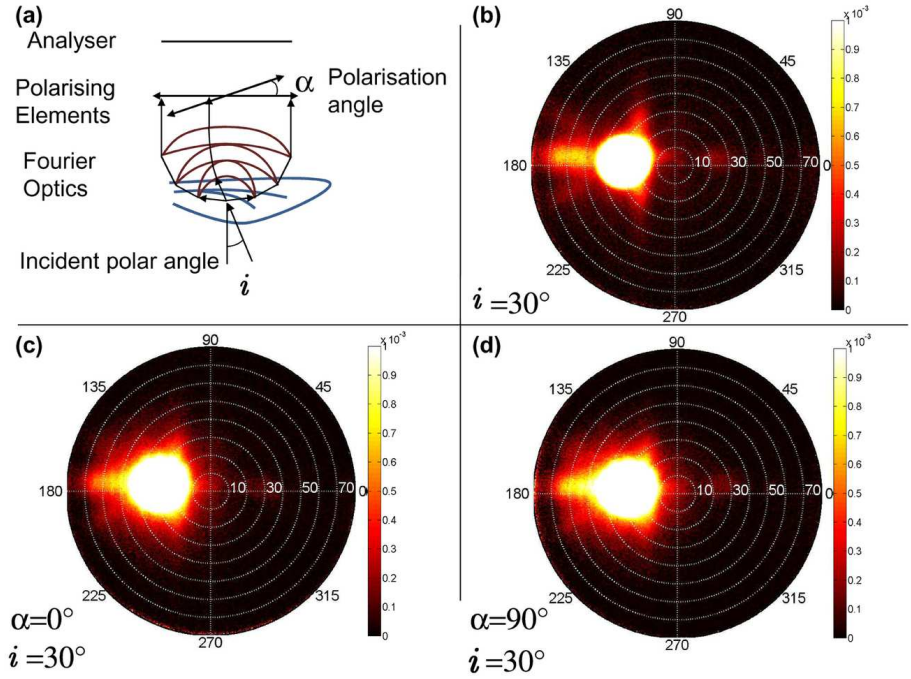

Figure 6.3: Bidirectional Transmittance Distribution Functions (BTDF) (in watt/m^2/sr/nm). Results are shown for polar angles ranging from 0° to 80° and azimuthal angles ranging from 0° to 360°. The wavelength is $\lambda = 509.48$ nm. b: BTDF of the incident beam at an angle of incidence $i = 30°$. c,d: BTDF of the cicada wing at $i = 30°$ and for two orthogonal analyzing polarizer orientations, 0° (panel (c)) and 90° (panel (d)).

Measurements of the wing optical properties were performed at normal incidence using a double beam spectrophotometer (*Perkin Elmer Lambda* 750 *S UV/VIS/NIR*) and an integrating sphere. In Fig. 6.4a, reflection spectrum is shown. Since reflection is very weak, measurement was made with the wing on a black substrate (Certified Reflectance Standard SRS-02-020 *Labsphere* with a reflectance factor of 2% between 250 and 2500 nm). The measured reflection R_m had to corrected since R_m was fairly approximated by $R_m \approx R_w + R_{bg} \cdot T_w^2$ (see insert in Fig. 6.4a) where R_w was the expected wing reflection, R_{bg} was the black substrate reflection (which was measured independently, not shown), and T_w was the free-standing wing transmission which is measured independently (see hereafter). In Fig. 6.4a, the blue dashed curve is R_m whereas the black solid curve is R_w which is deduced from the above expression. This correction confirms that reflection values are weak in accordance with previous results [130], and must be derived carefully. In addition, it is well-known that spectroscopic measurements are impacted by instrumental noise for low transmittance or reflectance levels. As a consequence, it is more relevant to compare high-level transmittance measurements with numerical models, rather than low-level reflectance measurements.

Let us now consider transmission measurements. They were carried out on free-standing wings *i.e* without substrate. The black curve in Fig. 6.4b indicates an almost perfect transmission in the visible range although it appears to be weaker on the blue side than on the red side of the spectrum. This means that almost 100% of the light passes through the free-standing

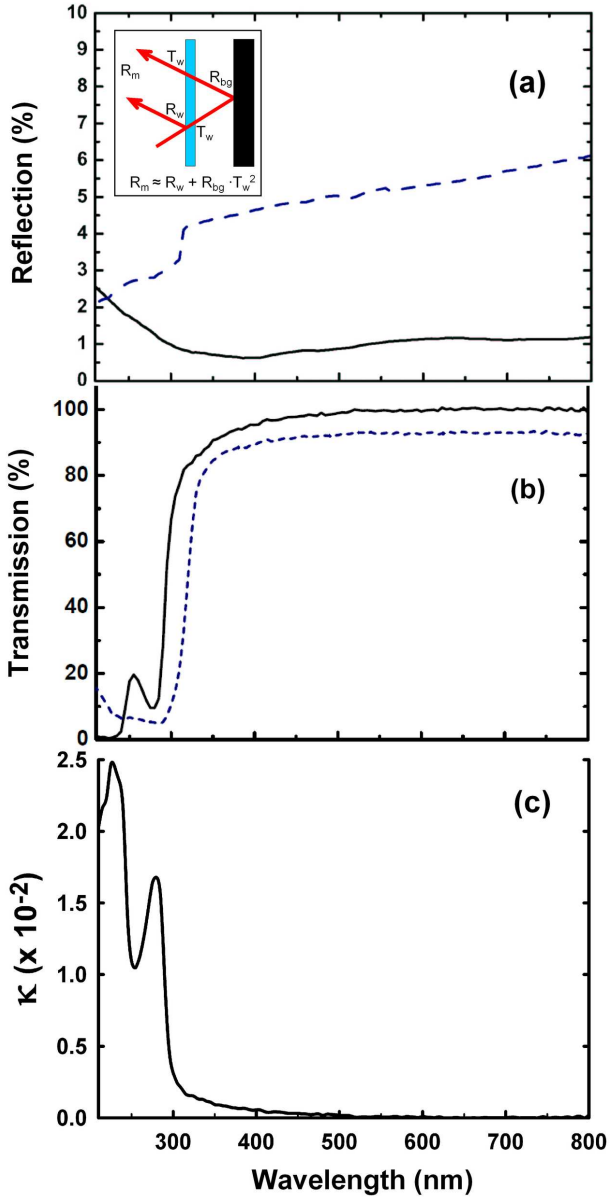

Figure 6.4: a: Measured wing reflection spectrum at normal incidence (blue dashed curve) and corrected measurement (black solid curve). Insert: Correction procedure. b: Measured wing transmission spectrum. Measurements on the actual free-standing wing (black curve) and the wing immersed in index matching oil (blue dashed curve). c: Imaginary part of the optical index of the cicada wing obtained from reflection/transmission measurements.

wing without being absorbed or reflected. The transmission exhibits a large drop below 350 nm, due to a strong intrinsic absorption in the ultra-violet range. Note that in Fig. 6.4a it is found that reflection does not fade away at these wavelengths. Using the absorption coefficient calculated from reflection and transmission at each wavelength, the spectrum of the imaginary part of the complex refractive index was deduced from the Beer-Lambert law [117] as shown in Fig. 6.4c.

In order to reveal the effect of the nipple array on the optical properties, the wing was covered

with a calibrated refractive index oil. Indeed, provided that the oil refractive index matches the refractive index of the protuberances, the oil filling the air cavities and the material can be regarded as a single planar layer. Here, a decrease of transmission was noted using a calibrated commercial oil with a real part of refractive index equal to 1.56. This oil is certified by the manufacturer *Cargille Labs* (also verified by us) with a negligible dispersion on the visible range and a weak dispersion in the ultraviolet domain. Such a refractive index value is consistent with that of chitin [128]. As a result, in the following, it will be assumed that the cicada wing is made of a chitin-like compound with an average refractive index of 1.56. On Fig. 6.4b, the blue curve (transmission spectrum of wing immersed in index matching oil) shows a transmission drop of 6% in the visible range and spectral changes in the UV range. One can then conclude that the nipple array increases the transmission by 6%, improving the transparency of the wing. These results are in agreement with those obtained by other authors [130]. Since UV absorption of the chitin material was determined, the absorption coefficient of the wing (extrapolated from experimental measurement) (Fig. 6.4c) will be used in the following numerical simulations.

6.2.2 Theoretical analysis

On the basis of morphological data, the wing is described as a homogeneous slab with, on both sides, a hexagonal array of truncated cones with top hemispheres (Fig. 6.5a). For the sake of

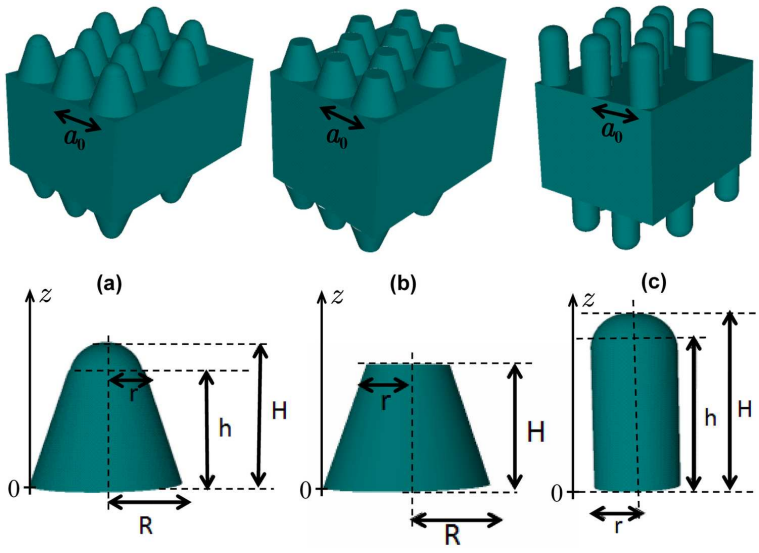

Figure 6.5: Various geometrical models studied. a: Model of the wing structure, b: Model used to study the influence of top hemisphere on transmission, c: Model used to study the influence of truncated cone on transmission.

simplicity, it is assumed that the wing was made of chitin only. The real part of the refractive index is taken equal to 1.56 and is assumed to be constant all over the simulation spectral range whereas the absorption coefficient was taken wavelength-dependent according to data shown in Fig. 6.4c. Simulations of the optical properties were carried out from the near UV to the near infrared (200 to 800 nm) by using a transfer matrix code [129][128].

Since the nipple array has subwavelength dimensions, the corrugated layer can be considered as a continuous effective material with a graded index along its thickness. More specifically, the effective dielectric constant can then be defined by [42]:

$$\varepsilon(z) = \varepsilon_{air} + (\varepsilon_{chitin} - \varepsilon_{air}) f(z), \tag{6.1}$$

where ε_{air} is the dielectric constant of air ($\varepsilon_{air} = 1$), ε_{chitin} is the dielectric constant of chitin and $f(z)$ is filling factor given by:

$$f(z) = \frac{\pi r^2(z)}{S}, \tag{6.2}$$

with $S = \frac{a_0^2\sqrt{3}}{2}$ and $r(z)$ the radius of the circular section of a nipple at coordinate z. While light propagation in corrugated layers is computed thanks to the transfer matrix code, light propagation in the homogeneous thick slab is calculated using an analytical expression based on Fresnel equations in which phases are set to zero in order to mimic optical incoherence. Indeed, structural imperfections in the slab, which is a thick biological layer, tend to break constructive light wave interferences. Finally, although it was chosen to focus on transmission for the reasons exposed previously, simulations of reflection are also performed to corroborate our results.

Simulation results for transmission are shown in Fig. 6.6a. The black curve corresponds to the measured transmission whereas the red curve corresponds to the simulated transmission : The two curves match very well. This result is valid whatever the polarization state is. In order to discriminate the role of the truncated cone and the role of the top hemisphere, two alternative wing models were considered. First, a truncated cone without the hemisphere on top was considered (see Fig. 6.5b). Fig. 6.6b shows the simulated spectrum (red curve) and the measured spectrum (black curve). Both transmission spectra match quite well, showing that the hemisphere does not actually contribute to the transparency of the wing. In a second simulation, a cylinder (instead of a cone) was considered (see Fig. 6.5c) with a hemisphere on top. The result is shown in Fig. 6.6c. The simulated transmission (red curve) is significantly lower than the measured one (black curve). Together with the previous simulation, this result shows that the truncated cone is required to get transparency in the visible range. This can be easily understood since the truncated cone avoids a sudden change in the refractive index when light impinges on the slab. Indeed, considering Eq. (6.1), the truncated cone creates a gradient of refractive index which acts as an optical impedance adaptation layer.

Let us now consider the simulated reflection. Our results are summarized in Fig. 6.7. The measured (black dash-dotted curve) and simulated (red dashed curve) reflections exhibit comparable values about 1%. Nevertheless, spectra of both reflections do not perfectly match. As explained previously, this can be explained by the lack of accuracy when measuring weak reflections. The simulated reflection for the wing model without hemispheres (cyan solid curve) is also presented. As for the transmission (Fig. 6.6b), there is negligible difference (less than 2%) with the full wing model (Fig. 6.5a). Now, by contrast, if the model with cylinders instead

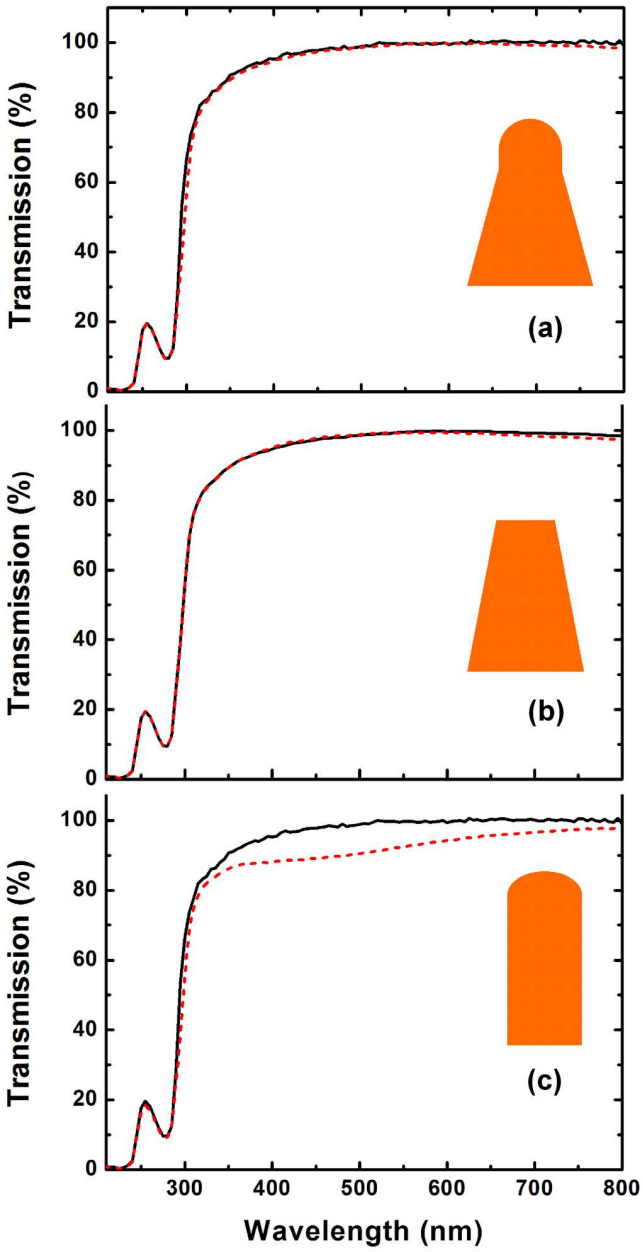

Figure 6.6: a: Measurement (black solid curve) and theoretical simulation (red dashed curve) on the actual wing model. b: Measurement (black solid curve) and theoretical simulation on the wing model without hemispheres on top (red dashed curve). c: Measurement (black solid curve) and theoretical simulation on the wing model with cylinders instead of truncated cones (red dashed curve).

of truncated cones is considered, it is seen that the reflection increases by a level of about 10. This corroborates qualitatively our results obtained with the transmission (Fig. 6.6c). In addition, strong oscillations of the simulated reflection, since the array of cylinders acts as a thin effective homogeneous slab where interferences occur.

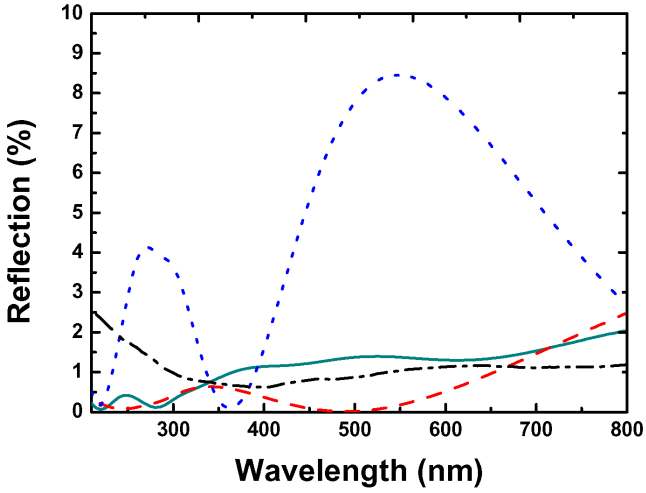

Figure 6.7: Theoretical simulation (red dashed curve) of the reflection on the full wing model (Fig. 6.3a). This curve can be compared with the simulated reflections for the wing model without hemispheres on top (cyan solid curve) or with cylinders instead of truncated cones (blue short-dashed curve). The black dash-dotted curve is the measured reflection, after correction.

6.3 Wetting properties

6.3.1 Experimental results

A surface can be classified as superhydrophobic if the static contact angle of a water droplet on the surface is higher than 150°. If the contact angle lies between 90° and 150°, the surface is only hydrophobic and it is hydrophilic if the contact angle lies between 0° and 90°. In the present case, the contact angle of a water droplet on the wing surface is measured to be 146° ± 3° (Fig. 6.8). As a consequence, the wing of *Cicada orni* is almost superhydrophobic.

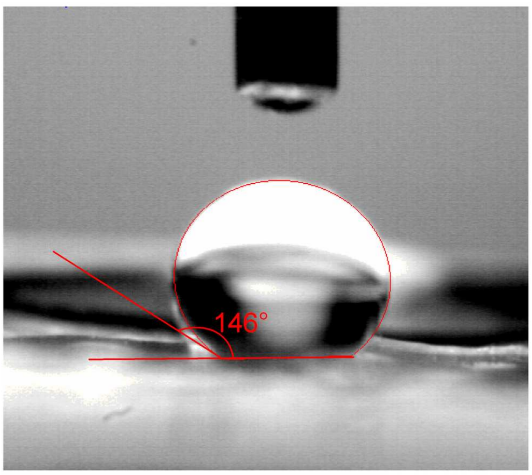

Figure 6.8: Wetting measurement on wing of *Cicada orni*, the contact angle is 146° ± 3°.

According to previous works related to the link between nanostructure and superhydrophobicity [131], it can be fairly inferred that the nipple array covering the wing surface is responsible for its hydrophobic properties. Indeed, without the nanostructure, the water droplet would

probably spread on the surface since the contact angle of water on a flat chitin surface is about 105° [132].

For a better understanding of the wing hydrophobicity, it is relevant to measure the wetting properties for various liquids with different surface tensions. For this purpose, ethanol-water solutions were used with different mass percentages of ethanol (from 0% to 100%), but also a 6.0 M sodium chloride aqueous solution and mercury.

The effective contact angle θ_{eff} for each liquid on the wing (the nanostructured surface) was measured, and then plotted against $\cos\theta$, where θ is the contact angle on a flat chitin surface (Fig. 6.9 ; black dots correspond to measured values). Since the liquid-gas surface tension γ_{LG}

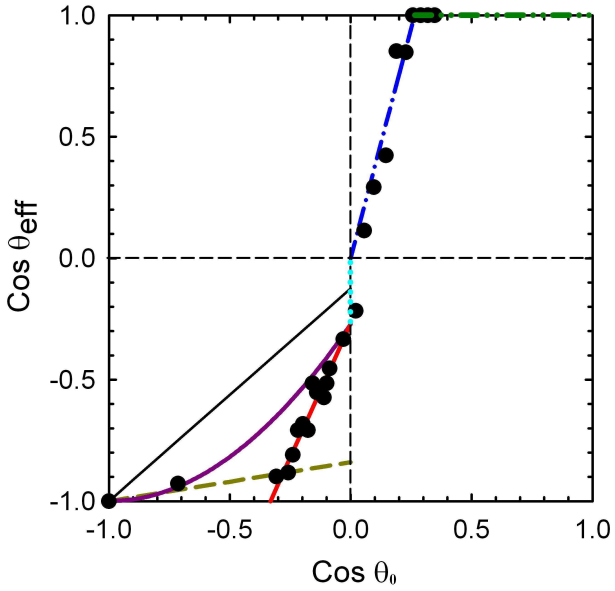

Figure 6.9: Effective contact angle θ_{eff} (nanostructured surface) as a function of the contact angle θ on a flat surface. The black dots are the experimental results. The blue (dash-dotted) straight line is plotted from Eq. (6.10), the purple (solid) curve is from Eq. (6.8). Brown (dashed) and red (solid) straight lines show trends by contrast to the ideal model. Light blue (dotted) vertical straight line corresponds to the hydrophobic/wetting transition. The green (dash-dot-dotted) straight line corresponds to the process of hemiwicking. The solid black line corresponds to the plot of Eq. (6.9).

of the used liquids are known [18][133], and since the solid-gas surface tension γ_{SG} of chitinous material can be calculated (see below), it is possible to calculate the contact angle θ for a given liquid on a flat chitinous surface, using the Young equation [1]:

$$\gamma_{SG} = \gamma_{SL} + \gamma_{LG}\cos\theta. \tag{6.3}$$

The solid/liquid surface tension γ_{SL} can be approximated by [18]:

$$\gamma_{SL} = \gamma_{SG} + \gamma_{LG} - 2\sqrt{\gamma_{SG}^{LW}\gamma_{LG}^{LW}} - 2\sqrt{\gamma_{SG}^{AB}\gamma_{LG}^{AB}}, \tag{6.4}$$

where the superscripts LW and AB denote the Lifshitz-van der Waals energy contribution

and the Acid-Base energy contribution to the surface tension[1], respectively, such that $\gamma_i = \gamma_i^{LW} + \gamma_i^{AB}$. While the total surface tension γ_{LG} can be easily obtained for the water-ethanol mixture mentioned above, the relative parts of the Lifshitz-van der Waals contribution γ_{LG}^{LW} and the Acid-Base contribution γ_{LG}^{AB} are more difficult to evaluate and so γ_{SL} *via* Eq. (6.4). However, in order to start investigating phenomenologically the wetting properties of the wing by the procedure mentioned above, the following heuristic approach is used for obtaining γ_{SL} [18]:

$$\gamma_{SL} \approx \gamma_{SG} + \gamma_{LG} - 2\sqrt{\gamma_{SG}\gamma_{LG}}, \tag{6.5}$$

Therefore, using Eqs. (6.3) and (6.4), the contact angle θ can be expressed as :

$$\cos\theta \approx 2\sqrt{\frac{\gamma_{SG}}{\gamma_{LG}}} - 1. \tag{6.6}$$

Since γ_{LG} of water is known, as well as the contact angle of a water droplet on flat chitinous surface ($\theta = 105°$) [132], the surface energy of chitin is deduced from Eq. (6.6) $\gamma_{SG} \approx 10 \times 10^{-3}$ N·m^{-1}. Due to the approximation mentioned above, the chitin surface energy γ_{SG} is here undervalued. Indeed, since chitin is a dispersive polymeric material, optically close from well-known dispersive polymers such as polyethylene or polystyrene, its surface energy can be expected to be around 30×10^{-3} N.m^{-1}[16]. However, as it will be presented hereafter, this value is sufficient, in a first step, in order to describe qualitatively the wetting properties of the wing although the accuracy of the evaluated contact angles θ must be handled with great care.

In Fig. 6.9, brown and red lines denote the linear asymptotic trends in data when $\cos\theta_{eff} < 0$, *i.e.* when the wing is not wet. By contrast, the blue line denotes the behavior of the wet wing ($\cos\theta_{eff} > 0$), *i.e.* the hydrophilic regime. The horizontal green line corresponds to the process of hemiwicking, *i.e.* spreading of the water on the wing [18]. According to these results, a transition from a superhydrophobic regime to a hydrophilic regime is observed.

6.3.2 Theoretical analysis

Models of wetting processes are used hereafter in order to predict the contact angle of a water droplet on the wing. Specifically, they are used to describe the superhydrophobic, hydrophobic or hydrophilic behaviors of the wing. Two theoretical models are considered : the Cassie-Baxter model for the hydrophobic regime and Wenzel model for the hydrophilic regime.

The Cassie-Baxter (CB) model [6] allows to describe the wetting process on superhydrophobic and hydrophobic surfaces according to their roughness (*i.e.* nipple array). For a surface made of two different materials with different coverage areas, the contact angle θ_{CB} of the heterogeneous surface is given by:

$$\cos\theta_{CB} = f_1\cos\theta_1 + f_2\cos\theta_2. \tag{6.7}$$

[1] See Chapter 2.

where f_1 and f_2 are the fractional areas of each material ($f_1 + f_2 \geq 1$), and θ_1 and θ_2 are the contact angles, respectively.

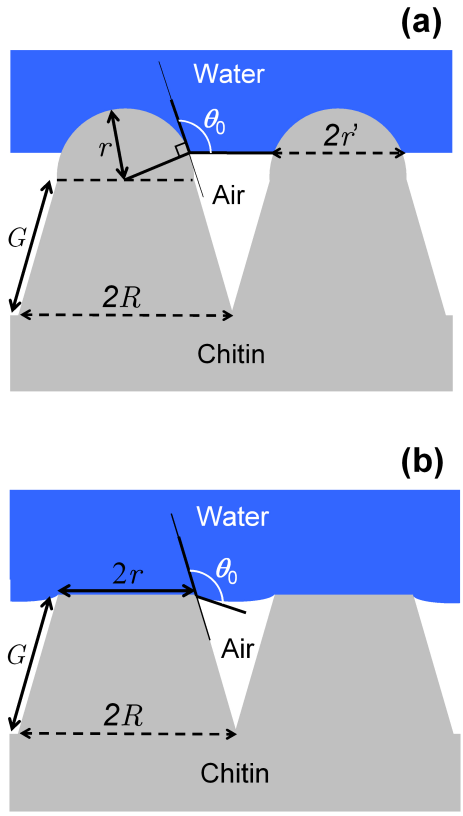

Figure 6.10: Wetting models under consideration. a: Wetting model from the full cicada's wing description. b: Wetting model without hemispheric top. The angle θ_0 corresponds to the Young's contact angle for a flat chitin surface.

Using the nipple geometry previously described, the wetting model shown on Fig. 6.10a is considered. The contact angle in the present case can be written as [134]:

$$\cos\theta_{CB} = n\pi R^2(1+\cos\theta)^2 - 1, \tag{6.8}$$

where n is the number of hemispheres per unit area for a hexagonal array, R is the radius of the hemisphere, and θ is the contact angle of a droplet deposited on flat chitin. This well-known equation, can be simply derived from Eq. (6.7) by assuming that $\theta_1 = \theta$ and $\theta_2 = 180°$. Indeed, θ_2 is the contact angle between a droplet and air, which is assumed to be 180°. Fractional areas can be easily derived from trivial geometrical considerations. On Fig. 6.9, Eq. (6.8) is plotted as the purple curve with $\theta_{CB} = \theta_{eff}$, using geometrical parameters mentioned in Section 6.1 and measured from SEM pictures. Gold and red lines show wetting trends experimentally observed by contrast to the theoretical model [134]. Though the theoretical curve and the experimental data do not perfectly match, the trends are the same. Differences are likely due to the fact that the water/air interface (see Fig. 6.10a) is not truly a planar one, modifying then the conditions for which the Gibbs energy is minimized [18]. Nevertheless, more accurate modeling

is a complex task far beyond the scope of the present work [18].

It is noteworthy that, using Eq. (6.8), a theoretical contact angle of 151° for water is found by contrast with the measured value of 146°, *i.e* there is less than 4% difference between theory and experiment.

In order to clearly demonstrate the essential role of the hemispherical top, the wetting properties of the conical base structure without the top hemisphere is investigated (Fig. 6.10b). In this case, the Cassie-Baxter contact angle is simply given by:

$$\cos\theta_{CB} = f\cos\theta_0 + (f-1)\,, \tag{6.9}$$

with $f = \pi r^2/S$ and $S = a_0^2\sqrt{3}/2$. The linear dependance, which is plotted in Fig. 6.9 as a black solid line, leads to much less satisfactory agreement with data, as compared with the quadratic dependence (purple curve) pertaining to the hemispherical top, *i.e*. Eq. (6.8). Indeed, for water ($\theta_0 = 105°$), a theoretical contact angle of $\theta_{CB} = 111°$ is predicted by Eq. (6.9), whereas a value of 151° was determined previously by Eq. (6.8). Therefore, only the model including the hemispherical top is able to account for the superhydrophobicity of the wing.

The hydrophilic behavior of a corrugated surface, on the other hand, can be described thanks to the Wenzel (W) model [5]. In this case, the contact angle is given by:

$$\cos\theta_W = r_o\cos\theta, \tag{6.10}$$

where r_o is the roughness factor which is in our case given by

$$r_o = \frac{2\pi r^2 + \pi G(R+r) + \frac{a_0^2\sqrt{3}}{2} - \pi R^2}{S}, \tag{6.11}$$

with $S = a_0^2\sqrt{3}/2$, r the radius of the hemisphere, R the radius of the base of the cone, G the length of the cone side and a_0 the spatial period. Eq. (6.10) is a linear relation between the effective contact angle and the contact angle on a flat surface made of the same material. On Fig. 6.9, Eq. (6.10) is plotted as blue curve with $\theta_W = \theta_{eff}$, using geometrical parameters mentioned in Section 6.1 and measured from SEM pictures. Here, the model matches very well with the experimental data.

The fact that the wetting models underline the role of the top hemisphere in the wetting phenomena, and especially in the hydrophobic behavior of the cicada wings, is emphasized. In the wetting regime, the whole structure geometry must be considered to explain the wetting.

6.4 Summary

While it is known that cicada wings possess both hydrophobic [135] and anti-reflective properties [130], the present work underlined the two-in-one character of the geometrical features leading both to the optical and wetting properties of the cicada [30]. From scanning electron microscopy, it was shown that the cicada wing consisted of a thick chitinous layer, which each side was covered by a nanostructured device in the form of an hexagonal nipple array. Each nipple

was modeled by a truncated cone topped by an hemisphere. An original wetting experiment with various chemical species as well as comprehensive optical measurements providing the complex refractive index of the chitinous wing were performed. From optical simulations and using an analytical wetting model, we demonstrated the character of the two functional levels of the nipple array. It is concluded that the hemisphere on the top of the nipple is useful for the superhydrophobic character of the cicada wing. This half-sphere playes no optical role. By contrast, the truncated cone plays no significant role in the hydrophobic behavior while it is found to be fundamental for ensuring transparency of the cicada wing (anti-reflection). Therefore, the nipple array nanostructure in the grey cicada can be considered as a two-in-one device: a hemisphere top which allows a strong water repellency and a truncated cone which ensures anti-reflective properties.

Part IV

Nanophotonical approach of surface multifunctionality at the nanoscale

Chapter 7

The tuning of Lifshitz-van der Waals interactions

Many fundamental aspects and practical issues in the physics of interfaces are related to controlling interactions between surfaces [18][99]. In his seminal article [12], De Gennes pointed out the importance of van der Waals and electrostatic forces in adsorption, adhesion, and wetting phenomena. Recently, it became obvious that controlling forces between macroscopic bodies or surfaces are crucial for a variety of applications such as mechanics of nanomachines, stability of colloids, and communication between biological cells [18][99][136][137].

This chapter focuses on small-correlation-length nanostructures with steep features for tuning Lifshitz-van der Waals interactions. In this case, the assimilation of the surface corrugation to a graded refractive index multilayer is justified and allows simplifying greatly the application of nonadditive methods while still taking fully into account electrodynamical coupling between features as explained below. The novel concept of manipulating quantum vacuum photon modes at the sub-10-nm scale for tuning Lifshitz-van der Waals interactions is introduced.

7.1 Description of the interacting macroscopic bodies systems

In order to investigate the impact of steep featured nanostructures on Lifshitz-van der Waals interactions, the two following models are proposed. Both model systems highlight **the same physical phenomenon** that is the tuning of the Lifshitz-van der Waals interactions and validate the computational methods to describe it. These two models will be individually developed in details in Chapters 8 and 9.

7.1.1 The first system : corrugated polyethylene-vacuum-water

The first two-body system under study consists of a nanostructured surface and a droplet of water separated by a distance L (Fig. 7.1a). Since the water droplet is much bigger than the surface corrugation features, it can be described by a flat slab (Fig. 7.1b). The thickness of the slab is arbitrarily taken at 1 μm. The surface is nanostructured with cones of height h

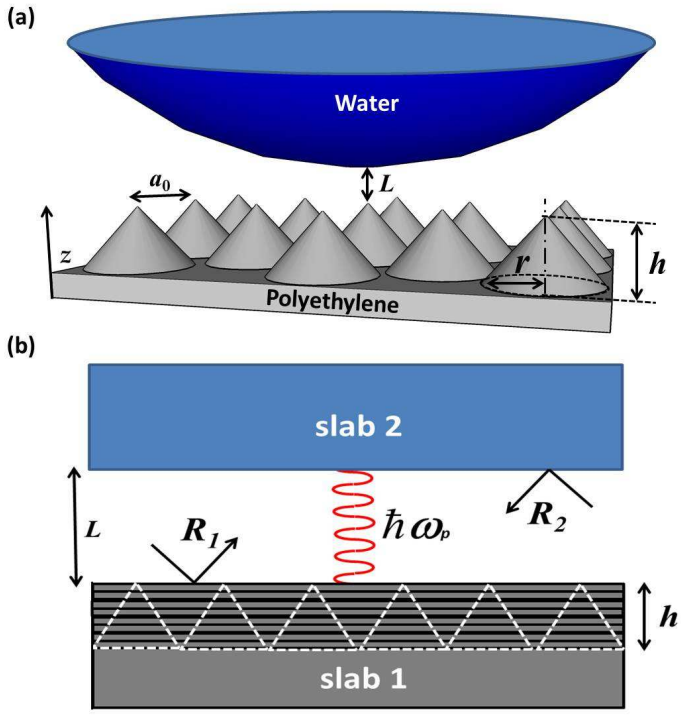

Figure 7.1: (a) Corrugated surface separated by a distance L from a water droplet. The surface of the droplet can be considered as flat at the scale of corrugation. (b) Approximation of the two-body system. R_1 and R_2 are the reflection coefficients of the effective multilayer (slab 1) and of the water droplet (slab 2), respectively. Quantum vacuum photon modes $\hbar\omega_p$ allowed between the two slabs are pictured in red.

arranged on a hexagonal lattice with a lattice parameter chosen to be $a_0 = 10$ nm. The cone base radius is $r = 5$ nm and the cone height h ranges from 10 to 100 nm (aspect ratio h/a_0 from 1 to 10). In the following, the nanostructured surface is assumed to be made of polyethylene. The choice of polyethylene was motivated by the need to work with an apolar polymer [18]. Such a polymer only possesses an apolar component for in surface energy, *i.e.* its cohesion energy is solely due to Lifshitz-van der Waals interactions. Since the lattice parameter a_0 has subwavelength dimensions and polyethylene permittivity is close to 1 at wavelengths below 10 nm [138], the corrugated surface can be, *a priori*, described by a continuous effective material with a graded refractive index along its thickness [30] (Fig. 7.1b). A detailed discussion on the validity of such model is provided further. The effective dielectric function of the corrugated surface can be expressed by [42][30]:

$$\varepsilon(z) = 1 + (\varepsilon_{material} - 1)f(z), \tag{7.1}$$

where $\varepsilon_{material}$ is the dielectric function of the bulk material and $f(z)$ is a filling factor given by: $f(z) = \pi r^2(z)/S$ with $S = a_0^2\sqrt{3}/2$ and $r(z)$ the radius of the circular section of the cones at coordinate z. The system is then reduced to a water slab and an effective multilayer (Fig. 7.1b). In computations, polyethylene permittivity is described by a modified Lorentz oscillator

model [139]:

$$\varepsilon(\omega) = \varepsilon_\infty + \sum_{p=1}^{N} \frac{\Delta\varepsilon_p(\omega_p^2 - i\gamma_p^{'}\omega)}{\omega_p^2 - 2i\omega\gamma_p - \omega^2}, \tag{7.2}$$

where ε_∞ is the permittivity at infinite frequency, ω_p is the plasma frequency, γ_p and $\gamma_p^{'}$ are related to relaxation processes associated to the p^{th} oscillator and $\Delta\varepsilon_p$ is defined such as $\sum_{p=1}^{N}\Delta\varepsilon_p = \varepsilon_{stat}$ - ε_∞ with ε_{stat} the permittivity at zero frequency. The values of these parameters are listed in Table (7.1) and were obtained by fitting ($N = 2$ oscillators) the experimental dielectric function of polyethylene which tends to unity at wavelengths shorter than 10 nm [138]. The water slab is also described by a dielectric function, the analytical form and parameters were taken from [140].

Actually, the water droplet is in equilibrium with water vapor. Therefore, the medium separating the surface and the droplet should be vapor instead of vacuum. However, since the water vapor dielectric constant is very close to that of vacuum at all wavelengths of interest and whatever the vapor partial pressure is [141], there is no difference in considering a vacuum interface instead of a vapor interface from the point of view of electrodynamical calculations. Moreover, the water slab is considered to be in a Cassie state in which a flat meniscus is assumed[1] [6]. In fact, a more realistic meniscus profile, like overhanging profile, could be modeled as a thin effective layer. This optically thin layer, however, would not lead to significant effects in the electrodynamical calculations of the van der Waals forces.

	$p = 1$	$p = 2$
$\Delta\varepsilon_p$	0.2479	0.970
ω_p	1.27×10^{16}rad s^{-1}	1.88×10^{16}rad s^{-1}
γ_p	9.66×10^{14}rad s^{-1}	5.27×10^{15}rad s^{-1}
$\gamma_p^{'}$	1.26×10^{16}rad s^{-1}	3.63×10^{15}rad s^{-1}

Table 7.1: Parameters of the dielectric function of polyethylene.

This system will be investigate in details in Chapter 8.

7.1.2 The second system : corrugated polyethylene-water-flat polyethylene

The second two-body system under study consists of a nanostructured polyethylene surface and a flat polyethyelene surface with water as intervening medium (Fig. 7.2). The corrugated polyethylene surface is patterned with the same cones mentioned above with the same dimensions and are approximated by the same effective medium. The water is assumed to be in a Cassie state with the corrugated polyethylene surface and both materials (polyethylene and water) are modelized with the dielectric functions presented above. This system will be investigate in detail in Chapter 9.

[1]Rigorously, the Cassie state would require checking the roll-off angle of the water droplet is below 10°. Since our simulation can only be carried out in a static regime, we cannot have access to this dynamic quantity. However, assuming a Wenzel state (the water fills the air gaps between the cones) would not affect the main results of our study since the graded index profile of the cones is maintained (see further).

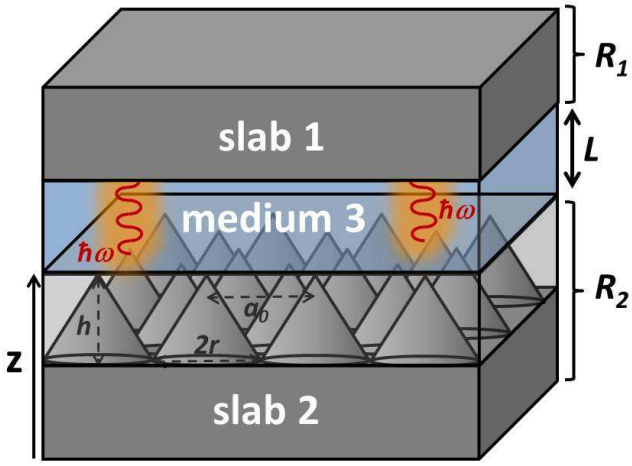

Figure 7.2: Bodies 1 and 2 interacting *via* an intervening medium 3. The two bodies are separated by a distance L. R_1 (R_2) is the Fresnel reflection coefficient of slab 1 (slab 2). The surface of body 2 is nanopatterned with corrugations that are described by a graded effective medium.

7.1.3 The effective medium

At this point, it is important to stress that the use of the effective medium approach has to be justified with great care. Indeed, this approximation usually requires the separation distance L to be equal to or larger than the lattice parameter a_0 of the periodically nanostructured surface [142]. The reason is that the distance is one of the main parameters determining the nature of the electromagnetic modes (radiative or evanescent) involved in the calculation of the Lifshitz-van der Waals interaction.

In the case of a separation distance much larger than the lattice parameter, radiative modes are dominant. The wavelegnths of the radiative modes which are of the order of the lattice parameter (around 10 nm) can ”see” the details of the structures and therefore are diffracted. Diffracting orders cannot be generated by the effective medium, of course. This invalidate the use of effective medium approximation.

In the case of a separation distance shorter than the lattice parameter, although radiative modes still exist, evanescent modes are dominant and are able to reproduce the details of the nanostructure, thereby invalidating the effective medium approach [143][144]. Indeed, the effective medium used for describing the patterned surface can only reproduce the graded refractive layer profile of the surface but obviously not its geometry. However, in the present situation, the effective medium approach remains valid for separation distances shorter than the lattice parameter. This nonintuitive result emerges from the weakness of the coupling between diffracted and specular orders due to both the optical properties of polyethylene and the steepness of the corrugation. The detailed justification is provided hereafter.

7.2 Accuracy of the effective medium approach

7.2.1 The far field

In order to investigate the accuracy of the effective medium approach at describing the optical properties of the cones patterned surface in the far field, *i.e.* $L >> a_0$, the intensity reflection coefficient $|R_1|^2$ (at normal incidence) of a surface patterned with cones of height $h = 10$ nm was simulated using the RCWA method with different numbers of reciprocal lattice vectors $N_{\vec{g}}$ (Fig. 7.3). Cones were described by cylinders stacks in simulations (Fig. 7.4). While the

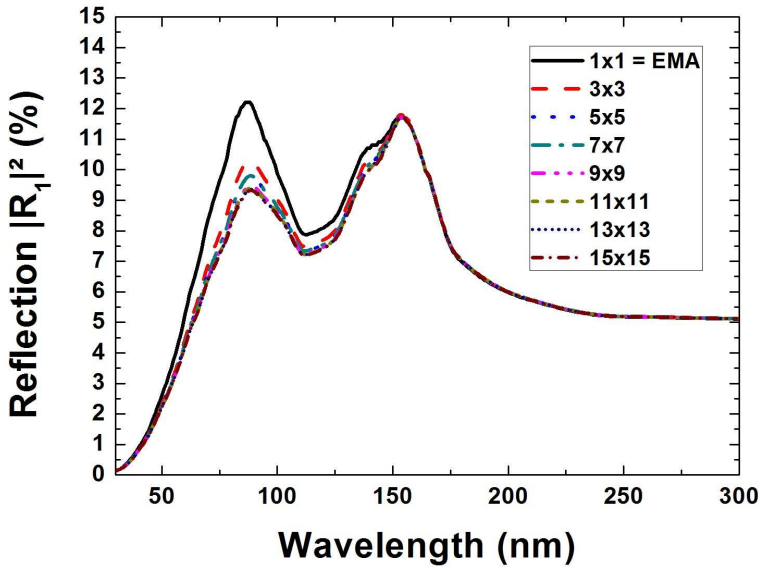

Figure 7.3: Intensity reflection coefficient (at normal incidence) of 10 nm height cones patterned surface. Different numbers $N_{\vec{g}}$ of reciprocal lattice vectors were tested. RCWA calculation (dashed/dotted line) and EMA (effective medium approximation) calculation (solid line).

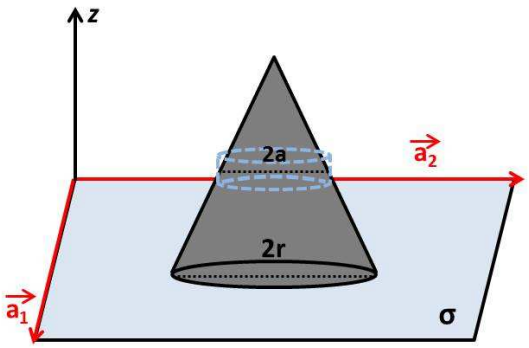

Figure 7.4: Primitive cell of the periodically patterned structure under study. In computations, the cone is described by a stack of cylinders of radius $a \in [0,r]$.

intensity reflection coefficient is relatively well approximated by the effective medium approach for wavelengths greater than 150 nm, several reciprocal lattice vectors are required for describing the optical properties in the range of 60 nm to 150 nm. Indeed, in this range, a number $N_{\vec{g}}$ = 9×9 of reciprocal lattice vectors is required for the intensity reflection coefficient to converge

(Fig. 7.3). Such a result is not surprising since, in this range, wavelengths are able to "see" the patterning of the surface. The use of the effective medium approach is therefore inappropriate for describing the diffraction phenomena in this wavelength range. In other words, the effective medium approach of the cones patterned surface is valid in the far field only for wavelengths greater than 150 nm. Note that for wavelengths lower than 60 nm, polyethylene becomes transparent (Fig. 7.5), which obviously validates the use of the effective medium approach.

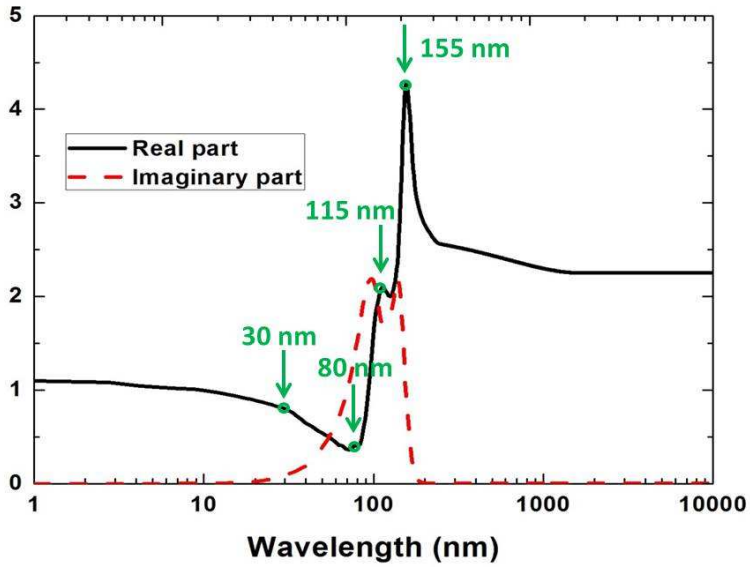

Figure 7.5: Dielectric function ε_s of polyethylene. Pointed values are those used for numerical simulations (Fig. 7.9).

7.2.2 The near field

While dealing with the near field (evanescent modes), *i.e.* $L \leq a_0$, which plays a non trivial role in the calculation of the interaction potential energy at short distances [145][65], it could be objected that the effective medium approach is inappropriate. Indeed, the evanescent near field is expected to exhibit lateral fluctuations mimicking surface corrugations [146]. Therefore, the effective medium approach is *a priori* inappropriate for describing accurately these fluctuations. However, the careful analysis described below leads to requalify this restriction in the specific case of subwavelength periodically patterned surfaces.

Let us consider the sub-10 nm cones patterned surface involved in the present study which diffracts an incident wave into a radiative specular order g_0 wave and evanescent diffracted order g_i waves (Fig. 7.6). The specular order couples with all the evanescent diffracted orders, which are all coupled with each other as well: together, they constitute the fluctuating near field (Fig. 7.6). Since the effective medium does not possess the geometry of the pattern, the fluctuation of the near field cannot be reproduced. Now, the question is : is this problematic or not ? Let us formally examine such a coupling in the theoretical framework of the Rigorous Coupled Wave

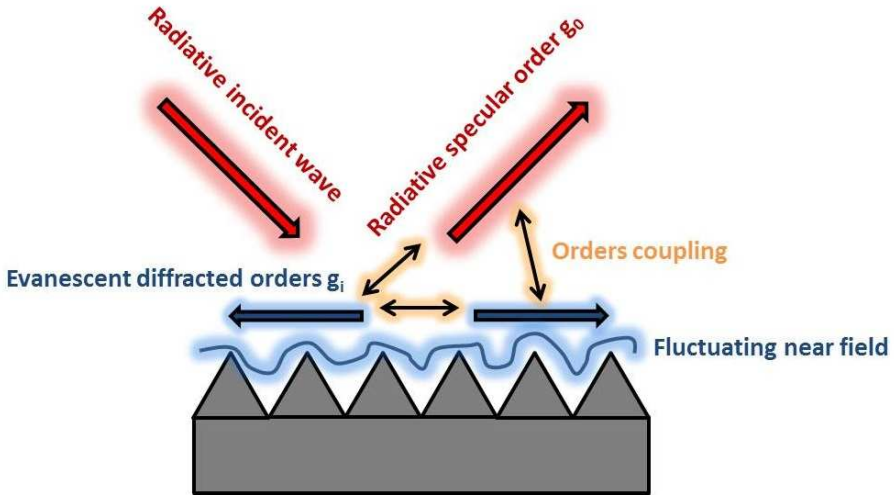

Figure 7.6: Sketch of the coupling between the specular order and the diffracted orders which create the fluctuating near field.

Analysis method[2] [56]. The Fourier series expansion of the dielectric constant writes as :

$$\varepsilon(z, \overrightarrow{\rho}) = \sum_{\overrightarrow{g}} \varepsilon_{\overrightarrow{g}}(z) e^{i \overrightarrow{g} . \overrightarrow{\rho}} \tag{7.3}$$

where $\overrightarrow{\rho}$ denotes a real-space vector in the primitive cell with basis vectors $\overrightarrow{a_1}$ and $\overrightarrow{a_2}$ (Fig. 7.4), and $\overrightarrow{g}$ is a reciprocal lattice vector. By virtue of Floquet-Bloch theorem, the electric $\overrightarrow{E}$ and displacement $\overrightarrow{D}$ fields expand as :

$$\overrightarrow{E}(z, \overrightarrow{\rho}) = \sum_{\overrightarrow{g}} \overrightarrow{E}_{\overrightarrow{g}}(z) e^{i(\overrightarrow{g} + \overrightarrow{k}_{//}) . \overrightarrow{\rho}} \tag{7.4}$$

$$\overrightarrow{D}(z, \overrightarrow{\rho}) = \sum_{\overrightarrow{g}} \overrightarrow{D}_{\overrightarrow{g}}(z) e^{i(\overrightarrow{g} + \overrightarrow{k}_{//}) . \overrightarrow{\rho}} \tag{7.5}$$

Since $\overrightarrow{D} = \varepsilon_0 \varepsilon(z, \overrightarrow{\rho}) \overrightarrow{E}$, we can re-write $\overrightarrow{D}_{\overrightarrow{g}}(z)$ as :

$$\overrightarrow{D}_{\overrightarrow{g}}(z) = \sum_{\overrightarrow{g'}} \varepsilon_0 \varepsilon_{\overrightarrow{g},\overrightarrow{g'}} \overrightarrow{E}_{\overrightarrow{g'}}(z) \tag{7.6}$$

where $\overrightarrow{g'}$ is another reciprocal lattice vector and the Fourier matrix element $\varepsilon_{\overrightarrow{g},\overrightarrow{g'}}$ expresses the coupling between diffracting orders $\overrightarrow{g}$ and $\overrightarrow{g'}$. When describing the cones by cylinders stack, $\varepsilon_{\overrightarrow{g},\overrightarrow{g'}}$ in a given layer has the following analytical expression :

$$\varepsilon_{\overrightarrow{g},\overrightarrow{g'}} = \varepsilon_m \delta_{\overrightarrow{g},\overrightarrow{g'}} + (\varepsilon_s - \varepsilon_m) \frac{2\pi a^2}{\sigma} \frac{J_1(\mid \overrightarrow{g} - \overrightarrow{g'} \mid a)}{\mid \overrightarrow{g} - \overrightarrow{g'} \mid a} \tag{7.7}$$

[2]See Chapter 3

where a is the cylinder radius at coordinate z (Fig. 7.4), J_1 is the first-order Bessel function, ε_m is the dielectric constant of surrounding medium (here, vacuum), ε_s is the dielectric constant of polyethylene, $\delta_{\overrightarrow{g},\overrightarrow{g'}}$ is the Kronecker symbol and σ is the primitive cell area (Fig. 7.4). Due to the subwavelength size of the corrugation period, mode coupling gives rise to evanescent waves propagating along the surface as explained hereafter. Such evanescent waves constitute the fluctuating near field.

Careful examination of Eq. (7.12) indicates that the coupling constant $\varepsilon_{\overrightarrow{g},\overrightarrow{g'}}$ vanishes in two limit cases: (1) for low refractive index contrast, *i.e.* $\varepsilon_s \rightarrow \varepsilon_m$, (2) in the topmost layers where the cylinder radius a becomes very small and ultimately tends to zero (note that $\lim_{a\rightarrow 0} \frac{J_1(|\overrightarrow{g}-\overrightarrow{g'}|a)}{|\overrightarrow{g}-\overrightarrow{g'}|a} = \frac{1}{2}$). As a consequence, in both limit cases, due to the extremely weak coupling, fluctuations of the near field tend to vanish. In the present study, the limit case 1 is always reached at wavelengths equal or shorter than about 30 nm because of the dielectric properties of polyethylene, *i.e.* $\mathbb{R}(\varepsilon_s) \rightarrow 1$ and $\mathbb{IM}(\varepsilon_s) \rightarrow 0$ (Fig. 7.5). On the other hand, since evanescent waves of interest are those that propagate near the very top of the cones and given the cones steepness thereof (*i.e.* $a \rightarrow 0$) the limit case 2 is always satisfied. Therefore, both the effective medium approach and the three dimensional treatment should give the same description of the near field within the cavity. For illustrative purpose, the coupling intensity $\left|\varepsilon_{\overrightarrow{0},\overrightarrow{g'}}\right| / \left|\varepsilon_{\overrightarrow{0},\overrightarrow{0}}\right|$ between the specular order and diffracting orders versus the top radius is illustrated for a wavelength of 155 nm (Fig. 7.7). As expected, the cones steepness gives rise to a

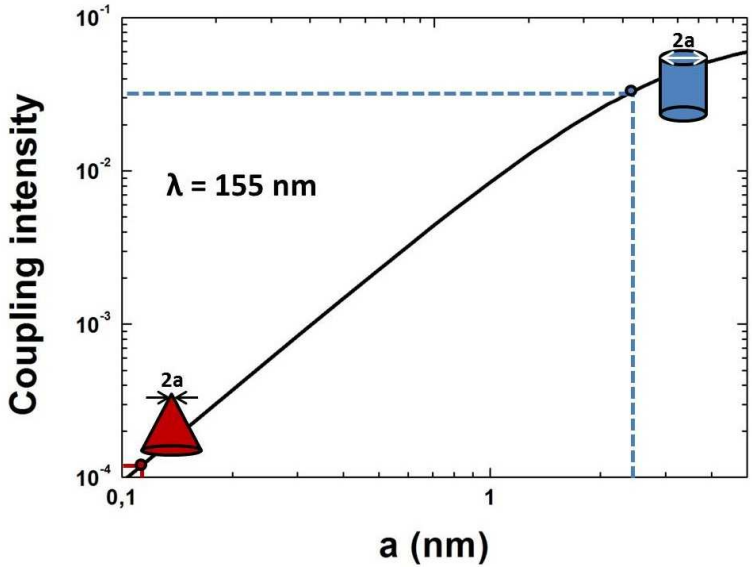

Figure 7.7: Coupling intensity between the specular order and the diffracting orders.

very weak coupling. These predictions need however to be verified by numerical simulations.

In order to probe the evanescent waves inside the cavity[3], the diffracted field pattern which originates from oscillating dipoles inserted inside the cavity was numerically simulated, using a finite difference time domain (FDTD) [55][147] home-made code. The corrugated polyethylene-

[3]Let us recall that the cavity is defined by the space between the flat surface and the plane touching the tops of the cones in Fig. 7.1 and 7.2.

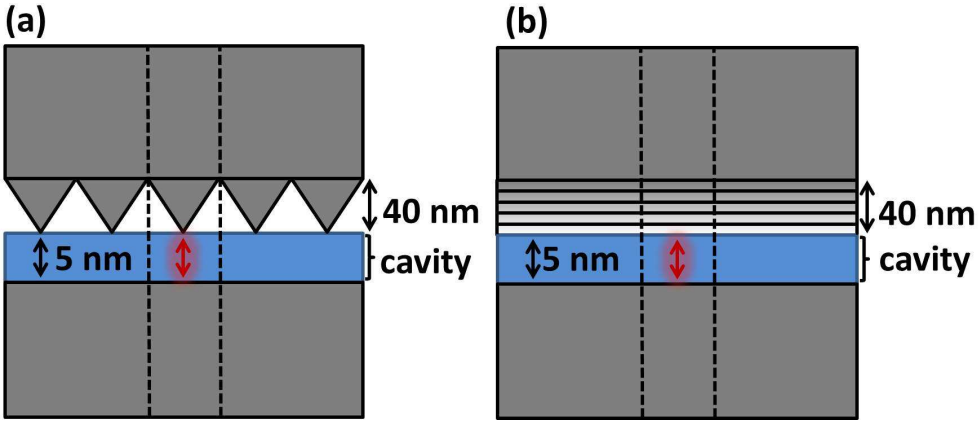

Figure 7.8: Sketches of the configuration used in FDTD simulations for the cone array structure (a) and its corresponding EMA description (b). The red arrow denotes an oscillating dipole and dashed lines delimit the computational cell. One dipole is inserted in each cells and periodically repeated. The grey regions are polyethylene, the blue region is water (in Cassie state).

water-flat polyethylene system is chosen here for illustration, without loss of generality. Such a dipole-excitation model emulates the electromagnetic field arising from quantum fluctuations inside the cavity. Both the actual three dimensional structure (Fig. 7.8a) and its corresponding effective medium description (Fig. 7.8b) were simulated using cones height of 40 nm and a separation distance of 5 nm, as an illustration. The electromagnetic responses of both configurations to dipole excitation were probed through normalized field intensity maps (Fig. 7.9). Maps are drawn for each computational cell (dashed lines on Fig. 7.9) and display only the diffracted field *i.e.* dipole radiation removed.

The wavelengths of the radiating dipole (30 nm, 80 nm, 115 nm and 155 nm) were selected in order to sample the spectral range which is relevant to polyethylene, according to its optical properties (Fig. 7.5). At all these wavelengths except 30 nm, the limit case 1 is not reached (Fig. 7.5) but the limit case 2 is reached near the top of the cones. In all cases, no significant differences are observed between the electromagnetic responses of the cone array structure and its effective medium approach description (Fig. 7.9, relative error lower than 2%). This result demonstrates that the fluctuations of the evanescent waves resulting from the coupling between diffracted orders and specular order are extremely weak, which therefore fully justifies the use of effective medium approach in the present case.

Note that, for a cavity made of materials with free charges, surface plasmon polaritons would produce strongly modulated evanescent waves which would dominate Lifshitz-van der Waals interactions [65]. In this case, the effective medium approach description would obviously fail. Since polyethylene cannot endorse surface plasmon polaritons, the above mentioned problem is excluded here.

In summary, the shallowness of evanescent waves fluctuations justifies the use of an effective medium approach for short separation distances. The underlying physical reason is the weak modes coupling due to both the optical properties of polyethylene and the steepness of the corrugation. The use of a graded refractive index profile for an effective medium approach

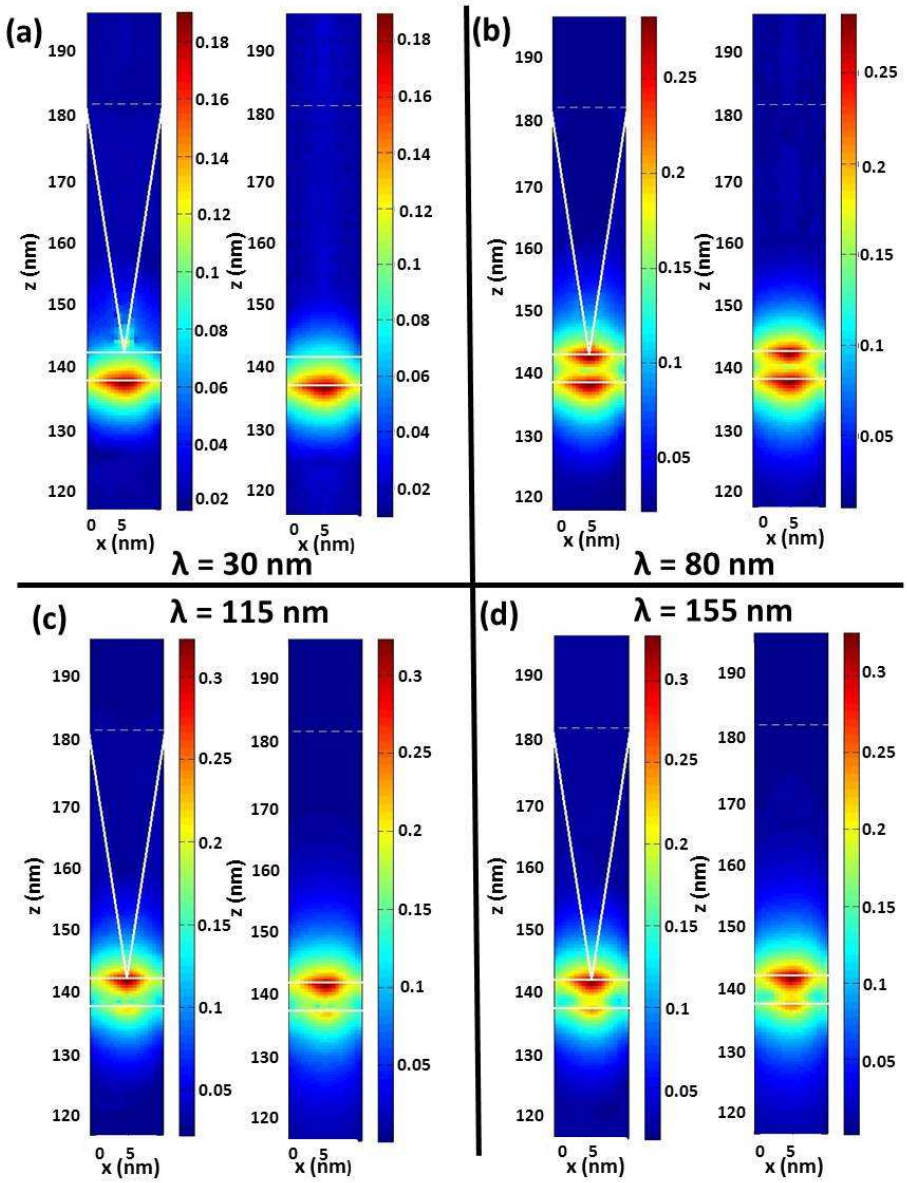

Figure 7.9: Maps of the normalized intensity of diffracted field at different wavelengths in the three dimensional structure (left charts in each panel) and its EMA description (right charts in each panel).

description turns out to be reliable in rendering these shallow fluctuations.

7.2.3 Preliminary conclusion

From the results presented above, it appears that, in the present case, the effective medium approach is suitable for describing the near field but not the far field. However, in the following, only short separation distances will be considered ($L = 5 \rightarrow 10$ nm) for which the evanescent modes, associated to the near field, are dominant compared to the radiative modes, associated to the far field. Therefore, although slight differences are expected between the effective medium approach and the three dimensional treatment (see further), the global results will not be

affected by such an approximation.

In addition, the effective medium approach avoids numerical stability issues while dealing with the direct computation of the scattering matrices of steep three dimensional structures of low refractive index contrast optical, which are needed for the evaluation of the Lifshitz-van der Waals force. This is a considerable advantage of the proposed method.

7.3 Numerical results for the corrugated polyethylene-vacuum-water system

For illustrating the tuning of the Lifshitz-van der Waals interactions, let us now consider the corrugated polyethylene-vacuum-water system. Since the Lifshitz-van der Waals potential energy relies on the optical properties of the interacting bodies, it is interesting to investigate the reflection properties of the corrugated polyethylene surface depending on the cones height. Thanks to the RCWA method, the intensity (square modulus) reflection coefficient of the nanostructured polyethylene surface $|R_1(\lambda)|^2$ was computed (see Fig. 7.10a where only normal incidence is considered for the sake of clarity). Broadband antireflection character of the corrugated surface was obtained by increasing the height of the cones: the higher the cones, the lower the reflection. Such a result is not surprising since increasing the cones height reinforces the graded refractive index profile of the surface which leads to an improvement of its antireflective behavior.

The Lifshitz-van der Waals potential energy is obtained using Eq. (7.8) (derived in Chapter 5) :

$$U^{LW}(L) = \frac{\hbar}{2\pi} \sum_{m=s,p} \int \frac{d^2 k_{//}}{(2\pi)^2} \int_0^\infty d\xi \ln \left[1 - R_1^m(i\xi, \overrightarrow{k}_{//}) R_2^m(i\xi, \overrightarrow{k}_{//}) e^{-2\kappa L} \right], \tag{7.8}$$

where $\kappa = \sqrt{\frac{\xi^2}{c^2} + \left| \overrightarrow{k}_{//} \right|^2}$, ${R_1}^m$ (${R_2}^m$) is the complex reflection coefficient of slab 1 (slab 2) (Fig. 7.1b) in the m polarization state (s or p states) and $k_{//}$ is the parallel component of the photon wave vector. The use of the complex angular frequency $\omega = i\xi$ arises from numerical computation considerations[4]. The spectral integration is performed over the wavelength range from 2 nm to 10 μm (as displayed on Fig. 7.10a). The integration over the photon wave vectors $\overrightarrow{k}_{//}$ employs a method proposed by Monkhorst and Pack [148] presented in Appendix A. The method uses a number of photon wave vectors $N_{\overrightarrow{k}_{//}} = 29 \times 29$ for flat surface and $N_{\overrightarrow{k}_{//}} = 7 \times 7 = 49$ for corrugated surfaces. Such a number is the result of convergence studies presented in Appendix B.

First of all, the thickness of the slab on which lay the cones and the thickness of the water slab should be determined such that the potential energy between a flat polyethylene slab and a water slab converges. Such a result is presented on Fig. 7.11 and shows that, for a 100 nm-thick polyethylene/water slabs, the potential energy converge. Indeed, it can be shown that, in the present case, the condition $t \times n/\lambda > 1$ (quickly oscillating phase condition) is verified beyond a 50 nm slab thickness. This thickness value will be used in simulations.

[4] See Chapter 5.

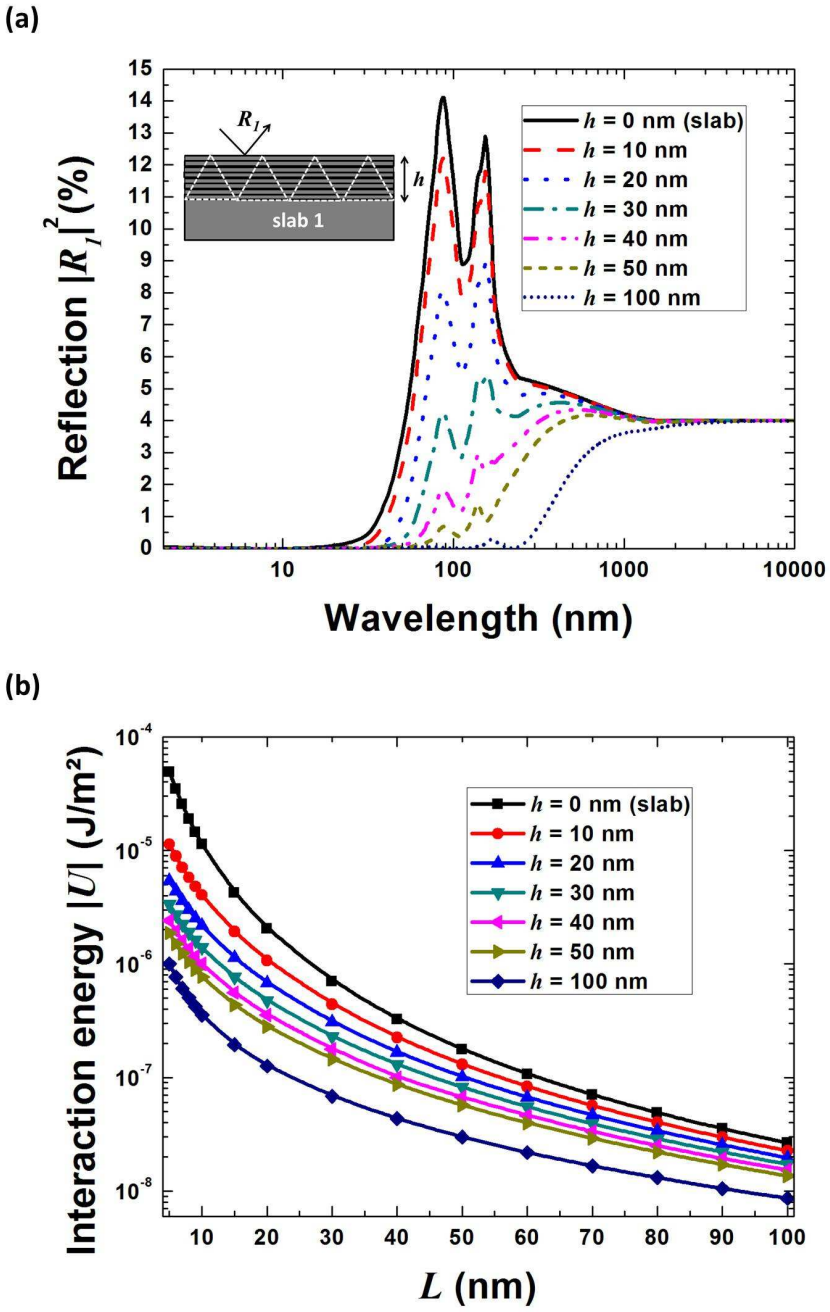

Figure 7.10: Intensity reflection coefficient (at normal incidence) of corrugated polyethylene slabs with cones of various heights h. (b) Interaction energy between a water droplet and corrugated polyethylene slabs.

By numerically solving Eq. (7.8), the interaction energy between the nanostructured surface and the water droplet was determined as a function of the cone height (Fig. 7.10b). The black line corresponds to the interaction energy between a flat polyethylene surface and a water droplet. As the height of cones is increased, the interaction energy is clearly altered: the higher the cones, the lower the potential energy (Fig. 7.10b). In other words, the Lifshitz-van der Waals potential energy decreases as the antireflection character of the polyethylene surface increases

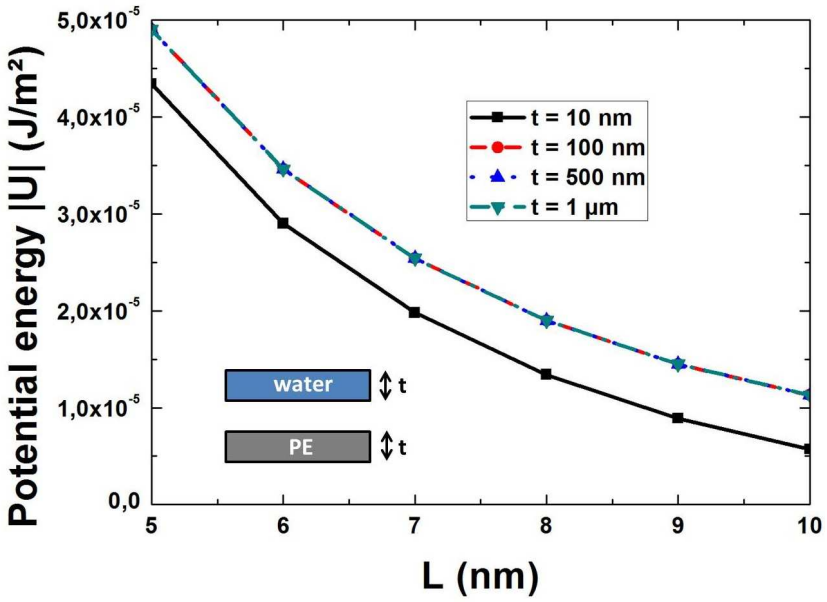

Figure 7.11: Convergence of the potential energy between a flat polyethylene slab and a water slab with respect to slabs thickness.

(Fig. 7.10a). This fundamental point is the main finding of this study: **the alteration of Lifshitz-van der Waals potential energy is due to the presence of surface corrugation** [91]. Note that the same phenomenon is obtained with the second system under study.

It is important to stress that results are here presented for separation distances shorter and much larger than the lattice parameter. As explained above, the effective medium approach is less suitable in the case of separation distance larger than the lattice parameter. However, the three dimensional treatment of the cones patterned surface will modify the magnitude of the energy due to the integration of reciprocal lattice vectors in the calculation (see further) but not the effect underlined here. Therefore, the main result presented for separation distances larger than the lattice parameter, *i.e.* the alteration of Lifshitz-van der Waals potential energy is due to the presence of surface corrugation**,** remains valid.

7.4 Discussion

7.4.1 The quality factor

Let us switch again from a system to another and consider the corrugated polyethylene-water-flat polyethylene system. Phenomenologically, the above result can be explained by the fact that the increase of the cone height h causes the decrease of the intensity reflection coefficient of the nanopatterned polyethylene slab $\mathcal{R}_1$. Consequently, the quality factor Q of the Fabry-Perot cavity also decreases (Fig. 7.12a) since [149]:

$$Q = -2\pi \frac{1}{\ln(\mathcal{R}_1 \mathcal{R}_2 (1 - \mathcal{A}_3)^2)} \frac{2L}{\lambda}, \tag{7.9}$$

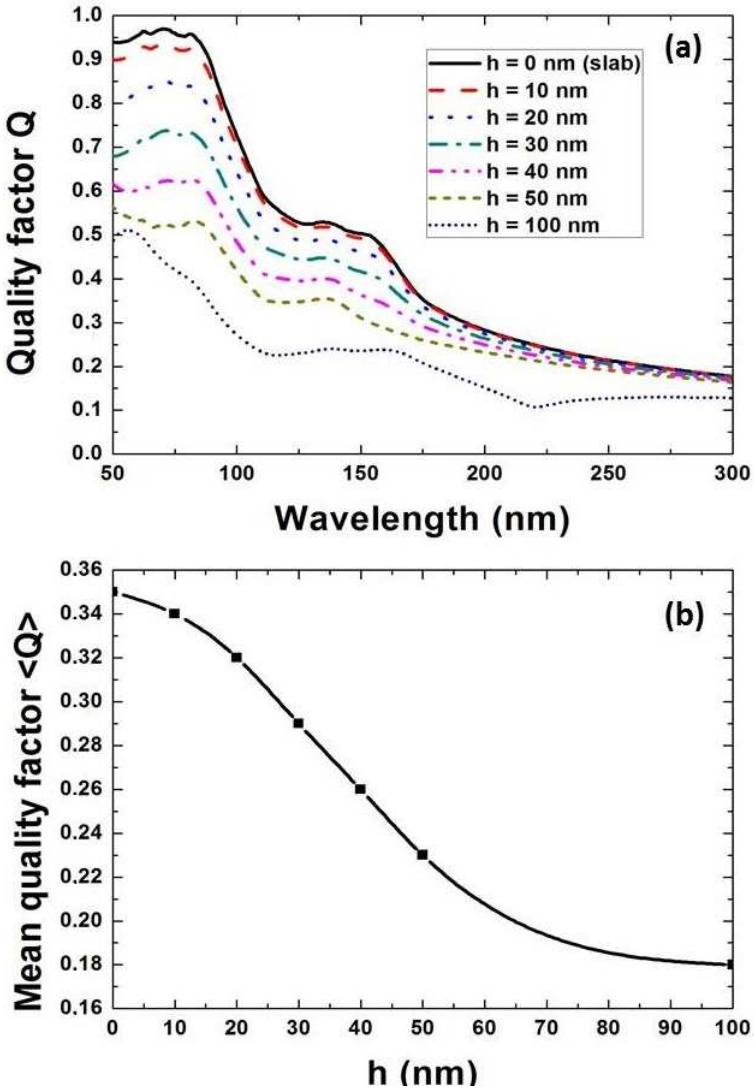

Figure 7.12: (a) Quality factor Q of the Fabry-Perot cavity formed by the flat polyethylene slab and the patterned polyethylene slab with water as intervening medium. Q is given against the wavelength for various cone heights. (b) Mean value (integration over wavelength) of the quality factor of the cavity described above.

where $\mathcal{R}_i = |R_i|^2$ and $\mathcal{A}_3$ is the optical absorption loss of the intervening medium (3) for a single path in the cavity (i.e. $\mathcal{A}_3$ is given by Beer-Lambert law). Moreover, the mean value of the quality factor $< Q >$ was calculated by integration of Eq. (7.9) in the relevant spectral range from 50 nm to 300 nm (Fig. 7.12b). The decrease of $< Q >$ as the cones height increases can be observed, down to 49 % of the initial value (*i.e.* for flat slabs) (Fig. 7.12b). As Q decreases, the electromagnetic energy stored into the Fabry-Perot cavity is reduced [149]; *i.e.*, the number of quantum vacuum photon modes available within the cavity and which contribute to the interaction potential energy $U(L) \propto \sum_k \hbar\omega_k(L)$ diminishes. Therefore, the attractive behavior of the interaction potential energy becomes weaker. On overall, controlling the optical properties of the cavity enables tuning the strength of the attractive force. It is noteworthy

that such an interpretation, although based on solid physical ground (*i.e.* the energy storage in an optical cavity), relies on a heuristic approach and still requires the establishment of a direct theoretical link between the quality factor and the Lifshitz-van der Waals interaction.

7.5 The three dimensional treatment

The three dimensional treatment of the periodically patterned surface instead of its effective one leads to the same trends presented above (Fig. 7.10) but are much more difficult to deal with due to numerical stability issues. Indeed, while dealing with the RCWA method, the individual scattering matrices S_1 and S_2 of each components of the system (Fig. 7.1), which are required for the calculation of the energy, are ill conditioned for slabs thickness greater than 10 nm when introducing reciprocal lattice vectors in the numerical simulations. However, for 10 nm thick slabs, the three dimensional treatment can be conducted. Therefore, although the potential energy does not converge for such a slab thickness, this value can be taken for illustrating the difference between an effective medium treatment and a three dimensional treatment. The main results will be then assumed to be the same for a the system with appropriate slab thickness.

As an illustration, let us consider a corrugated polyethylene-vacuum-water system with slabs thickness of 10 nm. From the individual scattering matrices S_1 and S_2 of each components of the system (Fig. 7.1) and the scattering matrix of vacuum S_v, the Lifshitz-van der Waals potential energy is obtained from Eq. (7.10) (the derivation is presented in Chapter 5) :

$$U^{LW}(L) = \frac{\hbar}{2\pi} \int \frac{d^2 k_{//}}{(2\pi)^2} \int_0^\infty d\xi \ln \left[\det \left(1 - S_1^{+-}(i\xi, \overrightarrow{k}_{//}) S_v^{--}(i\xi, \overrightarrow{k}_{//}) S_2^{-+}(i\xi, \overrightarrow{k}_{//}) S_v^{++}(i\xi, \overrightarrow{k}_{//}) \right) \right], \tag{7.10}$$

where the scattering matrices are calculated using the RCWA method. For computation, cones are approximated by a stack of cylinders of various radii (Fig. 7.3). The wavelength range is the same as the one used above. In the case of a periodic three dimensional patterned surface, an additional convergence study is required for determining the number of reciprocal lattice vectors needed for properly describe the scattering properties of the system. Therefore, a joint convergence study determining the number of photon wave vectors $N_{\overrightarrow{k}_{//}}$ and the number of reciprocal lattice vectors $N_{\overrightarrow{g}}$ required for the calculation needs to be performed. Such a convergence study is presented in Fig. 7.13.

The Lifshitz-van der Waals potential energy is calculated for a given separation distance $L = 5\ nm$ and a given cone height $h = 10\ nm$. The potential energy is evaluated for several values of $N_{\overrightarrow{k}_{//}}$ and $N_{\overrightarrow{g}}$ and its value calculated by the effective medium approach is also displayed for comparison. From Fig. 7.13, the Lifshitz-van der Waals potential energy converges for $N_{\overrightarrow{k}_{//}} = 49$ and $N_{\overrightarrow{g}} = 3 \times 3$ which means that only two diffracting orders (-1,1)[5] and the specular order are sufficient for describing the interactions. Such result is not surprising since the very weak coupling between diffracting orders (see Section 7.2) does not allow a significant transfer of energy from the specular order to the diffracting orders. Moreover, for the short

[5] A number $N_{\overrightarrow{g}} = 3 \times 3$ of reciprocal lattice vectors means that diffracting orders $\{-1, 0\ (specular), 1\}$ in both X and Y directions are involved in the numerical calculation.

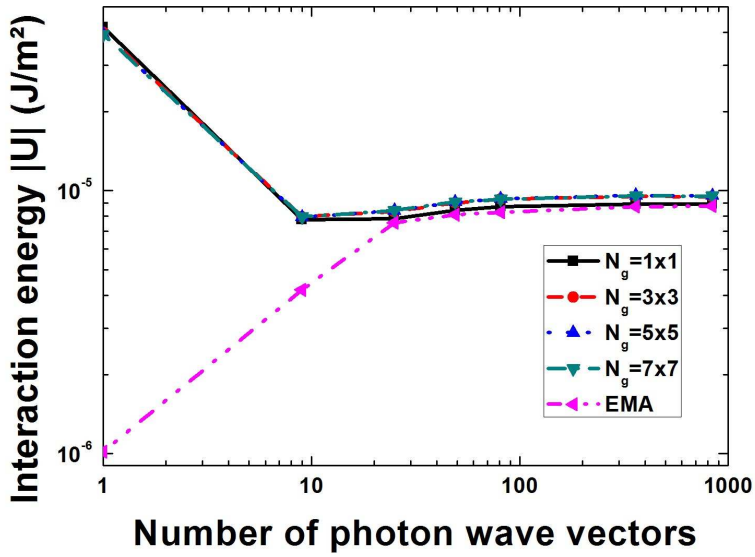

Figure 7.13: Convergence curve of the Lifshitz-van der Waals potential energy of the corrugated polyethylene-vacuum-water system for $L = 5\ nm$ and $h = 10\ nm$. The optimal number of photon wave vectors is evaluated for different numbers $N_{\overrightarrow{g}}$ of reciprocal lattice vectors.

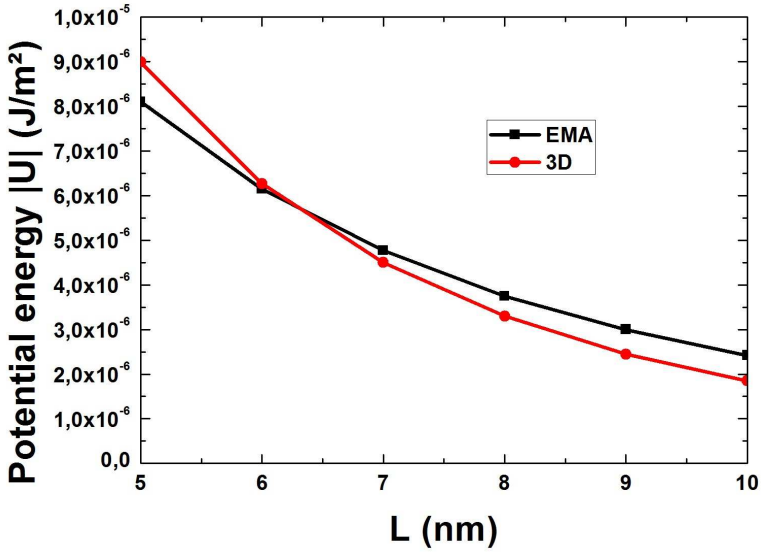

Figure 7.14: Comparison of the potential energy between the effective medium approach and the three dimensional treatment for a given separation distance $L = 5\ nm$ and a given cone height $h = 50\ nm$.

separation distances considered (see hereafter), the near field is dominant compared to the far field. Therefore, the high number of reciprocal lattice vectors required for the far field description ($N_{\overrightarrow{g}} = 9{\times}9$) is no more necessary in the near field case. Increasing the number of reciprocal lattice vectors will only slightly modify the Lifshitz-van der Waals potential energy, as shown on Fig. 7.8. The comparison between the effective medium approach (recalculated for 10 nm slab thicknesses) and the three dimensional treatment is displayed on Fig. 7.14. It appears very weak differences between both treatments (maximum relative error of 8 %), as

expected.

Chapter 8

Lifshitz-van der Waals interactions and superhydrophobicity

Nanostructures are commonly used for developing superhydrophobic surfaces. However, available wetting theoretical models ignore the effect of vacuum photon-mode alteration on Lifshitz-van der Waals forces and thus on hydrophobicity. In this chapter, it is shown theoretically that superhydrophibicity of nanostructured surfaces is dramatically enhanced by Lifshitz-van der Waals potential energy tuning. As a case study, static contact angles of a water droplet above a polyethylene nanostructured surface are obtained from the interaction potential energy calculated as a function of the droplet-surface separation distance. This new approach could pave the way for the design of novel superhydrophobic coatings.

8.1 Calculation of the water contact angle

While superhydrophobicity on structured surfaces is a topic of high interest [131][150], and wetting phenomena are known to be related to Lifshitz-van der Waals forces [151][152][16], the influence of surface nanocorrugations on Lifshitz-van der Waals forces has not been considered in wetting theoretical models as of yet [6][7][8]. For this purpose, let us consider the same two-body system than the one presented in the previous chapter involving the interactions between a cones patterned polyethylene and a droplet of water through vacuum (Fig. 7.1). The associated. Lifshitz-van der Waals potential energy $U^{LW}(L)$ is displayed on Fig. 7.10b for various cones heights. In order to probe the influence the Lifshitz-van der Waals potential energy tuning on the wettability of polyethylene, the static contact angle θ of the water droplet on the corrugated polyethylene surface can be evaluated from the potential energy for various cones height. Indeed, in the case of an apolar polymer such as polyethylene, the Yound-Dupré equation[1] [1] is able to predict the static contact angle of a water droplet on a surface such as :

$$\cos\theta = -1 + \frac{\left|U^{LW}(L_0)\right|}{\gamma_l}, \tag{8.1}$$

[1] See Chapter 2

where γ_l is the liquid surface tension, which for water is equal to 72.5 mN/m [18] and L_0 is the equilibrium separation distance [1] between the water droplet and the surface. This distance is substantially smaller than the center-to-center interatomic or intermolecular distance σ ($L_0 \approx \sigma/2.5$) [18]. However, it is remarkable that this sort of "'universal constant"' yields values for surface energies in such good agreement with those measured[2], for a large range of materials. The L_0 value, originally defined for a flat surface with planarly aligned atoms [18], is assumed hereafter to remain the same when the surface is corrugated. Actually, the lack of data on the equilibrium separation distance values for corrugated surfaces leaves us no choice but to use the value for flat surfaces of identical material. This approximation is strong since atoms are not planarly aligned anymore while dealing with corrugated surfaces. In a sense, a "local" equilibrium separation distance should be defined for each group of atoms of the patterned surface, rendering the problem clearly much more complex. However, this bold hypothesis does not affect the main results of the model as it will be demonstrated further (see Section 8.4).

8.2 Achievement of the superhydrophobicity

The equilibrium separation distance between water and flat polyethylene surface was calculated to be $L_0 = 0.145$ nm [16]. Although this value is reported for two flat polyethylene surfaces facing each other, it remains essentially unchanged while considering the present polyethylene-water system, as shown in [16]. Due to numerical stability issues, potential energy at $L = L_0$ is extrapolated from the data presented in Fig. 7.10b, by fitting the data to the energy values calculated for $L \leq 10$ nm [106] using the simplified form of the Lifshitz-van der Waals energy[3], with the calculated Hamaker constant A_h as fitting parameter :

$$U^{LW}(L) = -\frac{A_h}{12\pi L^2}. \tag{8.2}$$

The procedure is illustrated on Fig. 8.1 for cones height $h = 10$ nm. As shown on Fig. 8.1, the fit is not perfect ($R^2 = 0.87$) due to the fact that Eq. (8.2) is usually defined for homogeneous flat surface. In the case of multilayered surface, additional terms should be taken into account [153]. However, to qualitatively describe the influence of the tuning of the Lifshitz-van der Waals interactions on the static contact angle, Eq. (8.2) is sufficient.

The fitted Hamaker constant for each height h is shown in Fig. 8.2a. Using Eq. (8.1) and Eq. (8.2) with $L = L_0$, the expected value of the contact angle of a water droplet on a flat ($h = 0$ nm) polyethylene surface is found: $\theta = 102°$ [18] (Fig. 8.1b). The flat polyethylene is therefore hydrophobic. For a corrugated surface, the contact angle and the Hamaker constant of the system are modified with respect to a flat surface: the Hamaker constant decreases (Fig. 8.1a) while the contact angle increases (Fig. 8.1b) as the cone height increases. Superhydrophobicity ($\theta \geq 150°$) is achieved for $h > 20$ nm in the present case. **The tuning of the optical response of the polyethylene surface via its nanostructuration directly affects its wettability**

[2] $\gamma \approx \frac{A_h}{24\pi L_0^2}$

[3] See Chapter 2.

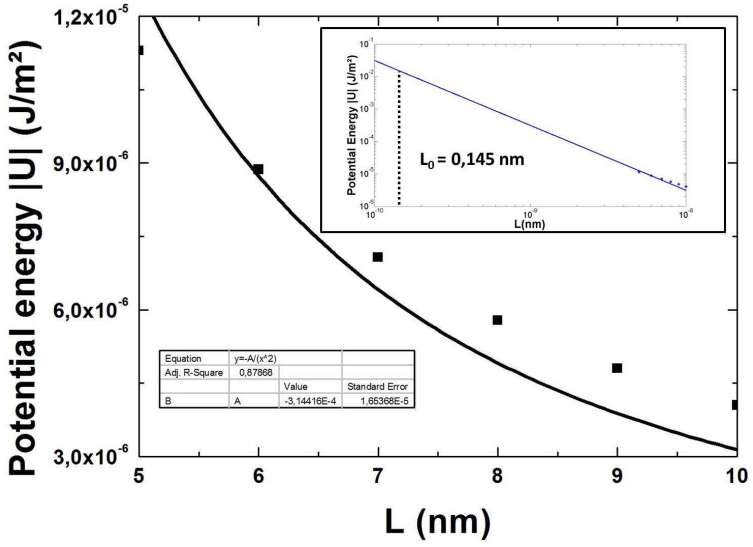

Figure 8.1: Fit of the computed Lifshitz-van der Waals potential energy related to the interaction of 100 nm cones patterned polyethylene surface with a droplet of water through vacuum. The fit is realized with Eq. (8.2). Inset shows the fitted potential energy at the equilibrium separation distance (note the logarithmic scale).

[91].

Our calculation predicts a contact angle (not shown on Fig. 8.2b) of 173° for $h = 1$ μm (aspect ratio $h/a_0 = 100$) and of 175° for $h = 10\mu$m (aspect ratio $h/a_0 = 1000$). Ultimately, it can be expected a contact angle approaching 180° for a very high aspect ratio of cones, *i.e.* $h/a_0 >> 1000$. First of all, it should be stressed that such high aspect ratio patterned surfaces ($h/a_0 > 10$) would be extremely complicated to fabricate. Therefore, there considerations are here purely theoretical. According to Eq. (8.1), a contact angle of 180° corresponds to zero potential energy. The asymptotic increase of the contact angle towards 180° as h increases results from the fact that, beyond a height of 100 nm[4] (maximum value displayed on Fig. 8.1b), the potential energy U decreases more slowly with h. Indeed, the reflection coefficient $|R_1|^2$(Fig. 7.10a) barely decreases at wavelengths $\lambda_p > 1000$ nm when h increases. In addition, the related vacuum photon-modes angular frequencies $\omega_p = 2\pi c/\lambda_p$ represent small energy values $\frac{1}{2}\hbar\omega_p(L)$ in the contributions to the potential energy U, which therefore varies more slowly when h increases above 100 nm.

Finally, note that for comparing the influence of the effective medium approach and the three dimensional treatment on the calculation of the static water contact angle, a 10 nm thick slab must be used (see Chapter 7). In this case, the static water contact angle can be calculated from both models. Results gives the same values of the contact angle (differences less than 2 %) and the same trend than the one presented above for both approaches, validating the use of the effective medium approach.

[4]The aspect ratio of the patterned surface would be equal to 10 in this case. Since such value is much more realistic in terms of fabrication but still high, the 100 nm cone height is set as the upper limit in the calculation.

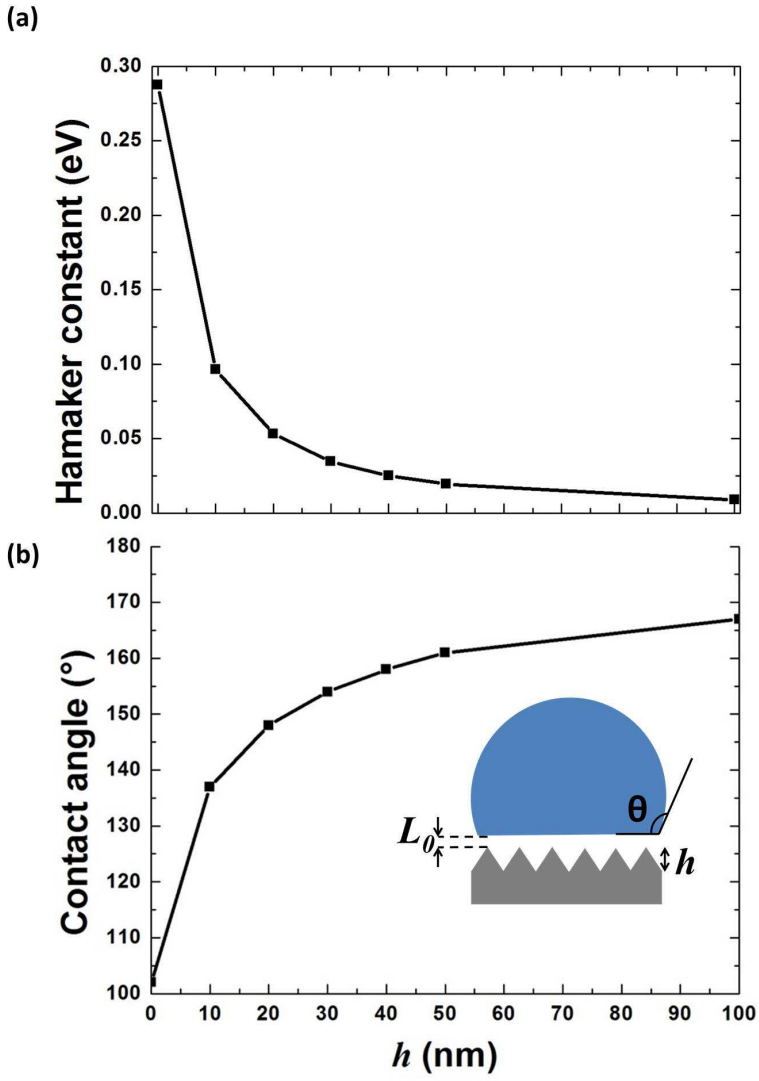

Figure 8.2: (a) Evolution of the Hamaker constant as function of the height h of cones. (b) Evolution of the contact angle of a water droplet on nanostructured polyethylene as function of the height h of cones.

8.3 The case of cylinders

In comparison to the antireflective cones array, using cylinders (same hexagonal lattice parameter equal to 10 nm and radius of 2.5 nm) cannot provide efficient antireflection character to the surface since there is no gradient of the effective permittivity: the reflection does not significantly decrease as the cylinder height increases (Fig. 8.3a). Therefore the Lifshitz-van der Waals potential energy, although it is higher than for a flat surface, does not evolve for cones height higher than 10 nm (Fig. 8.3b). As a consequence, the contact angle on this corrugated surface saturates quickly with the cylinder height (see inset table in Fig. 8.3b) and superhydrophobicity is never achieved (saturated value is about 140°).

It is noteworthy that cylinders do not fully satisfy the conditions mentioned above for using the effective medium approach. Indeed, the effective medium description of cylinders suffer

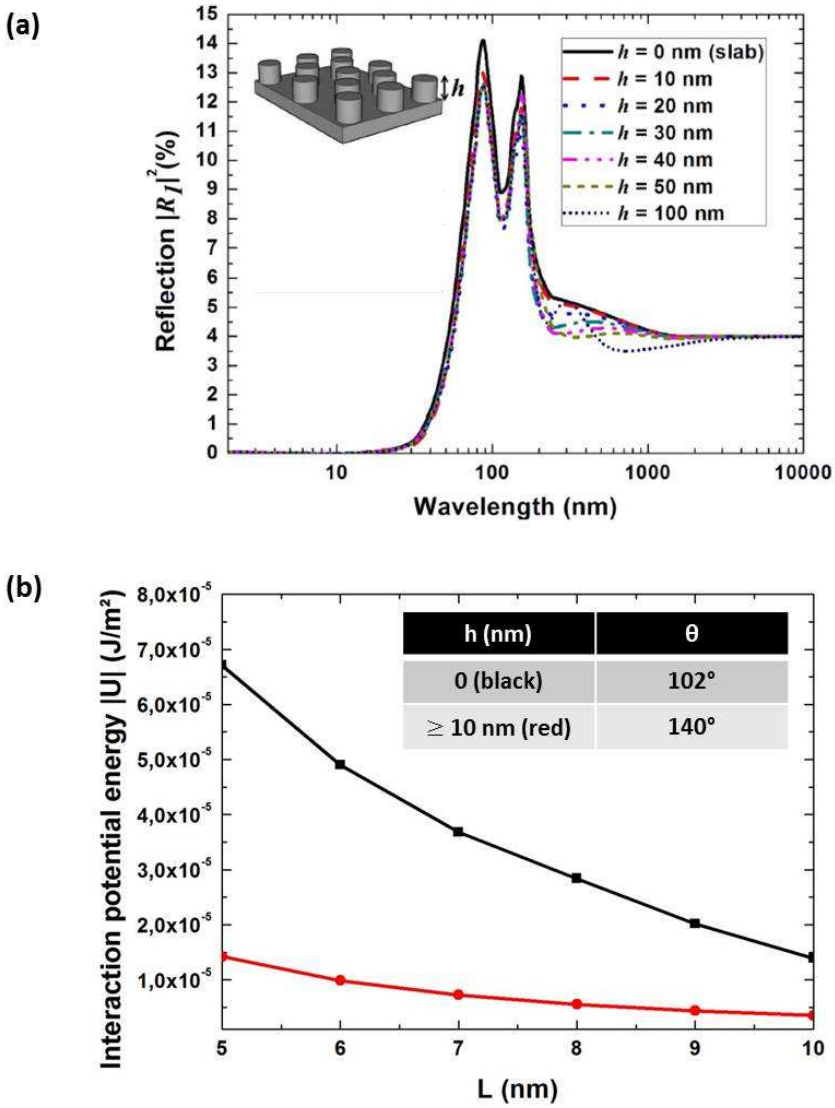

Figure 8.3: (a). Evolution of the reflectance with the height of nanocylinders covering the polyethylene slab. (b). Evolution of the potential energy with the height of nanocylinders covering the polyethylene slab. Inset (table): Contact angle of a water droplet on nanostructured polyethylene with cylinders heights h higher than 10 nm, compared with contact angle on a flat surface.

from the same drawback than the effective medium description cones for describing the far field (see Chapter 7). Moreover, the description of the near field within an effective treatment is less appropriate than for cones. The absence of very steep features does not allow to completely elude the coupling between diffracting modes. Indeed, as displayed on Fig. 7.7, the coupling intensity between diffracting modes is two orders of magnitude higher, and therefore is a less negligible, than for cones. As a consequence, an effective medium approach is less suitable in the case of cylinders. This result is confirmed by the simulated diffracted field patterns which originate from oscillating dipoles inserted inside the cavity (Fig. 8.4). Compared to the cones case, the intensity of the diffracted fields are more distinguishable, highlighting the coupling

phenomena mentioned above. Therefore, although the difference in terms of potential energy between the effective medium and the three dimensional treatment is weak (see Appendix B), the three dimensional treatment was chosen. The required convergence parameters of the problem are $N_{\overrightarrow{k}_{//}} = 49$ and $N_{\overrightarrow{g}} = 3 \times 3$. The associated convergence studies are presented in Appendix B.

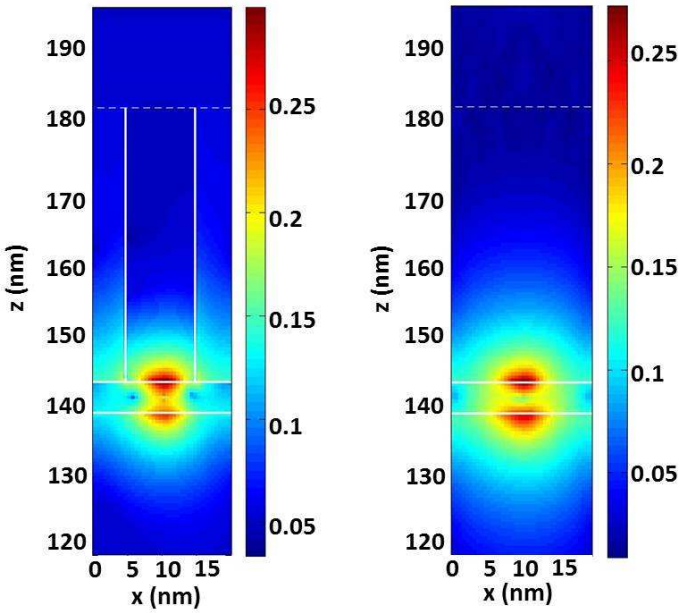

Figure 8.4: Maps of the normalized intensity of diffracted field for in the three dimensional cylinders structure (left panel) and its effective medium description (right panel). The maps are calculates at a wavelength of 155 nm and a for cone height of 40 nm.

8.4 The equilibrium separation distance

Considering a rough surface instead of a flat surface, it seems reasonable that different Lifshitz-van der Waals potential energies correspond to different equilibrium separation distances and thus contact angles. However, it is claimed that a change in the L_0 value (to account for rough instead of flat surface) does not modify the main result of this study: the reduction of Lifshitz-van der Waals poential energy due to nanoscopic corrugations increases the water contact angle. For justifying such a claim, let us consider a Lennard-Jones-like potential as effective interface potential of the rough surface-liquid system (Fig. 8.5). Such a potential has two contributions: a short-range repulsive interaction term related to Pauli exclusion principle and an attractive term related to Lifshitz-van der Waals interactions which is used in the calculation of the water contact angle. The equilibrium separation distance L_0 is the distance that corresponds to the potential minimum.

Unfortunately, it is not possible to predict theoretically the behavior of the short-range interaction term for a corrugated polyethylene surface due to the lack of direct physical access. On one hand, since the short-range repulsive interactions are determined solely by the topmost

atomic layer, they can be regarded to be the same for any corrugation depths (heights of cones or cylinders). On the other hand, the Lifshitz-van der Waals potential energy decreases with the cones height and partially with the cylinders height (Fig. 7.10b and 8.3b). Therefore, for constant short-range interactions, the equilibrium separation distance L_0 increases with height of corrugations h. An illustration of this subtle effect is presented in Fig. 8.5. On Fig. 8.5,

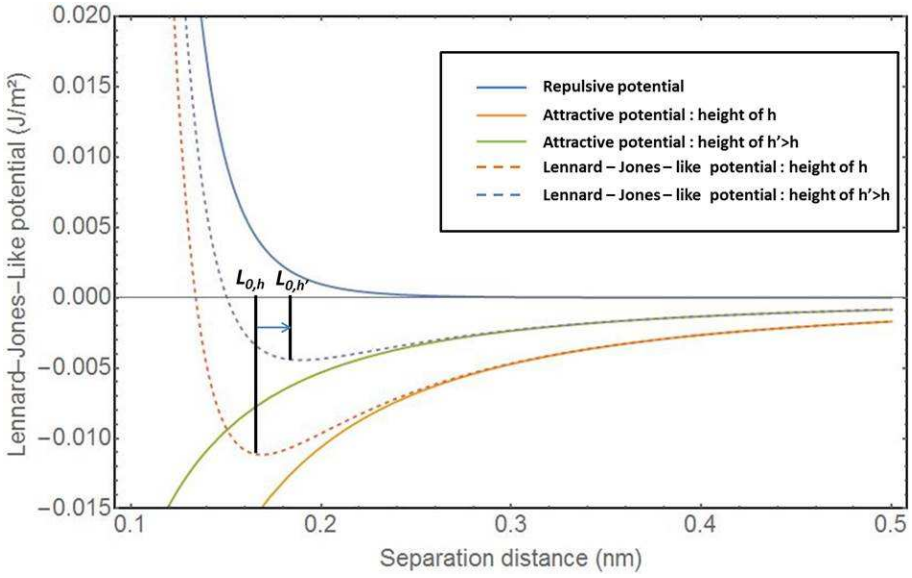

Figure 8.5: Qualitative picture of the evolution of the equilibrium separation distance L_0 while increasing the corrugation height from h to h'.

the short-range interaction term is kept constant with respect to h (blue solid curve) while the Lifshitz-van der Waals interaction term decreases with the increase of the corrugations height from h (orange solid curve) to $h^{'} > h$ (green solid curve). As a consequence, the Lennard-Jones-like potential associated with corrugations height h (orange dashed curve) gives a smaller value of the equilibrium separation distance than the one associated with corrugations height $h^{'} > h$ (blue dashed curve).

According to Eq. (8.1) and Eq. (8.2), this subtle effect, *i.e.* increase of the equilibrium separation distance and decrease of the Hamaker constant, leads to an increase of the water contact angle when the corrugations height increases. In consequence, the main effect of nanocorrugation on wettability described above is not only preserved but actually reinforced.

Of course, a refined model should explicitly take into account the short-range repulsive term, which should be computed in order to determine the equilibrium separation distance for a rough surface. However, the transition from a flat surface to a rough surface at the nanometer scale considered in our study, should increase the water contact angle according to experimental data [154] and to the theoretical considerations mentioned above. The determination of the short-range repulsive term is not a trivial task, as it should involve molecular dynamics computations for instance. This endeavor is beyond the scope of the present thesis since, as previously explained, such a refinement will not change the main conclusions of this study.

8.5 Possible experimental validations

The fabrication of the patterned surfaces involved in the present study appears as tricky since they require very specific size and shape, sub-10 nm periodically cones. Note that perfect regularity of the periodic pattern is not strictly need as it is well known that, *e.g.*, antireflection property can be achieved with random structures. Dimension and shape of the corrugations are therefore the critical parameters. In order to reach such dimensions and shapes, exotic fabrication techniques are required. Although we have performed the first steps towards the fabrication of such structures, we did not manage to fabricate a prototype of the patterned polyethylene so far. However, reports in literature seem to support our numerical result. A

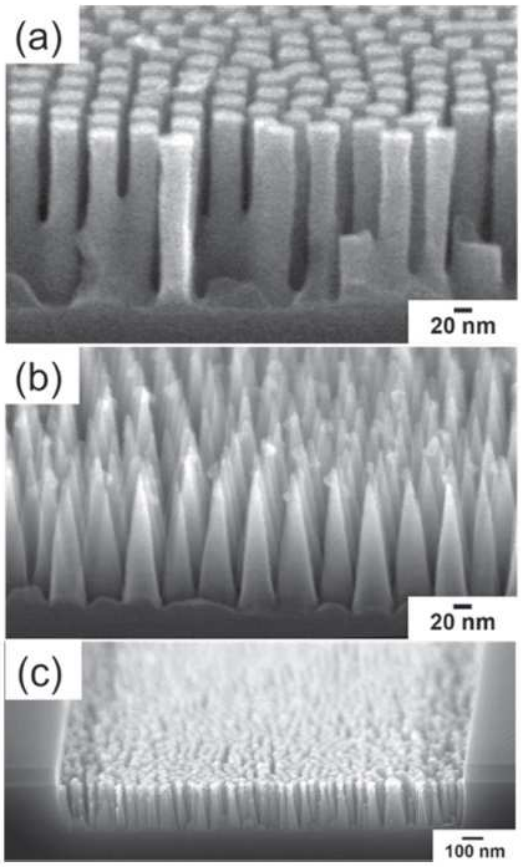

Figure 8.6: a) Side-view SEM image of a silicon surface textured with cylindrical pillars. b) Side-view SEM image of a silicon surface textured with nanocones. c) Side-view SEM image of nanocone surface formed in a selected substrate area [155].

team from the Brookhaven National Laboratory combined a block-copolymer self assembly technique with plasma based etching in order to generate nanostructured superhydrophobic surfaces over arbitrarily large areas (Fig. 8.6) [155]. They fabricated cones and cylinders array the dimensions of which are presented in Fig. 8.7. Their dimensions can be roughly assimilated to the dimensions of our computed cones and cylinders.

The as-fabricated patterned surface was made of silicon and was rendered hydrophobic by passivating it with a 2.5 nm thick octadecyltrichlorosilane (OTS), an apolar component

the surface energy of which is close to the one of polyethylene [18]. The thickness of such a

Surface Texture	Spacing (±1 nm) [nm]	Feature height (±5 nm) [nm]	θ_{adv} (±2°) [°]	$\Delta\theta$ (±3°) [°]
Flat	NA	NA	112	6
52 nm spaced pillars	52	180	150	30
30 nm spaced pillars	30	75	137	27
52 nm spaced cones 1	52	75	165	5
52 nm spaced cones 2	52	180	165	6
30 nm spaced cones	30	95	162	7

Figure 8.7: Average feature spacing, feature height, advancing water contact angle, and hysteresis of nanopatterned surfaces described in the reference [155].

monolayer is sufficient to render the patterned surface completely apolar. Therefore, since the dimensions of the nanostructures (subwavelength dimensions) as well as their chemical nature (apolar component) are closely similar to those numerically predicted in the previous sections, the measured contact angles (advanced contact angle) presented in Fig. 8.7 can be compared to those calculated above. By comparing both experimental et numerical results, it appears that the water contact angles are rougly similar, supporting the validity of the presented numerical model.

Chapter 9

The repulsive Lifshitz-van der Waals interactions

In previous chapters, the bridge between quantum vacuum photon modes and properties of patterned surfaces was established on solid theoretical grounds. Based on these foundations, hereafter, the manipulation of quantum vacuum photon modes in a nanostructured cavity is theoretically shown to be able to change the Lifshitz-van der Waals forces from attractive to repulsive regime. Since this concept relies on surface nanopatterning instead of chemical composition changes, it drastically relaxes the usual conditions for achieving repulsive Lifshitz-van der Waals forces. As a case study, the potential interaction energy between a nanopatterned polyethylene slab and a flat polyethylene slab with water as the intervening medium, *i.e.* the medium between both slabs, is calculated. Extremely small corrugation heights (<10 nm) are shown to be able to change the Lifshitz-van der Waals force from attractive to repulsive, the interaction strength being controlled by the corrugation height.

9.1 Traditional approach of repulsive Lifshitz-van der Waals interactions

Over the last decades, the Lifshitz - van der Waals approach of interfacial interactions in macroscopic systems has been widely investigated, both theoretically and experimentally [60][84][100][61]. Although usually attractive, the interaction potential energy may become repulsive if particular conditions are satisfied [62]. Let us first consider a body (1) interacting with a body (2) *via* an intervening medium (3) (Fig. 7.2). Let us also consider, for the moment, that each element of this macroscopic system has a planar geometry (for now body (2) is treated as a flat homogeneous slab) and is characterized by a dielectric function $\varepsilon(\mathrm{i}\xi)$, where $\mathrm{i}\xi$ is the imaginary angular frequency. It is well established that repulsive Lifshitz-van der Waals interactions between the two bodies can take place if the following condition is satisfied [62]:

$$\varepsilon_1(i\xi) < \varepsilon_3(i\xi) < \varepsilon_2(i\xi) \tag{9.1}$$

where ε_i is the dielectric function of the ith component of the system. As a matter of fact, Eq. (9.1) cannot be satisfied if the intervening medium is vacuum. Therefore, a liquid or a gas is needed to satisfy Eq. (9.1) for given slab materials [62]. Moreover, in practice, Eq. (9.1) imposes tight constraints on the choice of both the materials and the intervening medium, which makes challenging the experimental observation of repulsive Lifshitz-van der Waals interactions [84][156].

9.2 Negative Hamaker constant

Hereafter, an original approach is introduced to modify Lifshitz-van der Waals interactions in a very different perspective, beyond the constraint set by Eq. (9.1). As it was shown in previous chapters, at short separation distances ($L \leq 10$ nm), the Lifshitz-van der Waals potential energy is well approximated by [109]:

$$U^{LW}(L) = -\frac{A_{132}}{12\pi L^2} \tag{9.2}$$

where A_{132} is the effective Hamaker constant of the system which can be deduced from the numerically computed energy, *i.e.* Eq. (7.10) .

In case the intervening medium is vacuum, Eq. (7.10) appears to be efficient since it reproduces well experimental results [18]. In this case, using Eqs. (7.8) and (9.1), it is possible to retrieve the Hamaker constant A_{12} of the system ($A_{12} \equiv A_{132}$, where (3) is omitted when the intervening medium is vacuum). Using the same procedure, it is also possible to retrieve the Hamaker constant A_{11} of the flat surface. The effective Hamaker constant A_{22} of the patterned surface, on the other hand, can be deduced indirectly from the well-known relation [18] $A_{12} = \sqrt{A_{11}}\sqrt{A_{22}}$ by using values of A_{12} and A_{11} calculated from Eqs. (7.8) and (9.1).

For numerical convenience [157][158], instead of computing directly A_{132} *via* Eq. (7.8) in order to obtain the interaction potential energy, the effective Hamaker constant of the system (hereafter, (3) stands for fluid) was computed from the well-known relation [18][157][158]:

$$A_{132} = (\sqrt{A_{11}} - \sqrt{A_{33}})(\sqrt{A_{22}} - \sqrt{A_{33}}) \tag{9.3}$$

where A_{ii} are the Hamaker constants of the corresponding media which are obtained from the above described procedure. Repulsive interaction potential energy is reached when A_{132} is negative, *cf.* Eq. (9.1) . Therefore, according to Eq. (9.2) , such a condition is fulfilled when :

$$A_{22} < A_{33} < A_{11}. \tag{9.4}$$

The condition imposed by Eq. (9.3) goes beyond the constraint set by Eq. (9.1) . Indeed, when considering a nanopatterned surface, as in the present case, Eq. (9.1) can not be used since dielectric functions are those of flat materials. On the other hand, Eq. (9.3) allows to bypass this problem since the effective Hamaker constant of the nanopatterned surface can be calculated by the above described procedure. Therefore, Eq. (9.3) has a more general application since it can be used simultaneously for both flat and nanopatterned surfaces.

9.3 Modeling and simulation details

Let us now develop the case of a practical two-body system consisting of two polyethylene slabs facing each other and separated by a L distance. In order to fulfill Eq. (9.3), water (medium 3) was chosen as intervening medium. It must be pointed out that such a configuration does not match Eq. (9.1) since the interacting bodies are made of the same material. The first slab (slab 1) has a flat (planar) surface while the second one (slab 2) is nanostructured with cones of height h arranged on a hexagonal lattice with a lattice period chosen to be $a_0 = 10$ nm (Fig. 7.2). A fixed cone base radius of $r = 5$ nm was chosen and the cone height h was varied (ranging from 10 to 100 nm) in order to alter the optical properties of the surface. Indeed, such a geometry is known to improve the antireflection behavior of the surface which in turns alters the vacuum photon modes of the system. This patterned surface is the same as the one used in the previous chapter and is approximated by an effective medium approach, as fully discussed above. Moreover, since the polyethylene surface is hydrophobic [18], a Cassie state [6] can be assumed between water and the corrugated polyethylene surface[1]. As a consequence, the void space between cones is filled by air and water is localized above the top of the cones only.

9.4 Numerical results

As explained in paragraph 7.2, the use of a fluid as intervening medium led no choice but to compute individual Hamaker constants of each component of the system in a first step. From previous results[2], the effective Hamaker constant A_{22} of the corrugated polyethylene slab is calculated using Eq. (7.8) and Eq. (9.1) for various cones heights (Fig. 9.1).

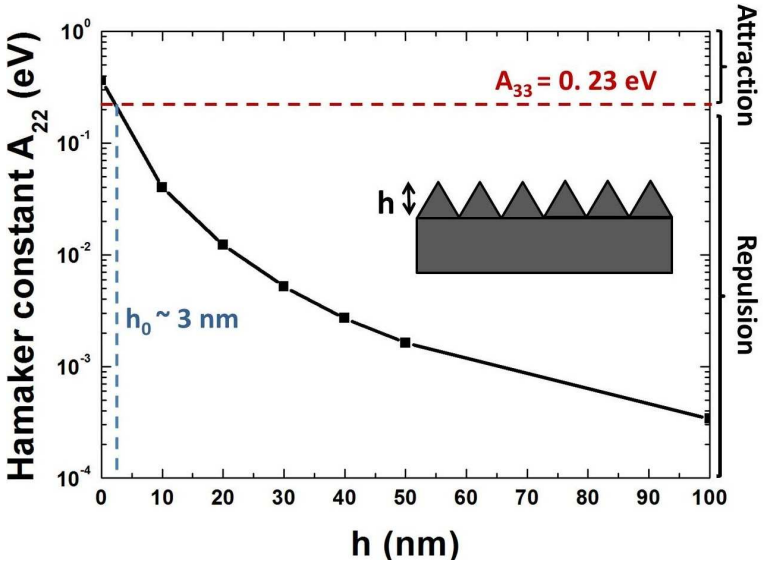

Figure 9.1: Hamaker constant A_{22} of nanopatterned polyethylene slab (see inset) as a function of cones height h.

[1] See Chapter 2.
[2] See Chapter 8.

Knowing the Hamaker constant A_{11} of flat PE surface ($A_{11} = 0.36$ eV) [18] and the Hamaker constant A_{33} of water ($A_{33} = 0.23$ eV) [18], the Hamaker constant A_{132} of the whole system is calculated from Eq. 9.2, as a function of the cones height (Fig. 9.2). Strong decrease of the Hamaker constant A_{132} with increasing cones height is observed, going from positive to negative values (Fig. 9.2). Here, the zero-crossing point for A_{132} takes place for $h_0 \approx 3$ nm. This critical

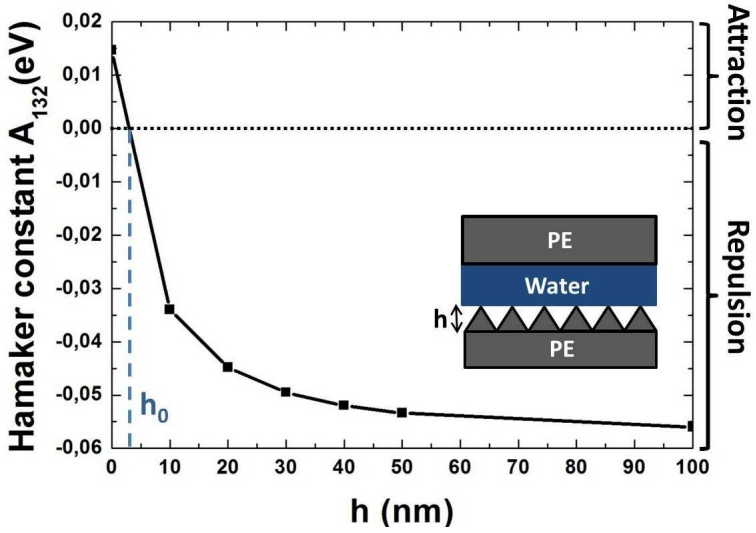

Figure 9.2: Hamaker constant A_{132} of flat polyethylene/patterned polyethylene system immersed in water (schematic view in the inset) as a function of cones height h.

point is reached when $A_{22} = A_{33}$ (horizontal red-dotted line, Fig. 9.1), in accordance with the fact that repulsive interaction is achieved only if Eq. (9.3) is satisfied. Therefore, the interaction potential energy becomes positive, *i.e.* repulsive force (Fig. 9.3), for $h > h_0$ as soon as the Hamaker constant A_{132} of the system becomes negative [159].

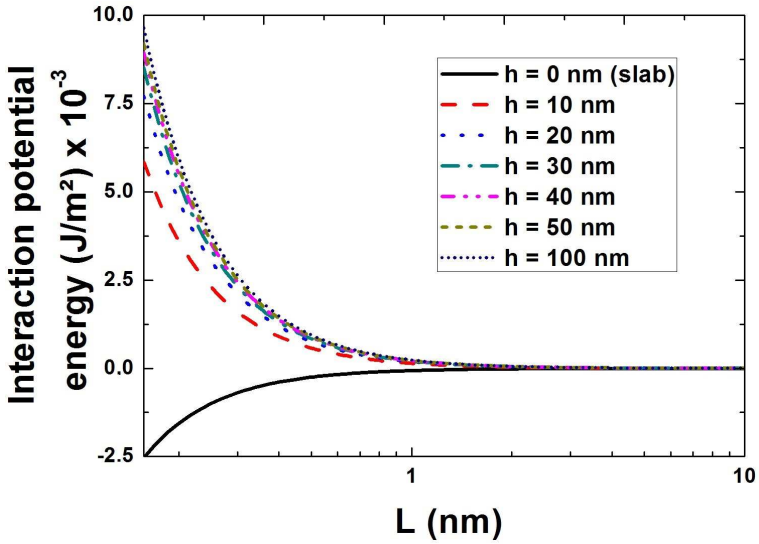

Figure 9.3: Interaction potential energy between PE slabs as a function of cones height.

It is noteworthy that, due to the small zero-crossing point value h_0, it could be experimentally

difficult to achieve a progressive transition from attractive to repulsive force while increasing the cones height. Thus, observation of this progressive transition would require higher h_0 value which could be achieved by using flat materials with Hamaker constants A_{22} (h =0 nm) higher than the Hamaker constant A_{33} of the intervening medium (by at least one order of magnitude, see Fig. 9.1). Furthermore, owning to the Cassie state regime of the present model, such materials are difficult to find [18]. Consequently, the transition from attractive to repulsive regimes cannot be easily observed as well as significantly modified (*i.e.* h_0 value stays in the same range for most of the materials).

9.5 The electrostatic double layer

The impact of the choice of water as the intervening medium has to be examined. Indeed, as a polar liquid, water induces an electrostatic double layer at both surfaces facing each other, giving rise to an additional electrostatic repulsive force between them which, in experiments, could screen the Lifshitz-van der Waals repulsive force treated here. However, while considering the Cassie state regime, the electrostatic double layer is located only on the top of the cones which become steeper while increasing the cones height. As a consequence, the electrostatic double layer associated to the steep nanocorrugated polyethylene surface becomes extremely small, leading to a dramatic decrease of the electrostatic repulsive interaction. Indeed, the relative contribution of electrostatic forces to interfacial interaction in the case of polyethylene slabs facing each other at very small separation distance (around 10 nm) needs to be examined. Let us first consider two flat surfaces facing each other and separated by a distance L with a liquid as intervening medium. The electrostatic potential energy associated to the electrostatic

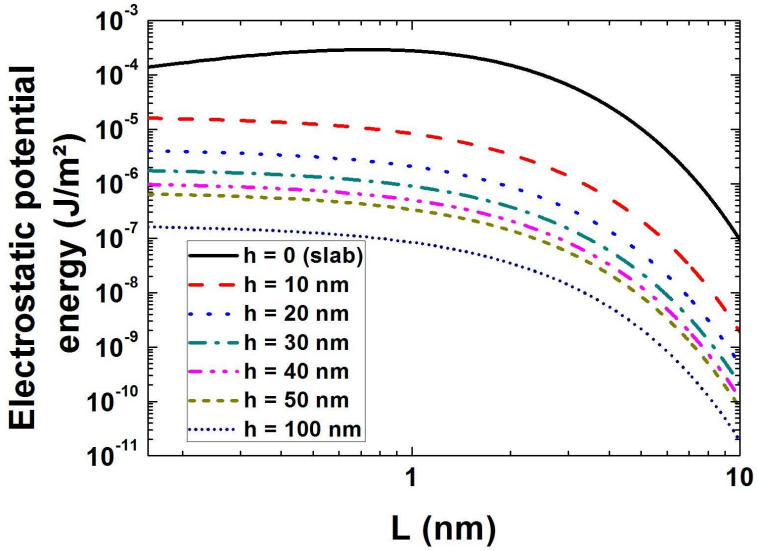

Figure 9.4: Electrostatic potential energy between PE slabs as a function of cones height. Note the orders of magnitude on the Y-axis in comparison with Fig. 9.3.

double layer formed at both surfaces is given by [18]:

$$W(L) = \varepsilon_r \varepsilon_0 \kappa \left[2\psi_1 \psi_2 e^{-\kappa L} - (\psi_1^2 + \psi_2^2) e^{-2\kappa L} \right] \tag{9.5}$$

where ε_r is the static permittivity (dielectric constant) of the liquid, ε_0 is the vacuum permittivity, κ is the inverse of the Debye length of the liquid and ψ_i is the surface potential of the i^{th}surface.

Replacing now one of the two surfaces by a periodically nanostructured surface, here an array of cones, and using the Derjaguin approximation [77], the electrostatic potential energy is given by (see Appendix C for calculation):

$$W(L) = 2\pi \varepsilon_r \varepsilon_0 \tan^2(\alpha) e^{-\kappa L} \times \left[2\psi_1 \psi_2 - (1/4)(\psi_1^2 + \psi_2^2) e^{-\kappa L} \right] / \kappa S \tag{9.6}$$

where α is the opening angle of the cone and $S = a_0^2 \sqrt{3}/2$. It is noteworthy that the Derjaguin approximation is valid only if the Debye length of the liquid is smaller than the lattice period a_0 of the structured surface so that the electrostatic potential energy is not affected by coupling effects between cones.

In the case study presented in this thesis, the surface potential of both polyethylene surfaces is equal to - 30mV [18], the static permittivity of water is equal to 78.2 J $m^{-1}V^{-2}$ [18] and the Debye length of water is equal to 1.5 nm [18] (the Debye length of groundwater is used for more realistic considerations). Note that the small value of the Debye length allows one to use Eq. (9.6) since the correlation length (*i.e.* cones interdistance) is one order of magnitude larger. The electrostatic potential energy for various cones heights is shown at Fig 9.1. Comparing the magnitude of the electrostatic potential energy (Fig. 9.5) and that of the Lifshitz-van der Waals potential energy (Fig. 9.3) for same cones height, the electrostatic potential energy is found to be negligible compared to the Lifshitz-van der Waals potential energy.

Chapter 10

Toward experimental validation

This last chapter presents the experimental strategy we have selected for fabricating the cones-patterned surfaces considered in this work. A block-copolymer-based thin-film patterning method is chosen in order to create large-area textured surfaces with sub-10 nm features. This method, inspired by the works of Checco *et al.* [155], is divided into five main steps, each one described hereafter. Although, at this stage, a prototype of such surfaces has not been obtained yet, the preliminary results regarding the first fabrication steps are presented. These results were obtained in the framework of a collaboration I initiated with four universities : the University of Bordeaux (Laboratoire de Chimie des Polymères Organiques), the Catholic University of Louvain (Institute of Information and Communication Technologies, Electronics and Applied Mathematics), the Ecole Centrale de Lyon (Institute of Nanotechology) and the University of Namur (Physique de la Matière et du Rayonnement)

As mentioned above, the selected experimental method is a block-copolymer-based thin film patterning [160][155][161]. Already briefly presented in Section 8.5, the method consists in combining block-copolymer self assembly with plasma-based etching. Using intermediate steps of Atomic Layer Deposition (ALD) cycles and oxygen plasma etching, this method allows to generate nanostructured surfaces over arbitrarily large areas. While the main steps are only briefly described hereafter, specific details can be found elsewhere [160][155][161].

10.1 Block copolymer spin-casting

The process begins by spin-casting polystyrene- *block* -poly(methyl methacrylate) (PS-b-PMMA) block-copolymer thin film onto a flat silicon surface. In this case, PS acts as a matrix in which are embedded cylindrical PMMA domains locally arranged in a close-packed hexagonal lattice, as displayed on the Atomic Force Microscope (AFM) images in Fig. 10.1. Moreover, the self-assembled domain size scales with the copolymer molecular weight. Here, on average, 23 nm pitch (Fig. 10.1a) and 32 nm pitch (Fig. 10.1b) PS-b-PMMA block copolymer hexagonal patterns were generated from different molecular-weight materials. Note that a specific pretreatment of the silicon substrate allows the PMMA cylindrical domains to orient perpendicularly [155]. This first step of the experimental procedure was realized at the Laboratoire de Chimie

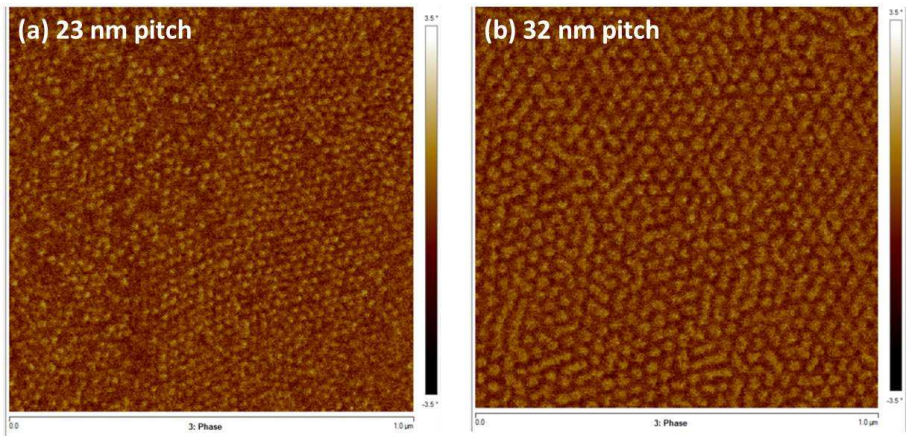

Figure 10.1: (a) AFM image of the 23 nm pitch cylindrical phase PS- b -PMMA block-copolymer film. (b) AFM image of the 32 nm pitch cylindrical phase PS- b -PMMA block-copolymer film.

des Polymères Organiques in Bordeaux by Dr. Guillaume Fleury.

10.2 Sequential infiltration synthesis

In order to render the self-assembled block-copolymer thin films suitable for etching, the samples were subjected to ALD sequences of three cycles of tri-methyl aluminum (TMA) and water vapor. This step aims to incorporate aluminum oxide (Al_2O_3) selectively into the PMMA domains by a process known as sequential infiltration synthesis (SIS) [162]. This process exploits the ability to selectively modify the PMMA domains in the PS matrix through a chemical reaction between TMA and the carbonyl groups on the PMMA chains, after a long ALD exposure. The Al-CH_3/Al-OH chains formed within PMMA domains provide reactive sites for the selective growth of different materials, in this case nucleated Al_2O_3, by the sequential infiltration synthesis method [162]. In order to investigate the efficiency of this process, the as-modified surface was characterized by X-ray Photoelectron Spectroscopy (XPS). The results provided in Table 10.1 show the presence of three atomic species: carbon, oxygen and aluminum. The presence of

Chemical species	Atomic percentage
C_{1s}	80.63
O_{1s}	15.51
Al_{2p}	3.86

Table 10.1: XPS analysis of the surface after the ALD treatment.

carbon and oxygen comes from the organic nature of the original PS-b-PMMA block copolymer thin film while the presence of aluminum comes from the nucleated Al_2O_3 incorporated within the PMMA during the ALD treatment and the underlying SIS. This step was realized at the Catholic University of Louvain by Dr. Sébastien Faniel.

10.3 Oxygen plasma chemical etching

The next step consists in subsequently removing all the organic materials from the film surface by oxygen plasma chemical etching. In this way, the silicon substrate is left with covering close-packed Al_2O_3 nanostructures exhibiting approximately the same pitches as PMMA domains. The combined ALD treatment and oxygen plasma etching are illustrated in Fig. 10.2 with PMMA rods instead of perpendicularly aligned PMMA domains.

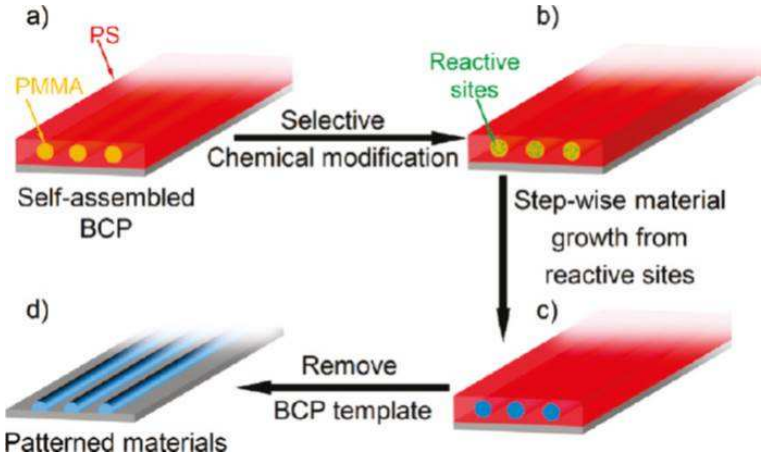

Figure 10.2: Simplified mechanism for the nanoscopic materials generation process with self-assembled block copolymer as the template [162].

The efficiency of the oxygen plasma etching was again investigated by XPS. The results provided in Table 10.2 underline the expected decrease of carbon, increase of oxygen (due to the oxidation of the silicon substrate) and appearance of silicon coming from the substrate. The presence of fluorine is assumed to be due to a contamination of the silicon substrate in the block-copolymer casting step.

Chemical species	Atomic percentage
C_{1s}	1.12
O_{1s}	50.92
Al_{2p}	4.21
F_{1s}	3.16
Si_{2p}	50.92

Table 10.2: XPS analysis of the surface after the oxygen plasma etching.

The Al_2O_3 nanostructures were observed by AFM and SEM for the 32 nm pitch PS-b-PMMA block copolymer surfaces (Fig. 10.3). The nanostructures exhibit averaged height of 6 nm, averaged diameter of 20 nm and averaged pitch of 29 nm. These aluminum oxide nanostructures should provide a robust mask for nanotexturing the underlying silicon by plasma etching and trying to obtain the desired nanocones-patterned surfaces. This step was realized at the University of Namur by Dr. Alexandre Felten.

At this stage of this work, we did not yet manage to transfer these nanostructures in the silicon by etching. The reason for this is probably the low averaged height of the Al_2O_3 nanos-

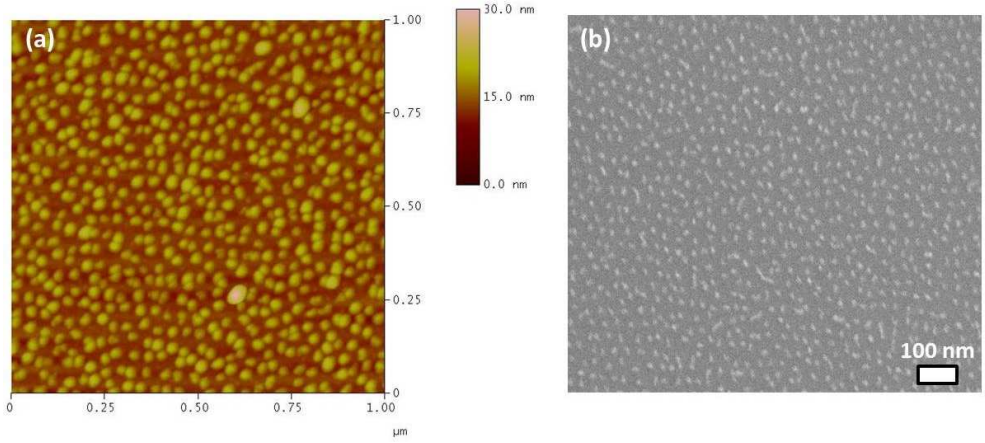

Figure 10.3: (a) AFM image of the topography of the Al_2O_2 nanostructures covering the silicon substrate. (b) SEM image of the topography of the Al_2O_2 nanostructures covering the silicon substrate.

tructures, which decrease the robustness of the mask during etching. Figure of the desired mask is illustrated on Fig. 10.4 from the work of Checco *et al.* [155]. Nevertheless, the two remaining

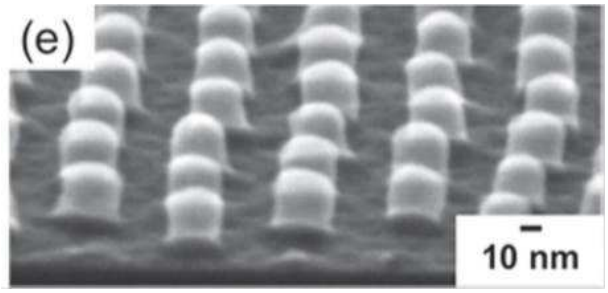

Figure 10.4: SEM image of the Al_2O_3 mask obtained by Checco *et al.* [155].

steps of the block-copolymer-based thin film patterning method are presented hereafter.

10.4 Plasma etching

From the aluminum oxide nanostructures acting as a mask, it is in principle possible to obtain by plasma etching different geometries of textures within the sub-10 nm scale (see Fig. 8.6 in Section 8.5). For instance, surfaces covered with cylindrical pillars can be created by anisotropically etching the silicon substrate using sulfur hexafluoride:oxygen (SF_6:O_2) gas chemistry at low temperature (- 100°C) [155]. Note that any remaining alumina can be removed by briefly immersing the sample in dilute buffered hydrofluoric acid. Moreover, by adjusting the etch process parameters, precise tailoring of the structure geometry can be provided. In the case of this work, conical nanostructures could be obtained by etching the silicon surface using a hydrogen bromide:chlorine:oxygen (HBr:Cl_2:O_2) chemistry [155]. Schematic side views of process flow for creating a nanotextured surface from a self-assembled block-copolymer thin film is displayed in Fig. 10.5. This step is under trial at the Ecole Centrale de Lyon by Prof. Christian Seassal.

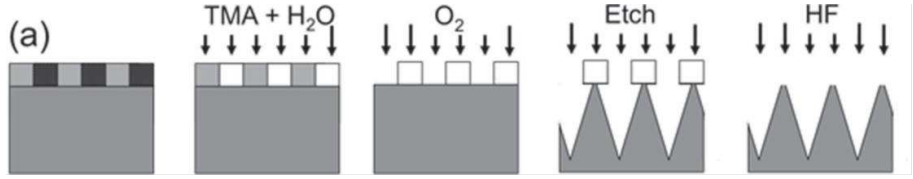

Figure 10.5: Sketch of the four main steps of the block-copolymer-based thin film patterning.

10.5 Octadecyltrichlorosilane passivating

The last step of the process is to render the nanostructured surface hydrophobic by passivating it with a 2.5 nm thick octadecyltrichlorosilane (OTS) [155], an apolar component the surface energy of which is close to the one of polyethylene [18]. The OTS coating is assumed to not significantly alter the surface topography [155]. This last step will be realize at the University of Namur by Dr. Bastien Bathélémy.

As explained in Section 8.5, this kind of patterned surface is tightly close to the polyethylene patterned surface studied during this work. Therefore, achieving the realization of this surface by the above proposed method would allow us to verify the theoretical predictions presented in this thesis work. However, due to its very challenging aspects, this experimental work requires further investigations.

Part V

Conclusions and perspectives

Conclusion

This thesis work aimed at investigating two different approaches of the multifunctionality of patterned surfaces. The first one, the classical approach, used a common methodology of dealing with the wettability and the optical properties, both of them being supposed to act independently from each others. This approach was applied to the treatment of the multifunctional behavior of the Grey Cicada's wings. It was shown that the nipple array nanostructure on the grey cicada wings could be considered as a two-in-one device with a hemisphere top which allows a strong water repellency and a truncated cone which ensures anti-reflective properties.

The second approach developed herein is the so-called nanophotonics approach. This new approach considers the interplay between the optical properties and the wetting properties. Based on the Lifshitz theory, it was highlighted that small nanoscopic corrugations, acting effectively as an antireflective coating, dramatically affect the Lifshitz-van der Waals interaction energy and thus the water contact angle of molecular solid surfaces. Using a cones patterned polyethylene surface as a case study and varying the corrugation height, it turned out that the higher the antireflectivity of the surface, the higher the superhydrophobicity at least from theoretical point of view. This aspect was usually ignored in the literature, although many experimental results tend to indicate that such a link between properties do exist. The effect of nanostructures on the density of vacuum photon modes should therefore be considered when wetting phenomena are studied, because it is responsible for the interplay between superhydrophobicity and antireflection property. Actually, in many practical cases, fractal structures appear to be quite efficient in achieving superhydrophobicity. Since those hierarchical structures involve, among others, nanoscopic corrugations (ranging from 10 to 100 nm), the role of the latter in wetting phenomena deserves a reinterpretation in the light of the quantum vacuum photon-mode origin of the van der Waals force.

From the above results, an original extension of this theoretical work was carried out in order to investigate the possibility of achieving repulsive Lifshitz-van der Waals interactions between two macroscopic bodies, by solely playing on nanostructures. As for wetting, it was shown theoretically that extremely small and steep nanoscopic corrugations on the surface of one of two interacting bodies were able to turn Lifshitz-van der Waals interactions from attractive to repulsive. This prediction is appealing since it offers the possibility of achieving a repulsive interaction only by nanopatterning one of the surfaces without any chemical treatment, as usually required. This new way of achieving dispersive repulsion could be used to control macroscopic interactions in a variety of applications, ranging from biology to materials science,

for controlling adhesion, and adsorption.

In terms of experimental perspectives, the obvious objective which should be targeted is the experimental validation of the effects that were predicted with our nanophotonics approach. This proof of concept could open the road to the design of novel superhydrophobic coatings and nanoelectromechanical systems, especially in the light of recent experimental studies, such as the one reported by Intravaia in 2013 [96]. However, the engineering complexity related to the achievement of a controlled pattern shape and depth just a few nanometers below the surface is a major obstacle. According to the experimental strategy proposed in Chapter 10, the key points of the chosen fabrication process lie in the synthesis of the Al_2O_3 mask and the subsequent plasma etching. These two tricky fabrication steps need to be further investigated in order to find the proper experimental conditions and to successfully overcome their related issues and fabricate the desired patterned surfaces.

From a theoretical point of view, the results of this thesis should be also compared with molecular dynamics simulations. Due to the lack of time, this effort has not been undertaken but is of course worth to be done. Indeed, since molecular dynamic takes into account van der Waals interactions between atoms and molecules, it could be truly interesting to compare for instance the static water contact angle calculated with our nanophotonics approach and molecular dynamics. Moreover, since the numerical method developed in the present thesis can handle complex periodic corrugation geometries, additional studies regarding, for instance, the wetting of fractal surfaces or hyperbolic metamaterials could be envisaged. Finally, it can be fairly assumed that our contribution to the understanding of Lifshitz-van der Waals force in nanostructures might contribute to elaborate more suitable models for describing more complex wettability phenomena such as contact angle hysteresis, Cassie state metastabilty, and Cassie-Wenzel transition.

Appendix A

Integration of the Lifshitz-van der Waals energy over the Brillouin zone

The integration method proposed by Monkhorst and Pack [148] is used for computing the Lifshitz-van der Waals energy. The method consists in discretizing the Brillouin zone into a set a relevant wave vectors $\overrightarrow{k}_{n_1,n_2}$ such as:

$$\overrightarrow{k}_{n_1,n_2} = \frac{2n_1 - N_1 - 1}{2N_1} \overrightarrow{b}_1 + \frac{2n_2 - N_2 - 1}{2N_2} \overrightarrow{b}_2 \tag{A.1}$$

where N_1 and N_2 are odd numbers, $n_i = 1, 2, ..., N_i$, $\overrightarrow{b}_1$ and $\overrightarrow{b}_2$ are the reciprocal lattice vectors (Fig. A.1). Therefore, the Lifshitz-van der Waals energy can be easily computed as :

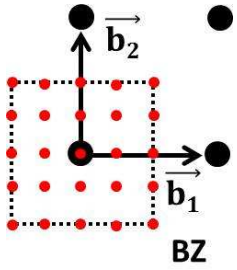

Figure A.1: Discretization of the Brillouin zone represented for a square lattice.

$$\begin{aligned} U^{LW}(L) &= \frac{\hbar (\Delta k)^2}{8\pi^3} \sum_{n_1,n_2} \int_0^\infty d\xi \ln[\det(1 - \\ &\quad S_1^{+-}(i\xi, \overrightarrow{k}_{n_1,n_2}) S_v^{--}(i\xi, \overrightarrow{k}_{n_1,n_2}) S_2^{-+}(i\xi, \overrightarrow{k}_{n_1,n_2}) S_v^{++}(i\xi, \overrightarrow{k}_{n_1,n_2}))], \end{aligned} \tag{A.2}$$

where $\Delta k = \frac{1}{N_1} \left| \overrightarrow{b}_1 \right| = \frac{1}{N_2} \left| \overrightarrow{b}_2 \right|$.

Appendix B

Convergence study of the Lifshitz-van der Waals potential energy

B.1 Cones

In the numerical calculation of the Lifshitz-van der Waals potential energy (Eq. (7.10)), the optimal number of photon wave vectors $N_{\overrightarrow{k}_{//}}$ of the cones patterned surface has been firstly investigated in the case of the effective medium treatment. For this purpose, the Lifshitz van-der Waals potential energy was calculated for a given separation distance $L = 5\ nm$ and a given cone height $h = 50\ nm$ (Fig. B.1a) and $h = 100\ nm$ (Fig. B.1b). In both cases, for $N_{\overrightarrow{k}_{//}} = 49$ was found to be enough for the potential energy to converge.

In the case of the three dimensional treatment of the patterned surface, the optimal number of photon wave vectors $N_{\overrightarrow{k}_{//}}$ has to be investigated jointly to the optimal number of reciprocal lattice vectors $N_{\overrightarrow{g}}$. In both cases, the Lifshitz-van der Waals potential energy converges for $N_{\overrightarrow{k}_{//}} = 49$ and $N_{\overrightarrow{g}} = 3 \times 3$. Consequently, the effective medium treatment and the three dimensional treatment give similar results in terms of Lifshitz-van der Waals potential energy (B.1). The physical reasons of such results are provided in the text.

B.2 Cylinders

In the case of the three dimensional treatment of the cylinders patterned surface, the optimal number of photon wave vectors $N_{\overrightarrow{k}_{//}}$ has to be investigated jointly to the number of reciprocal lattice vectors $N_{\overrightarrow{g}}$. For this purpose, the Lifshitz van-der Waals potential energy was calculated for a given separation distance $L = 5\ nm$ and a given cone height $h = 10\ nm$ (Fig. B.2a) and $h = 50\ nm$ (Fig. B.2b). In both cases, the Lifshitz-van der Waals potential energy converges for $N_{\overrightarrow{k}_{//}} = 49$ and $N_{\overrightarrow{g}} = 3 \times 3$. As cylinders are less close to conditions for the use of an effective medium approach, the effective medium treatment and the three dimensional treatment do not give the same results in terms of Lifshitz-van der Waals potential energy, although almost the

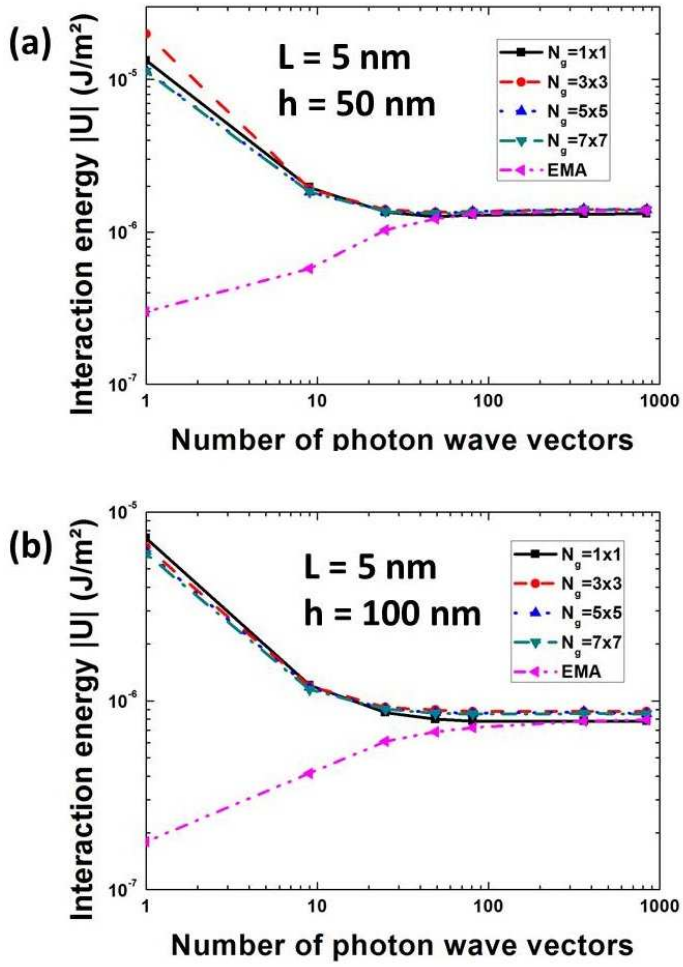

Figure B.1: Convergence curves of the Lifshitz-van der Waals potential energy for $L = 5\ nm$ and (a) $h = 50\ nm$.(b) $h = 100\ nm$. The optimal number of photon wave vectors is evaluated for several numbers of reciprocal lattice vectors, in the case of the three dimensional treatment of the patterned surface ($N_{\vec{g}}$=1,9,25 and 49).

same (Fig. B.2).

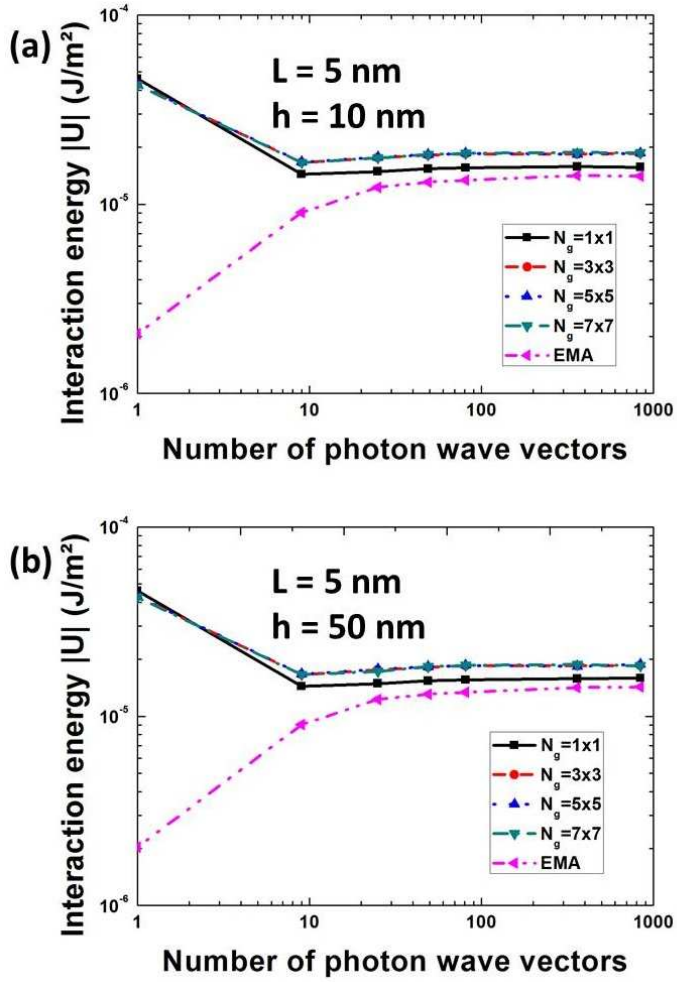

Figure B.2: Convergence curves of the Lifshitz-van der Waals potential energy for $L = 5\ nm$ and (a) $h = 10\ nm$.(b) $h = 500\ nm$. The optimal number of photon wave vectors is evaluated for several numbers of reciprocal lattice vectors ($N_{\overrightarrow{g}} = 1$, 9, 25 and 49).

Appendix C

Electrostatic potential energy between a cones array and a semi-infinite plane

Let us consider a cone with an opening angle α and a semi-infinite planar surface separated by a D distance (Fig. C.1). The surface A of the cone is given by :

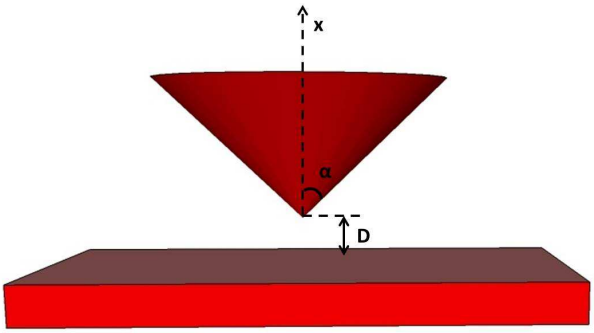

Figure C.1: Cone with an opening angle α and a semi-infinite planar surface ($\alpha = 0$).

$$A = \pi[(x - D)\tan(\alpha)]^2, \tag{C.1}$$

with $x \geq D$, which leads to :

$$dA = 2\pi \tan(\alpha)(x - D)dx. \tag{C.2}$$

The electrostatic potential energy is obtained using Derjaguin's approximation [77] :

$$W(D) = \int_D^\infty W_{S_1S_2}(x)dA, \tag{C.3}$$

where $W_{S_1S_2}(x)$ is the electrostatic potential energy between two semi-finite planar surfaces immersed in an electrolyte solution with a Debye legnth κ :

$$W_{S_1S_2}(x) = \varepsilon_r\varepsilon_0\kappa[2\psi_1\psi_2 e^{-\kappa x} - (\psi_1^2 + \psi_2^2)e^{-2\kappa x}], \tag{C.4}$$

where ε_r is the static dielectric constant of the electrolyte solution, ε_0 the static dielectric constant of vacuum and ψ_i the surface potential of the i^{th} surface. Injecting (C.2) and (C.2) into (C.4), the electrostatic potential energy is :

$$W(D) = \int_D^\infty \varepsilon_r\varepsilon_0\kappa[2\psi_1\psi_2 e^{-\kappa x} - (\psi_1^2 + \psi_2^2)e^{-2\kappa x}]2\pi\tan(\alpha)(x-D)dx, \tag{C.5}$$

which can be decomposed as :

$$\begin{aligned} W(D) \;=\; & \int_D^\infty (\varepsilon_r\varepsilon_0\kappa 2\psi_1\psi_2 e^{-\kappa x})2\pi\tan(\alpha)x dx \\ & - \int_D^\infty (\varepsilon_r\varepsilon_0\kappa 2\psi_1\psi_2 e^{-\kappa x})2\pi\tan(\alpha)D dx \\ & - \int_D^\infty (\varepsilon_r\varepsilon_0\kappa(\psi_1^2+\psi_2^2) e^{-2\kappa x})2\pi\tan(\alpha)x dx \\ & + \int_D^\infty (\varepsilon_r\varepsilon_0\kappa(\psi_1^2+\psi_2^2) e^{-2\kappa x})2\pi\tan(\alpha)D dx. \end{aligned} \tag{C.6}$$

Using the Hospital theorem, the electrostatic potential energy between an isolated cone and a semi-infinite plane writes as :

$$W(D) = \frac{2\pi\tan(\alpha)\varepsilon_r\varepsilon_0}{\kappa} e^{-\kappa D}(2\psi_1\psi_2 - (\psi_1^2+\psi_2^2)\frac{e^{-\kappa D}}{4}). \tag{C.7}$$

In the case of a hexagonal cones array, the electrostatic potential energy is :

$$W(D)_{hexagonal-array} = \frac{W(D)}{S_0} \tag{C.8}$$

where S_0=$\frac{a_0^2\sqrt{3}}{2}$ is the surface of the unit cell of the hexagonal array, with a_0 the lattice parameter. Note that such result is valid only if the cones interdistance is greater than the Debye length of the liquid.

Bibliography

[1] T. Young. An essay on the cohesion of fluids. *Philosophical Transactions of the Royal Society London*, **95**(65), 1805.

[2] J.W. Gibbs. On the equilibrium of heterogeneous substances. *Transactions of the Connecticut Academy of Arts and Sciences*, **3**(343), 1878.

[3] H.B. Eral, D.J.C.M Mannetje, and J.M Oh. Contact angle hysteresis: a review of fundamentals and applications. *Colloid and Polymer Science*, **291**(247), 2013.

[4] R. Tadmor. Line energy and the relation between advancing, receding, and young contact angles. *Langmuir*, **20**(7659), 2004.

[5] R. N. Wenzel. Resistance of solid surfaces to wetting by water. *Industrial and engineering chemistry*, **28**(988), 1936.

[6] A.B.D Cassie and S. Baxter. Wettability of porous surfaces. *Transactions of the Faraday Society*, **40**(546), 1944.

[7] C. Cuvelier, A. Segal, and A. A. van Steenhoven. *Finite Element Methods and Navier-Stokes Equations*. Springer Science and Business Media, New York, 1986.

[8] J. De Coninck and T.D. Blake. Wetting and Molecular Dynamics Simulations of Simple Liquids. *Annual Review of Material Research*, **38**(1), 2008.

[9] M. J. Kreder, J. Alvarenga, P. Kim, and J. Aizenberg. Design of anti-icing surfaces: smooth, textured or slippery? *Nature Reviews Materials*, **1**(15003), 2016.

[10] L. Dellieu, E. Lawarée, N. Reckinger, C. Didembourg, J.-J. Letesson, M. Sarrazin, O. Deparis, J.-Y. Matroule, and J.-F. Colomer. Do CVD grown graphene films have antibacterial activity on metallic substrates? *Carbon*, **84**(310), 2015.

[11] E.P. Ivanovna, J. Hasan, H. K. Webb, G. Gervinskas, S. Juodkazis, V. K. Truong abnd A. H.F. Wu, R. N. Lamb, V. A. Baulin, G. S. Watson, J. A. Watson, D. E. Mainwaring, and R. J. Crawford. Bacterial activity of black silicon. *Nature communications*, **4**(2838), 2013.

[12] P.G. de Gennes. Wetting: statics and dynamics. *Review of modern physics*, **57**(887), 1985.

[13] D.P. Woodruff. *The Chemical Physics of Solid Surfaces*. Elsevier, 2002.

[14] D.K. Owens and R.C. Wendt. Estimation of the Surface Free Energy of Polymers. *Journal of Applied Polymer Science*, **13**(1741), 1969.

[15] A. Shahravan, T. Desai, and Themis Matsoukas. Controlled manipulation of wetting characteristics of nanoparticles with dry-based plasma polymerization method. *Applied Physics Letters*, **101**(251603), 2012.

[16] C. J. Drummond and D. Y. C. Chan. van der Waals Interaction, Surface Free Energies, and Contact Angles: Dispersive Polymers and Liquids. *Langmuir*, **14**(3890), 1997.

[17] K. L. Mittal. *Adhesion Aspects of Polymeric Coatings*. Plenum Press, New York, 1983.

[18] J. N. Israelachvili. *Intermolecular and Surface Forces-Third Edition*. Academic Press (Elsevier), 2011.

[19] M. Lessel, O. Bäumchen, M. Klos, H. Hähl, R. Fetzer, M. Paulus, R. Seemanna, and K. Jacobsa. Self-assembled silane monolayers: an efficient step-by-step recipe for high-quality, low energy surfaces. *Surface and Interface Analysis*, **47**(557), 2015.

[20] A. Ulman. Formation and structure of self-assembled monolayers. *Chemical Reviews*, **96**(1533), 1996.

[21] W. Barthlott and C. Neinhuis. Purity of the sacred lotus, or escape from contamination in biological surfaces. *Planta*, **1**(202), 1997.

[22] T. Onda, S. Shibuichi, N. Satoh, and K. Tsujii. Superwater-repellent fractal surfaces. *Langmuir*, **12**(2125), 1996.

[23] Z. Yoshimitsu, A. Nakajima, T. Watanabe, and K. Hashimoto. Effetcs of Surface Structure on the Hydrophobicity and Slidind Behavior of Water Droplets. *Langmuir*, **18**(5818), 2002.

[24] D. Quéré. Fakir droplets. *Nature materials*, **1**(14), 2002.

[25] A. Tuteja, w. Choi, M. Ma, J.M. Mabry, S.A. Mazzella, GC. Rutledge, G.H. McKinley, and R. Cohen. Designing superoleophobic surfaces. *Science*, **318**(1618), 2007.

[26] T.L. Liu and C.-J. C. Kim. Turning a surface superrepellent even to completely wetting liquids. *Science*, **346**(1096), 2014.

[27] J.T. Simpson, S.R. Hunter, and T. Aytug. Superhydrophobic materials and coatings: a review. *Reports on Progress in Physics*, **78**(086501), 2015.

[28] D. Quéré. Wetting and roughness. *Annual Review of Materials Research*, **38**(71), 2008.

[29] D. Quéré. Non-sticking drops. *Reports on Progress in Physics*, **68**(2495), 2005.

[30] L. Dellieu, O. Deparis, P. Simonis, M. Sarrazin, and J.P. Vigneron. A two-in-one superhydrophobic and anti-reflective nanodevice in the grey cicada Cicada orni (Hemiptera). *Journal of Applied Physics*, **116**(024701), 2014.

[31] R. Helbig, J. Nickerl, C. Neinhuis, and C. Werner. Turning a surface superrepellent even to completely wetting liquids. *Science*, **346**(1096), 2014.

[32] A. Tuteja, W. Choi, J.M. Mabry, G.H. McKinley, and R.E. Cohen. Robust omniphobic surfaces. *Proceedings of the National Academy of Sciences*, **105**(18200), 2008.

[33] L. Bocquet and E. Lauga. A smooth future ? *Nature materials*, **10**(334), 2011.

[34] T-S. Wong, S.H. Kang, S. K. Y Tang, E. J. Smythe, B. D. Hatton, A. Grinthal, and J. Aizenberg. Bioinspired self-repairing slippery surfaces with pressure-stable omniphobicity. *Nature*, **447**(443), 2011.

[35] H.F. Bohn and W. Federle. Insect aquaplaning: Nepenthes pitcher plants capture prey with the peristome,a fullywettablewater-lubricatedanisotropic surface. *Proceedings of the National Academy of Sciences*, **101**(14138), 2004.

[36] P. Kim, T.-S. Wong, J. Alvarenga, M. J. Kreder, W. E. Adorno-Martinez, and J. Aizenberg. Liquid-infused nanostructured surfaces with extreme anti-ice and anti-frost performance. *ACS Nano*, **6**(6569), 2012.

[37] W. Ma, Y. Higaki, H. Otsuka, and A. Takahara. Perfluoropolyether-infused nano-texture: a versatile approach to omniphobic coatings with low hysteresis and high transparency. *Chemical Communications*, **49**(597), 2013.

[38] Q. Liu, Y. Yang, M. Huang, Y. Zhou, Y. Liu, and X. Liang. Durability of a lubricant-infused electrospray silicon rubber surface as an anti-icing coating. *Applied Surface Science*, **346**(68), 2015.

[39] M. Born and E. Wolf. *Principles of Optics*. Pergamon Press, 1970.

[40] L. Rayleigh. On the intensity of ligh reflected from certain surfaces at nearly perpendicular incidence. *Proceedings of the Royal Society of London*, **41**(275), 1886.

[41] H. K. Raut, V. A. Ganesh, A. S. Nairb, and S. Ramakrishna. Anti-reflective coatings: A critical, in-depth review. *Energy and environmental science*, **4**(3779), 2011.

[42] D.G Stavenga, S Foletti, G Palasantzas, and K Arikawa. Light on the moth-eye corneal nipple array of butterflies. *Proceedings of the Royal Society B*, **273**(691), 2006.

[43] E.W. Marchand. *Gradient Index Optics*. New York Academic Press, 1978.

[44] A. Herman, C. Trompoukis, O. El Daif, V. Depauw, and O. Deparis. Influence of the pattern shape on the efficiency of front-side periodically patterned ultrathin crystalline silicon solar cells. *Journal of Applied Physics*, **112**(11), 2012.

[45] J. Zhu, C.-M. Hsu, S. Fan Z. Yu, and Y. Cui. Nanodome Solar Cells with Efficient Light Management and Self-Cleaning. *NanoLetters*, **10**(1979), 2010.

[46] B. Dale and H. G. Rudenberg. Photovoltaic conversion : high effiency silicon solar cells. *Proc. 14th Annual Power Sources Conf.*, **1**(22), 1960.

[47] A. Bay, N. Ande, M. Sarrazin, A. Belarouci, V. Aimez, L. A. Francis, and J. P. Vigneron. Optimal overlayer inspired by Photuris firefly improves light-extraction efficiency of existing light-emitting diodes. *Optics Express*, **21**(177866), 2013.

[48] M.A. Pasquinelli and Y.G. Yingling. *Molecular dynamics simulations of bio-nano interactions*. Springer, 2012.

[49] N. Wei, C. Lv, and Z. Xu. Wetting of Graphene Oxide: A Molecular Dynamics Study. *Langmuir*, **30**(3572), 2014.

[50] J.Chen, B.J. Hanson, and M.A. Pasquinelli. Molecular Dynamics Simulations for Predicting Surface Wetting. *AIMS Materials Science*, **1**(121), 2014.

[51] J.E. Sprittles. *Dynamic wetting/dewetting processes in complex liquid-solid systems*. PhD thesis, School of Mathematics, The University of Birmingham, 2010.

[52] R. Hensel, R. Helbig, S. Aland, H.-G. Braun, A. Voigt, C. Neinhuis, and C. Werner. Wetting Resistance at Its Topographical Limit: The Benefit of Mushroom and Serif T Structures. *Langmuir*, **29**(1100), 2013.

[53] J.E. Sprittles and Y.D. Shikhmurzaev. Finite element framework for describing dynamic wetting phenomena. *International Journal for numerical methods in fluids*, **68**(1257), 2012.

[54] B. Gallinet, J. Butet, and O. J. F. Martin. Numerical methods for nanophotonics: standard problems and future challenges. *Laser and Photonics Reviews*, **9**(577), 2015.

[55] A. Taflove and S. Hagness. *Computational Electrodynamics, 3rd ed.* Artech House, Boston, 2005.

[56] M. Moharam and T.Gaylord. Rigorous coupled-wave analysis of planar-grating diffraction. *Journal of the Optical Society of America*, **71**(811), 1981.

[57] J.D van der Waals. *Over de Continuïteit van den Gas- en Vloeistoftoestand*. PhD thesis, Leinden University, 1873.

[58] F.London. Zur theorie und systematik der molekularkräfte. *Zeitschrift für Physik*, **63**(245), 1930.

[59] H.B.G. Casimir. On the attraction between two perfectly conducting plates. *Proceedings of the Royal Netherlands Academy of Arts and Science*, **B51**(793), 1948.

[60] E.M. Lifshitz. The theory of molecular attractive forces between solids. *Journal of experimental and theoretical physics USSR*, **29**(94), 1955.

[61] G. L. Klimchitskaya, U. Mohideen, and V. M. Mostepanenko. The Casimir force between real materials: Experiment and theory. *Review of Modern Physics*, **81**(1827), 2009.

[62] I. E. Dzyaloshinskii, E. M. Lifshitz, and L. P. Pitaevskii. General Theory of Van der Waals Forces. *Soviet Physics Uspekhi*, **4**(153), 1961.

[63] M. Kardar and R. Golestanian. The friction of vacuum, and other fluctuationinduced forces. *Review of Modern Physics*, **71**(1233), 1999.

[64] A. Lambrecht and S. Reynaud. Casimir force between metallic mirrors. *The European Physical Journal D*, **8**(309), 2000.

[65] F. Intravaia and A. Lambrecht. Surface plasmon modes and the Casimir energy. *Physical Review Letters*, **91**(110404), 2005.

[66] M.S.Tomas. Casimir force in absorbing multilayers. *Physical Review A*, **66**(052103), 2002.

[67] T.H. Boyer. Van der Waals forces and zero-point energy for dielectric and permeable materials. *Physical Review A*, **9**(2078), 1974.

[68] J. N. Munday, D. Iannuzzi, Y. Barash, and F. Capasso. Torque on birefringent plates induced by quantum fluctuations. *Physical Review A*, **71**(042102), 2005.

[69] P.H.G.M. van Blockland and J.T.G. Overbeek. van der waals forces between objects covered with a chromium layer. *Journal of the Chemical Society, Faraday Transaction*, **74**(2637), 1978.

[70] M. Bordag, G. L. Klimchitskaya, U. Mohidee, and V. M. Mostepanenko. *Advances in the Casimir effect*. Oxford University Press, 2009.

[71] S. K. Lamoreaux. Demonstration of the Casimir Force in the 0.6 to 6Range. *Physical Review Letters*, **78**(5), 1997.

[72] G. Bressi, G. Carugno, R. Onofrio, and G. Ruoso. Measurement of the Casimir Force between Parallel Metallic Surfaces. *Physical Review Letters*, **88**(4), 2002.

[73] A. A. Maradudin and P. Mazur. Effects of surface roughness on the van der Waals force between macroscopic bodies. *Physical Review B*, **22**(1677), 1980.

[74] P. Mazur and A. A. Maradudin. Effects of surface roughness on the van der Waals force between macroscopic bodies. II. Two rough surfaces. *Physical Review B*, **253**(695), 1981.

[75] B.V. Derjaguin, N.V. Churaev, and Y.I. Rabinovich. The modern state of the macroscopic theory of molecular forces and the results of its experimental verification for thin interlayers. *Advances in Colloid and Interface Science*, **28**(197), 1987.

[76] U. Mohideen and A. Roy. Precision Measurement of the Casimir Force from 0.1 to 0.9. *Physical Review Letters*, **81**(4549), 1998.

[77] B.V. Derjaguin. Untersuchungen über die Reibung und Adhäsion, IV. Theorie des Anhaftens kleiner Teilchen. *Kolloid-Zeitschrift*, **69**(155), 1934.

[78] D.E. Krause, R.S. Decca, D. Lopez, and E. Fischbach. Experimental investigation of the casimir force beyond the proximity-force approximation. *Physical Review Letters*, **98**(050403), 2007.

[79] A. Canaguier-Durand, P.A. Maia Neto, I. Cavero-Pelaez, A. Lambrecht, and S.Reynaud. Casimir interaction between plane and spherical metallic surfaces. *Physical Review Letters*, **102**(230404), 2009.

[80] G. L. Klimchitskaya, U. Mohideen, and V. M. Mostepanenko. Casimir and van der waals forces between two plates or a sphere lens above a plate made of real metals. *Physical Review A*, **61**(062107), 2000.

[81] A. O. Sushkov, W. J. Kim, D. A. R. Dalvit, and S. K. Lamoreaux. Observation of the thermal casimir force. *Nature physics*, **7**(230), 2011.

[82] A. Canaguier-Durand, P.A. Maia Neto, A. Lambrecht, and S.Reynaud. Thermal casimir effect in the plane-sphere geometry. *Physical Review Letters*, **104**(040403), 2010.

[83] J. N. Munday and F. Capasso. Precision measurement of the casimir lifshitz force in a fluid. *Physical Review A rapid communication*, **75**(060102), 2007.

[84] N. Munday, Federico Capasso, and V. Adrian Parsegian. Measured long-range repulsive Casimir Lifshitz forces. *Nature*, **457**(170), 2009.

[85] L. Seung woo Lee and S.M. Wolfgang. Afm study of repulsive van der waals forces between teflon af thin film and silica or alumina. *Colloids and Surfaces A*, **204**(43), 2002.

[86] H. B. Chan, V. A. Aksyuk, R. N. Kleiman, D. J. Bishop, and F. Capasso. Nonlinear micromechanical casimir oscillator. *Physical Review Letters*, **87**(211801), 2001.

[87] L.M. Woods, D.A.R. Dalvit, A. Tkatchenko, P. Rodriguez-Lopez, A.W. Rodriguez, and R. Podgornik. A materials perspective on casimir and van der waals interactions. *submitted to Review of Modern Physics.*

[88] M. F. Maghrebia, S. J. Rahia, T. Emig, N. Grahamd, R. L. Jaffea, and M. Kardar. Analytical results on casimir forces for conductors with edges and tips. *Proceedings of the National Academy of Sciences*, **108**(17), 2011.

[89] S. J. Rahi, T. Emig, R. L. Jaffe, and M. Kardar. Casimir forces between cylinders and plates. *Physical Review A*, **78**(012104), 2008.

[90] M. T. Homer Reid, A. W. Rodriguez, J. White, and S. G. Johnson. Efficient computation of casimir interactions between arbitrary 3d objects. *Physical Review Letters*, **103**(040401), 2009.

[91] L. Dellieu, O. Deparis, J. Muller, and M. Sarrazin. Quantum vacuum photon modes and superhydrophobicity. *Physical Review Letters*, **114**(024501), 2015.

[92] A. Lambrecht and V.N. Marachevsky. Casimir interaction of dielectric gratings. *Physical Review Letters*, **101**(160403), 2008.

[93] H. B. Chan, Y. Bao, J. Zou, R. A. Cirelli, F. Klemens, W. M. Mansfield, and C. S. Pai. Measurement of the casimir force between a gold sphere and a silicon surface with nanoscale trench arrays. *Physical Review Letters*, **101**(030401), 2008.

[94] R. Guérout, J. Lussange, F. S. S. Rosa, J.-P. Hugonin, D. A. R. Dalvit, J.-J. Greffet, A. Lambrecht, and S. Reynaud. Enhanced radiative heat transfer between nanostructured gold plates. *Physical Review B rapid communcation*, **85**(180301), 2012.

[95] P. S. Davids, F. Intravaia, F. S. S. Rosa, and D. A. R. Dalvit. Modal approach to casimir forces in periodic structures. *Physical Review A*, **82**(062111), 2010.

[96] F. Intravaia, S. Koev, I. W. Jung, A. A. Talin, P. S. Davids, R S. Decca, V. A. Aksyuko, D. A. R. Dalvit, and D. Lopez. Strong casimir force reduction through metallic surface nanostructuring. *Nature communication*, **4**(2515), 2013.

[97] K.V. Pappakrishnan and C.M. Pattabhirajuand A.G. Dentcho. Repulsive casimir force using metamaterials. *Proceeding SPIE*, **8455**(845510), 2012.

[98] F. J. Rodríguez-Fortuno, A. Vakil, and N. Engheta. Electric levitation using ϵ-near-zero metamaterials. *Physical Review Letters*, **112**(033902), 2014.

[99] H.-J. Butt, K. Graf, and M. Kappl. *Physics and Chemistry of Interfaces*. Wiley-VCH, New York, 2003.

[100] A. Lambrecht, P.A. Maia-Neto, and S. Reynaud. The Casimir effect within scattering theory. *New Journal of Physics*, **8**(243), 2006.

[101] D. Dalvit, P. Milonni, D. Robert, and F. da Rosa. *Casimir Physics*. Springer, 2011.

[102] A.W. Rodriguez, F. Capasso, and S. G. Johnson. The Casimir effect in microstructured geometries. *Nature photonics*, **5**(211), 2011.

[103] F. Capasso, J.N. Munday, D. Iannuzzi, and H. B. Chan. Casimir Forces and Quantum Electrodynamical Torques: Physics and Nanomechanics. *IEEE Journal of selected topics in quantum electronics*, **13**(2), 2007.

[104] H. B. Chan, V. A. Aksyuk, R. N. Kleiman, D. J. Bishop, and F. Capasso. Quantum Mechanical Actuation of Microelectromechanical Systems by the Casimir Force. *Science*, **291**(1941), 2001.

[105] R. Guérout, C. Genet, A. Lambrecht, and S. Reynaud. Casimir torque between nanostructured plates. *European Physics Letters*, **111**(44001), 2015.

[106] C.J. van Oss, M.K. Chaudhury, and R.J. Good. Interfacial Lifshitz-van der Waals and polar interactions in macroscopic systems. *Chemical Review*, **88**(927), 1988.

[107] W.H. Keesom. The second viral coefficient for rigid spherical molecules, whose mutual attraction is equivalent to that of a quadruplet placed at their centre. *Proceedings of the Royal Netherlands Academy of Arts and Science*, **18**(636), 1915.

[108] P. Debye. Die van der Waalsschen Kohasionskrafte. *Zeitschrift für Physik*, **21**(178), 1920.

[109] H. C. Hamaker. The london van der waals attraction between spherical particles. *Physica*, **4**(1058), 1937.

[110] C. J. van Oss. *Interfacial Forces in Aqueous Media - Second Edition.* Taylor and Francis, 2006.

[111] T. C. Choy. *Effective Medium Theory: Principles and Applications.* Clarendon Press, 1992.

[112] E. Hecht. *Optics - Fourth Edition.* Pearson Education, 2014.

[113] Jinguang Cai and Limin Qi. Recent advances in antireflective surfaces based on nanostructure arrays. *Material Horizons*, **2**(37), 2014.

[114] J. Zhu and Y. Cui. Nanocones as antireflection coating. *SPIE Proceedings*, 2009.

[115] J.P. Vigneron, F. Forati, D. André, A. Castiaux, I. Derycke, and A. Dereux. Theory of electromagnetic energy transfer in three-dimensional structures. *Ultramicroscopy*, **61**(21), 1995.

[116] M. Sarrazin. *Etude de propriétés optiques liées à la transmission de cristaux photoniques bidimensionnels.* PhD thesis, Université de Franche-Comté, 2002.

[117] L. Mandel and E. Wolf. *Optical coherence and quantum optics.* Cambridge University Press, 1995.

[118] A. Lambrecht, I. Pirozhenko, L. Duraffourg, and Ph. Andreucci. The Casimir effect for Silicon and Gold slabs. *Europhysics Letters*, **77**(44006), 2007.

[119] I. Pirozhenko and A. Lambrecht. Influence of slab thickness on the Casimir force. *Physical Review A*, **77**(013811), 2008.

[120] J. Yu, G. A. Rance, and A. N. Khlobystov. Electrostatic interactions for directed assembly of nanostructured materials: composites of titanium dioxide nanotubes with gold nanoparticles . *Journal of Materials Chemistry*, **19**(8928), 2009.

[121] H.J.Kimble. The quantum internet. *Nature*, **453**(1023), 2008.

[122] C. Genet, A. Lambrecht, and S. Reynaud. Temperature dependence of the casimir effect between metallic mirrors. *Physical Review A*, **62**(012110), 2000.

[123] L. Ahlfors. *Complex analysis: an introduction to the theory of analytic functions of one complex variable*. McGraw-Hill, 1979.

[124] C. Kittel. *Introduction to Solid State Physics, 8th Edition*. Wiley, 2005.

[125] G.C. Wick. Properties of Bethe-Salpeter Wave Functions. *Physical Review*, **96**(1124), 1954.

[126] A. Lambrecht and S. Reynaud. Casimir force between metallic mirrors. *European Physics Journal D*, **8**(309), 2000.

[127] C. Genet, F. Intravaia, A. Lambrecht, and S. Reynaud. Electromagnetic vacuum fluctuations, casimir and van der waals forces. *Annales de la Fondation Louis de Broglie*, **29**(1), 2004.

[128] O. Deparis, N. Khuzayim, and and J. P. Vigneron A. Parker. Assessment of the antireflection property of moth wings by three-dimensional transfer-matrix optical simulations. *Physical Review Et*, **79**(041910), 2009.

[129] J. P. Vigneron and V. Lousse. Variation of a photonic crystal color with the Miller indices of the exposed surface. *Proceedings SPIE*, **6128**(61281G), 2006.

[130] M. Sun, A. Liang, Y. Zheng, G.S. Watson, and J. A. Watson. A study of the antireflection efficiency of natural nano-arrays of varying sizes. *Bioinspiration and Biomimetics*, **6**(026003), 2011.

[131] D. Quéré. Rough ideas on wetting. *Physica A*, **313**(32), 2002.

[132] M.W. Holdgate. The wetting of insect cuticles by water. *Journal of Experimental Biology*, **32**(591), 1955.

[133] G. Vazquez, E. Alvarez, and J. M. Navaza. Surface Tension of Alcohol Water + Water from 20 to 50 .degree.C. *Journal of Chemical and Engineering data*, **40**(611), 1995.

[134] L. Dellieu. Surface multifonctionnelle d'origine biologique : l'aile de la cigale grise. Master's thesis, Université de Namur, 2013.

[135] G. S. Watson, S. Myhra, B. W. Cribb, and J. A. Watson. Putative Functions and Functional Efficiency of Ordered Cuticular Nanoarrays on Insect Wings. *Journal of Chemical and Engineering data*, **94**(3352), 2008.

[136] Á. M. Alhambra, A. Kempf, and E. Martín-Martínez. Casimir forces on atoms in optical cavities. *Physical Review A*, **89**(033835), 2014.

[137] H. B. Chan, V. A. Aksyuk, R. N. Kleiman, D. J. Bishop, and Federico Capasso. Quantum Mechanical Actuation of Microelectromechanical Systems by the Casimir Force. *Science*, **291**(1941), 2001.

[138] J. Ashok, P. L. H. Varaprasad, and J. R. Birch. *Handbook of Optical Constants of Solids II*. E. D. Palik, Academic Press Elsevier, New York, 1991.

[139] A. Deinega and S. John. Effective optical response of silicon to sunlight in the finite-difference time-domain method. *Optics letters*, **37**(112), 2012.

[140] V.A. Parsegian and G. H. Weiss. Spectroscopic parameters for computation of van der waals forces. *Journal of Colloids and Interface science*, **81**(285), 1981.

[141] S. Mouchet, O. Deparis, and J.-P. Vigneron. Unexplained high sensitivity of the reflectance of porous natural photonic structures to the presence of gases and vapours in the atmosphere. *SPIE Proceedings*, 2012.

[142] A. P. McCauley, F. S. S. Rosa, A. W. Rodriguez, J. D. Joannopoulos, D. A. R. Dalvit, and S. G. Johnson. Structural anisotropy and orientation-induced Casimir repulsion in fluids. *Physical Review A*, **83**(052503), 2011.

[143] R. Zhao, J. Zhou, Th. Koschny, E. N. Economou, and C. M. Soukoulis. Repulsive Casimir Force in Chiral Metamaterials. *Physical Review Letters*, **103**(103602), 2009.

[144] A. P. McCauley, R. Zhao, M. T. H. Reid, A. W. Rodriguez, J. Zhou, F. S. S. Rosa, J. D. Joannopoulos, D. A. R. Dalvit, C. M. Soukoulis, and S. G. Johnson. Microstructure effects for Casimir forces in chiral metamaterials. *Physical Review B*, **82**(165108), 2010.

[145] Y. Zheng and A. Narayanaswamy. Patch contribution to near-field radiative energy transfer and van der Waals pressure between two half-spaces. *Physical Review A*, **89**(022512), 2014.

[146] D. Courjon. *Near-Field Microscopy and Near-Field Optics*. Imperial College Press, London, 2003.

[147] J. Muller, G. Parent, G.Jeandel, and David Lacroix. Finite-difference time-domain and near-field-to-far-field transformation in the spectral domain: application to scattering objects with complex shapes in the vicinity of a semi-infinite dielectric medium . *Journal of the Optical Society of America A*, **28**(868), 2011.

[148] H.J. Monkhorst and J. D. Pack. Special points for Brillouin-zone integrations. *Physical Review B*, **13**(5188), 1976.

[149] B. E. A. Saleh and M. C. Teich. *Fundamentals of Photonics, 2nd ed.* Wiley-Interscience, New York, 2007.

[150] C. Yang, U. Tartaglino, and B. N. J. Persson. Influence of Surface Roughness on Superhydrophobicity. *Physical Review Letters*, **97**(116103), 2006.

[151] W. Fenzl. Continuous Wetting Transitions in Systems with Van der Waals Interaction. *Berichte der Bunsengesellschaft für physikalische Chemie*, **98**(389), 1994.

[152] W. Fenzl. van der Waals interaction and wetting transitions. *Europhysics Letters*, **64**(64), 2003.

[153] J. Rafiee, X. Mi, H. Gullapalli, A. V. Thomas, F. Yavari, Y. Shi, P. M. Ajayan, and N. A. Koratkar. Wetting transparency of graphene. *Nature materials*, **11**(217), 2012.

[154] J.D. Miller, S. Veeramasuneni, J. Drelich, and M.R. Yalamanchili. Effect of roughness as determined by atomic force microscopy on the wetting properties of PTFE thin films. *Polymer Engineering and Science*, **36**(1849), 1996.

[155] A. Checco, A. Rahman, and C. T. Black. Robust Superhydrophobicity in Large-Area Nanostructured Surfaces Defi ned by Block-Copolymer Self Assembly. *Advanced Materials*, **26**(886), 2013.

[156] S.-W. Lee and W. M. Sigmund. AFM study of repulsive van der Waals forces between Teflon AF thin film and silica or alumina. *Colloids and Surfaces A*, **204**(43), 2002.

[157] J. Visser. The concept of negative hamaker coefficients. 1. history and present status. *Advances in Colloid and Interface Science*, **2**(157), 1981.

[158] J. Visser. On Hamaker constants: A comparison between Hamaker constants and Lifshitz-van der Waals constants. *Advances in Colloid and Interface Science*, **3**(331), 1972.

[159] L. Dellieu, O. Deparis, J. Muller, B. Kolaric, and M. Sarrazin. Quantum vacuum photon modes and repulsive Lifshitz-van der Waals interactions. *Physical Review B*, **92**(235418), 2015.

[160] R. A. Segalman. Patterning with block copolymer thin films. *Materials Science and Engineering R*, **48**(191), 2005.

[161] Q. Peng, Y-C. Tseng, S. B. Darling, and J. W. Elam. Nanoscopic patterned materials with tunable dimensions via atomic layer deposition on block copolymers. *Advanced Materials*, **22**(5129), 2010.

[162] Q. Peng, Y-C. Tseng, S. B. Darling, and J. W. Elam. A route to nanoscopic materials via sequential infiltration synthesis on block copolymer templates. *ACS Nano*, **5**(6), 2011.